

**PREPARATION AND CHARACTERIZATION OF
ZnO/ZnAl₂O₄ MIXED METAL OXIDE AS AN EFFECTIVE
ANODE MATERIALS FOR DYE-SENSITIZED
PHOTODETECTOR**

ETHAR YAHYA SALIH

**FACULTY OF ENGINEERING
UNIVERSITY OF MALAYA
KUALA LUMPUR**

2018

**PREPARATION AND CHARACTERIZATION OF
ZnO/ZnAl₂O₄ MIXED METAL OXIDE AS AN
EFFECTIVE ANODE MATERIALS FOR DYE-
SENSITIZED PHOTODETECTOR**

ETHAR YAHYA SALIH

**THESIS SUBMITTED IN FULFILMENT OF THE
REQUIREMENTS FOR THE DEGREE OF DOCTOR OF
PHILOSOPHY**

**FACULTY OF ENGINEERING
UNIVERSITY OF MALAYA
KUALA LUMPUR**

2018

UNIVERSITY OF MALAYA
ORIGINAL LITERARY WORK DECLARATION

Name of Candidate: **Ethar Yahya Salih**

Matric No: KHA140116

Name of Degree: Ph.D

Title of Project Paper/Research Report/Dissertation/Thesis (“this Work”):

**Preparation and Characterization ZnO/ZnAl₂O₄ Mixed Metal Oxide as an
Effective Anode Materials for Dye-Sensitized Photodetector**

Field of Study: **Nanomaterials/Advance Materials**

I do solemnly and sincerely declare that:

- (1) I am the sole author/writer of this Work;
- (2) This Work is original;
- (3) Any use of any work in which copyright exists was done by way of fair dealing and for permitted purposes and any excerpt or extract from, or reference to or reproduction of any copyright work has been disclosed expressly and sufficiently and the title of the Work and its authorship have been acknowledged in this Work;
- (4) I do not have any actual knowledge nor do I ought reasonably to know that the making of this work constitutes an infringement of any copyright work;
- (5) I hereby assign all and every rights in the copyright to this Work to the University of Malaya (“UM”), who henceforth shall be owner of the copyright in this Work and that any reproduction or use in any form or by any means whatsoever is prohibited without the written consent of UM having been first had and obtained;
- (6) I am fully aware that if in the course of making this Work I have infringed any copyright whether intentionally or otherwise, I may be subject to legal action or any other action as may be determined by UM.

Candidate’s Signature

Date:

Subscribed and solemnly declared before,

Witness’s Signature

Date:

Name:

Designation:

UNIVERSITI MALAYA
PERAKUAN KEASLIAN PENULISAN

Nama: **Ethar Yahya Salih**

No. Matrik: KHA140116

Nama Ijazah: Ph.D

Tajuk Kertas Projek/Laporan Penyelidikan/Disertasi/Tesis (~~Hasil Kerja ini~~):

**Penyediaan dan Pencirian ZnO/ZnAl₂O₄ Campuran Logam Oksida sebagai
Bahan Anod Berkesan untuk Pengesan-foto Peka-Pewarna**

Bidang Penyelidikan: **Bahan Nano/Bahan Pendahuluan**

Saya dengan sesungguhnya dan sebenarnya mengaku bahawa:

- (1) Saya adalah satu-satunya pengarang/penulis Hasil Kerja ini;
- (2) Hasil Kerja ini adalah asli;
- (3) Apa-apa penggunaan mana-mana hasil kerja yang mengandungi hakcipta telah dilakukan secara urusan yang wajar dan bagi maksud yang dibenarkan dan apa-apa petikan, ekstrak, rujukan atau pengeluaran semula daripada atau kepada mana-mana hasil kerja yang mengandungi hakcipta telah dinyatakan dengan sejasasnya dan secukupnya dan satu pengiktirafan tajuk hasil kerja tersebut dan pengarang/penulisnya telah dilakukan di dalam Hasil Kerja ini;
- (4) Saya tidak mempunyai apa-apa pengetahuan sebenar atau patut semunasabahnya tahu bahawa penghasilan Hasil Kerja ini melanggar suatu hakcipta hasil kerja yang lain;
- (5) Saya dengan ini menyerahkan kesemua dan tiap-tiap hak yang terkandung di dalam hakcipta Hasil Kerja ini kepada Universiti Malaya (~~UM~~) yang seterusnya mula dari sekarang adalah tuan punya kepada hakcipta di dalam Hasil Kerja ini dan apa-apa pengeluaran semula atau penggunaan dalam apa jua bentuk atau dengan apa juga cara sekalipun adalah dilarang tanpa terlebih dahulu mendapat kebenaran bertulis dari UM;
- (6) Saya sedar sepenuhnya sekiranya dalam masa penghasilan Hasil Kerja ini saya telah melanggar suatu hakcipta hasil kerja yang lain sama ada dengan niat atau sebaliknya, saya boleh dikenakan tindakan undang-undang atau apa-apa tindakan lain sebagaimana yang diputuskan oleh UM.

Tandatangan Calon

Tarikh:

Diperbuat dan sesungguhnya diakui di hadapan,

Tandatangan Saksi

Tarikh:

Nama:

Jawatan:

**PREPARATION AND CHARACTERIZATION OF ZnO/ZnAl₂O₄ MIXED
METAL OXIDE AS AN EFFECTIVE ANODE MATERIALS FOR DYE-
SENSITIZED PHOTODETECTOR**

ABSTRACT

Semiconductor nanomaterials-based photodetectors have attracted considerable attention from various research groups because of their low fabrication cost, easy handling, short carrier-diffusion path length and high density. Photodetector, which is an optoelectronic device, is of growing concern since it can determine the intensity of incident photons by transferring the yielded energy of absorbed light into a measurable electrical signal. Recently, new class photodetector was introduced, namely, dye-sensitized photodetector. Dye-sensitized photodetector has shown great interest among researchers due to its attracting properties such as low fabrication cost and eco-friendly processing. One of the key factors of enhancing the photo-responsive behavior of dye-sensitized photodetector is to develop a deep understanding of each component in this device. Among these component is anode material, which is considered the main component in Dye-sensitized photodetector. The anode material, in dye-sensitized photodetector, serves dual functions; firstly, as a support for sensitizer loading and secondly as a transporter of photo-excited electrons. Therefore, the introduction of new class materials is of great importance. In the present study, Zn/Al layered double hydroxide as precursor was employed with its microstructural features modified. Moreover, ZnO/ZnAl₂O₄ mixed metal oxides obtained as a result of thermally-treated Zn/Al layered double hydroxide was used as the anode materials due to its superior features such as ultra-fast injection efficiency, similar band gap to ZnO and TiO₂, easy manufacturing handling at large scale and relatively large surface area. It was found that the optimum sample (Z6A-MMO-400) exhibited mesoporous surface morphology with value of 53 m²/g surface area which was found to be very sufficient for high dye loading

(3.3×10^{-4} mol/cm²). In the UV-Vis analysis, a noticeable red shift towards the visible light was noticed and energy band gap of 3.21 eV was acquired as the thermal treatment temperature increased from 200 to 400 °C. In term of photoluminescence properties, it was observed that both increment in thermal treatment temperature as well as molar ratio resulted in higher I_{NBE}/I_{DLE} ratio. Pristine ZA-LDH exhibited a value of 0.13, whereas Z6A-MMO-400 demonstrated a value of 0.78. The optimum dye-sensitized photodetector Z6A-MMO-400 showed photo-responsivity of 1.1×10^{-2} A/W at 25 mW/cm², whereas Z6A-MMO-200 and Z3A-MMO-400 exhibited values as low as 2.2×10^{-3} and 1.5×10^{-3} A/W at 25 mW/cm², respectively. Nonetheless, the response time was calculated to be lower than the recovery time which validates faster electron injection than recombination process. A precise control of the prepared anode materials properties can be used to study and optimize the performance of DS photodetector made of this novel material system.

Keywords: Mixed metal oxide, layered double hydroxide, dye-sensitized photodetector, photo-responsivity, response/recovery time.

**PENYEDIAAN DAN PENCIRIAN ZnO/ZnAl₂O₄ CAMPURAN LOGAM
OKSIDA SEBAGAI BAHAN ANOD BERKESAN UNTUK PENGESAN-FOTO
PEKA-PEWARNA**

ABSTRAK

Pengesan-foto berasaskan bahan nano telah menarik banyak perhatian daripada pelbagai kumpulan penyelidikan kerana kos fabrikasi yang murah, mudah dibawa, laluan penyebaran yang pendek dan ketumpatan yang tinggi. Pengesan-foto, yang merupakan peranti optoelektronik, semakin menarik perhatian kerana ia dapat menentukan intensiti foton insiden dengan memindahkan tenaga cahaya yang diserap ke dalam isyarat elektrik yang boleh diukur. Baru-baru ini, pengesan-foto kelas baru telah diperkenalkan, iaitu pengesan-foto peka-pewarna. Pengesan-foto peka-pewarna telah menarik minat yang tinggi di kalangan penyelidik kerana sifatnya yang unggul seperti kos fabrikasi yang rendah dan pemprosesan yang mesra alam. Antara faktor utama untuk meningkatkan keadaan sifat fotografi responsif untuk pengesan-foto peka-pewarna adalah dengan mempunyai pemahaman yang mendalam tentang setiap komponen dalam peranti ini. Antara komponen terlibat adalah bahan anod, yang dianggap sebagai komponen utama dalam pengesan-foto peka-pewarna. Bahan anod, dalam pengesan-foto peka-pewarna, berfungsi sebagai fungsi ganda; pertama, sebagai sokongan untuk memastikan tahap kepekaan dan kedua sebagai pengangkut fenomena foto-pengujaan elektron. Oleh itu, pengenalan bahan kelas baru adalah diperlukan. Dalam kajian ini, dua hidroksida Zn/Al berlapis digunakan dengan ciri-ciri mikrostrukturnya yang diubah suai. Selain itu, oksida logam campuran ZnO/ZnAl₂O₄ yang diperoleh hasil daripada dua hidroksida Zn/Al berlapis yang diperoleh melalui kaedah pemanasan menunjukkan ciri-ciri unggul seperti kecekapan suntikan ultra-pantas, jurang jalur yang sama dengan ZnO dan TiO₂, pengendalian pembuatan yang mudah pada skala besar dan keluasan luas permukaan relatif. Telah didapati bahawa

sampel MMO optimum (Z6A-MMO-400) memperlihatkan morfologi permukaan mesolias dengan nilai luas permukaan $53 \text{ m}^2/\text{g}$ yang didapati sangat mencukupi untuk memuatkan pewarna tinggi ($3.3 \times 10^{-4} \text{ mol}/\text{cm}^2$). Dalam analisis UV-Vis, satu anjakan merah yang ketara ke arah cahaya diperhatikan apabila suhu pengoksidaan meningkat dari 200 hingga 400 °C dengan jurang tenaga sebanyak 3.21 eV. Dari segi sifat kefotopencapaian, diperhatikan bahawa kedua-dua kenaikan dalam nisbah molar serta suhu pengoksidaan menghasilkan nisbah $I_{\text{NBE}} / I_{\text{DLE}}$ yang lebih rendah. ZA-LDH asli memperlihatkan nilai 0.13, manakala Z6A-MMO-400 menunjukkan nilai 0.78. Pengesan-foto peka-pewarna optimum Z6A-MMO-400 menunjukkan foto-responsif iaitu $1.1 \times 10^{-2} \text{ A}/\text{W}$ pada $25 \text{ mW}/\text{cm}^2$, manakala Z6A-MMO-200 dan Z3A-MMO-400 masing-masing menunjukkan nilai serendah 2.2×10^{-3} dan $1.5 \times 10^{-3} \text{ A}/\text{W}$ pada $25 \text{ mW}/\text{cm}^2$. Walau bagaimanapun, masa tindakbalas yang dikira menjadi lebih rendah daripada masa pemulihan yang mengesahkan suntikan elektron lebih cepat daripada proses penggabungan semula. Ketelitian kawalan terhadap sifat-sifat bahan anod yang disediakan boleh digunakan untuk kajian ketumpatan cas-pengangkut dan pengoptimalan prestasi peranti yang dibuat daripada sistem bahan baru.

Keywords: campuran logam oksida, dua hidroksida berlapis, pengesan-foto peka-pewarna, foto-responsif, masa tindakbalas/ pemulihan

ACKNOWLEDGEMENTS

First and foremost, I would like to sincerely acknowledge my supervisors, namely, Assoc. Prof. Dr. Mohd Faizul Mohd Sabri, Assoc. Prof. Dr. Khaulah Suliman, Prof. Dr. Mohd Zobir and Assoc. Prof. Dr. Suhana Mohd Said for their countless hours of valuable suggestions, recommendations, enthusiasm, motivation and immense knowledge.

Besides, I would like to express my deepest appreciations to Ms. Noor Shafinie Surapandi for her endless encouragement and support throughout the whole period of my study, thank you for everything. Simultaneously, I would like to dedicate my gratitude to my friends, colleagues, acquaintance and faculty members who directly or indirectly supported me during my study.

On top of all, I would love to offer my sincere appreciations and gratitude to my parents, whatsoever; there are no words to express my feelings and gratefulness for everything they have been doing for me since my birth. Last but not least, my sincerest thanks to my siblings for all their unconditional support and consistent caring.

TABLE OF CONTENTS

Preparation and Characterization of ZnO/ZnAl ₂ O ₄ Mixed Metal Oxide as an Effective Anode Materials for Dye-Sensitized Photodetector Abstract	iii
Penyediaan dan Pencirian ZnO/ZnAl ₂ O ₄ Campuran Logam Oksida sebagai Bahan Anod Berkesan untuk Pengesan-foto Peka-Pewarna Abstrak	v
Acknowledgements	vii
Table of Contents	viii
List of Figures	xi
List of Tables.....	xv
List of Symbols and Abbreviations.....	xvi
List of Appendices	xviii
CHAPTER 1: INTRODUCTION.....	1
1.1 Background.....	1
1.2 Motivation of the study.....	4
1.3 Research objectives	6
1.4 Thesis framework	7
CHAPTER 2: THEORY AND LITERATURE	8
2.1 Anode materials	8
2.1.1 Layered double hydroxides	10
2.1.2 Mixed metal oxides	12
2.1.3 Phase transformation of LDH to MMO.....	15
2.2 Photodetector	17
2.2.1 Photodetector current-voltage characteristics.....	17
2.2.2 Photodetector sensing parameters	20

2.2.3	Photodetector operation modes	24
2.2.4	Types of photodetector	25
2.2.4.1	Organic photodetectors	25
2.2.4.2	Inorganic photodetectors	27
2.2.4.3	Hybrid inorganic-organic photodetectors.....	30
2.3	Dye-sensitized photodetector.....	31
2.3.1	Dye-sensitized photodetector structure	33
2.3.1.1	Photoanode	34
2.3.1.2	Redox mediator (Electrolyte).....	37
2.3.1.3	Photo cathode	38
2.3.1.4	Conductive glass substrate	40
2.3.1.5	Device packing (Sealing)	41
2.3.2	Electron transport process in dye-sensitized photodetector	41
2.4	Summary.....	46
CHAPTER 3: MATERIALS, EXPERIMENTAL METHODS AND PROCEDURES		
47		
3.1	Methodology.....	48
3.1.1	Substrate cleaning protocol	48
3.1.2	Zn/Al-LDH preparation.....	48
3.1.3	ZnO/ZnAl ₂ O ₄ -MMO anode materials preparation and phase Transformation	49
3.1.4	Dye-sensitized photodetector fabrication.....	50
3.2	Characterization techniques.....	51
3.2.1	Thermogravimetric analysis	52
3.2.2	X-ray diffraction.....	53
3.2.3	Field emission scanning electron microscopy.....	53

3.2.4	Surface area and pore size analysis	54
3.2.5	Surface profilometer	55
3.2.6	Ultraviolet/Visible/Infrared spectroscopy analysis	56
3.2.7	Photoluminescence spectroscopy	57
3.2.8	DS photodetector performance measurements	58
 CHAPTER 4: RESULTS AND DISCUSSION		60
4.1	Thermal properties analysis	61
4.2	Microstructural properties analysis	64
4.2.1	X-ray Diffraction	64
4.2.2	Field emission scanning electron microscopy	69
4.2.3	Surface area, pore volume and pore size analysis	75
4.3	Optical properties analysis	83
4.3.1	Ultraviolet-visible light spectroscopy	83
4.3.2	Photoluminescence spectroscopy	93
4.4	Dye-sensitized photodetector performance analysis	97
4.4.1	Spectral response of dye-sensitized photodetector	97
4.4.2	Illumination power dependence of dye-sensitized photodetector	102
4.4.3	Spatial and Temporal Response Time of Dye-sensitized Photodetector	113
4.5	Summary	117
 CHAPTER 5: CONCLUSION AND RECOMMENDATIONS		119
5.1	Conclusion	119
5.2	Recommendations and future work	120
References		122
Appendices		140

LIST OF FIGURES

Figure 1.1: Working principle and device design of visible light dye-sensitized photodetector.....	3
Figure 2.1: Evolution of the share distribution of publications (Ye <i>et al.</i> , 2015).....	9
Figure 2.2: Schematic depiction of the layered double hydroxide structure (Salomao <i>et al.</i> , 2011).....	11
Figure 2.3: The general structure of a typical ordered MMO where A ⁺² and B ⁺³ atoms occupy tetrahedral and octahedral holes, respectively (Issa <i>et al.</i> , 2013).....	13
Figure 2.4: Schematic representation of the phase transformation of LDH precursor into the ZnO/ZnAl ₂ O ₄ -MMO.....	17
Figure 2.5: Current-Voltage characteristics schematic illustration.....	20
Figure 2.6: Schematic representation of a typical DSSC function and structure.....	34
Figure 2.7: (a) schematic representation of the DS photodetector kinetics (Omar & Abdullah, 2014) and (b) operation principle and scheme of the energy levels of a solid-state device.....	45
Figure 3.1: Methodology flowchart.....	47
Figure 3.2: Schematic diagram of Zn/Al-LDH nanoparticles synthesis procedure.....	49
Figure 3.3: Schematic diagram of MMO anode materials preparation and thermal treatment process.....	50
Figure 3.4: Schematic diagram of the DS photodetector.....	51
Figure 3.5: Photocurrent measurements setup of the fabricated DS photodetector.....	59
Figure 4.1: TGA-DTG curves of (a) Z3A-LDH (b) Z4A-LDH, (c) Z5A-LDH, (d) Z6A-LDH and (e) Z7A-LDH samples; whereas (f) a comparison between TGA curves.....	63
Figure 4.2: X-ray diffraction patterns of ZrA-LDH prepared at different molar ratios, where $r = 3, 4, 5, 6$ and 7	65
Figure 4.3: (a) X-ray diffraction patterns of Z6A-MMO- T prepared at different temperatures, where $T = 200, 300, 350, 400, 450$ and 500 °C; and (b) average (100), (002) and (101) planes intensity of Z6A-MMO- T	67

Figure 4.4: (a) X-ray diffraction patterns of thermally treated <i>ZrA-MMO-400</i> prepared at different molar ratio where $r = 3, 4, 5, 6$ and 7 ; and (b) average (100), (002) and (101) planes intensity of <i>ZrA-MMO-400</i> .	68
Figure 4.5: FESEM images of the pristine <i>ZrA-LDH</i> at different molar ratios; (a) <i>Z3A-LDH</i> , (b) <i>Z4A-LDH</i> , (c) <i>Z5A-LDH</i> , (d) <i>Z6A-LDH</i> and (e) <i>Z7A-LDH</i> .	70
Figure 4.6: FESEM images of the prepared <i>Z6A-MMO-T</i> at different thermal treatment temperatures; (a) <i>Z6A-MMO-200</i> , (b) <i>Z6A-MMO-300</i> , (c) <i>Z6A-MMO-350</i> , (d) <i>Z6A-MMO-400</i> , (e) <i>Z6A-MMO-450</i> and (f) <i>Z6A-MMO-500</i> .	72
Figure 4.7: FESEM images of the prepared <i>ZrA-MMO-400</i> at different molar ratios; (a) <i>Z3A- MMO-400</i> , (b) <i>Z4A- MMO-400</i> , (c) <i>Z5A- MMO-400</i> , (d) <i>Z6A- MMO-400</i> and (e) <i>Z7A- MMO-400</i> .	74
Figure 4.8: Nitrogen adsorption/desorption isotherms of <i>Z6A-MMO-T</i> samples; (a) <i>Z6A-MMO-200</i> , (b) <i>Z6A-MMO-300</i> , (c) <i>Z6A-MMO-350</i> , (d) <i>Z6A-MMO-400</i> , (e) <i>Z6A-MMO-450</i> and (f) <i>Z6A-MMO-500</i> .	77
Figure 4.9: Surface area and pore volume of <i>Z6A-MMO-T</i> samples, where $T = 200, 300, 350, 400, 450$ and 500 °C.	78
Figure 4.10: Nitrogen adsorption/desorption isotherms of <i>ZrA-MMO-400</i> samples; (a) <i>Z3A-MMO-400</i> , (b) <i>Z4A-MMO-400</i> , (c) <i>Z5A-MMO-400</i> , (d) <i>Z6A-MMO-400</i> and (e) <i>Z7A-MMO-400</i> .	80
Figure 4.11: Surface area and pore volume of <i>ZrA-MMO-400</i> samples, where $r = 3, 4, 5, 6$ and 7 .	81
Figure 4.12: Nitrogen adsorption/desorption isotherms of pristine <i>Z6A-LDH</i> and <i>Z6A-MMO-400</i> samples.	82
Figure 4.13: Schematic diagram of ZnO and $ZnAl_2O_4$ energy levels together with their photo-excitation process (X. Zhao <i>et al.</i> , 2012).	84
Figure 4.14: Absorbance spectra of <i>Z6A-MMO-T</i> samples at different thermal treatment temperatures ($T = 200, 300, 350, 400, 450$ and 500 °C).	86
Figure 4.15: Optical band gap of <i>Z6A-MMO-T</i> samples at different thermal treatment temperatures; (a) <i>Z6A-MMO-200</i> , (b) <i>Z6A-MMO-300</i> , (c) <i>Z6A-MMO-350</i> , (d) <i>Z6A-MMO-400</i> , (e) <i>Z6A-MMO-450</i> and (f) <i>Z6A-MMO-500</i> .	87
Figure 4.16: Absorbance spectra of <i>ZrA-MMO-400</i> samples at different ratios ($r = 3, 4, 5, 6$ and 7).	89

Figure 4.17: Optical band gap of <i>ZrA</i> -MMO-400 samples at different molar ratios; (a) Z3A-MMO-400, (b) Z4A-MMO-400, (c) Z5A-MMO-400, (d) Z6A-MMO-400 and (e) Z7A-MMO-400.....	90
Figure 4.18: Optical properties of (a) absorbance of pristine Z6A-LDH and thermally treated Z6A-MMO-400 samples, (b) Z6A-LDH energy band gap no.1 (c) Z6A-LDH energy band gap no.2 and (e) Z6A-LDH energy band gap no.3.....	92
Figure 4.19: (a) Normalized PL spectra; and (b) I_{NBE}/I_{DLE} ratio of Z6A-MMO- <i>T</i> samples, where <i>T</i> = 200, 300, 350, 400, 450 and 500 °C.....	94
Figure 4.20: (a) Normalized PL spectra; and (b) I_{NBE}/I_{DLE} ratio of <i>ZrA</i> -MMO-400 samples, where r = 3, 4, 5, 6 and 7.....	95
Figure 4.21: Normalized PL spectra of Z6A-LDH and Z6A-MMO-400 samples.	96
Figure 4.22: (a) Illustrative schematic of MMO anode material in dark condition, (b) Dye-sensitized mechanism and (c) proposed energy diagram of DS photodetector based on MMO and N719 sensitizer photoanode (Foruzin <i>et al.</i> , 2016).	98
Figure 4.23: (a) Spectral response of Z6A-MMO-400 and Z6A-MMO-400 containing dye N719, (b) Z6A-MMO- <i>T</i> + Dye N719, (c) <i>ZrA</i> -MMO-400 + Dye N719, (d) absorbance spectra of dye N719 at different concentrations; and (e) linear fit of absorption λ max of dye N719 at 525 nm.....	101
Figure 4.24: Photocurrent vs. illumination power for Z6A-MMO- <i>T</i> DS photodetectors; (a) zero and (b) 0.2 V bias voltages.	104
Figure 4.25: Illumination power dependence of photo-responsive behavior of Z6A-MMO- <i>T</i> DS photodetectors: (a) photo-responsivity, (b) photo-conductivity at 0.2 V bias voltage, (c) photo-detectivity and (d) effective quantum efficiency.....	106
Figure 4.26: Photocurrent vs. illumination power for <i>ZrA</i> -MMO-400 DS photodetectors; (a) zero and (b) 0.2 V bias voltages.....	108
Figure 4.27: Illumination power dependence of photo-responsive behavior of <i>ZrA</i> -MMO-400 DS photodetectors: (a) photo-responsivity, (b) photo-conductivity at 0.2 V bias voltage (c) photo-detectivity and (d) effective quantum efficiency.	111
Figure 4.28: Logarithmic scale of photo-responsivity and effective quantum efficiency as a function of illumination power for Z6A-MMO-400 DS photodetector.....	112
Figure 4.29: Photo-switching characteristics of the fabricated Z6A-MMO- <i>T</i> DS photodetectors under alternating dark and light illumination at zero and 0.2 bias voltage; (a) Z6A-MMO-200, (b) Z6A-MMO-300, (c) Z6A-MMO-350, (d) Z6A-MMO-400, (e) Z6A-MMO-450 and (f) Z6A-MMO-500.	114

Figure #4.30: Photo-switching characteristics of the fabricated *ZrA-MMO-400* DS photodetectors under alternating dark and light illumination at zero and 0.2 bias voltage; (a) *Z3A-MMO-400*, (b) *Z4A-MMO-400*, (c) *Z5A-MMO-400*, (d) *Z6A-MMO-400*, (e) *Z7A-MMO-400*. 115

Figure #4.31: Response/recovery time of *Z6A-MMO-400* DS photodetector. 116

University of Malaya

LIST OF TABLES

Table 2.1: Brief of the materials type and sensing parameter used in DS photodetector.	32
Table 4.1: TGA/DTG in-depth data of pristine ZrA-LDH; where $r = 3, 4, 5, 6$ and 7 ...62	62
Table 4.2: In-depth analysis of pristine ZrA-LDH synthesized at different molar ratios.	66
Table 4.3: Surface area, pore volume and average pore size of the prepared Z6A-MMO- T samples at different thermal treatment temperatures.	76
Table 4.4: Surface area, pore volume and average pore size of the prepared ZrA-MMO-400 samples at different molar ratio.	79
Table 4.5: Comparison table with other researches' outcomes.	82
Table 4.6: Comparison table to other researchers' outcomes.	92
Table 4.7: Amount of dye N719 loaded on MMO anode material layers.....	102
Table 4.8: Photocurrent magnitude, in mA, for Z6A-MMO- T DS photodetectors at different illumination power intensities.	104
Table 4.9: Photocurrent magnitude, in mA, for ZrA-MMO-400 DS photodetectors at different illumination power intensities.	109
Table 4.10: Response/Recovery time comparison to other researchers' outcomes.	117
Table 4.11: Summary of the results analysis for all samples.	118

LIST OF SYMBOLS AND ABBREVIATIONS

ZnO	:	Zinc Oxide
Al ₂ O ₄	:	Aluminate
LDH	:	Layered double hydroxide
MMO	:	Mixed metal oxide
DS	:	Dye-sensitized
2D	:	Two-dimensional
I_D	:	Dark current
I_S	:	Saturation current
q	:	Electron absolute charge
n	:	Ideality factor
V	:	Voltage
K_B	:	Boltzman's constant
T	:	Temperature
P_o	:	Power density
λ	:	Absorption wavelength
T, d	:	Sensing film thickness
I_{ph}	:	Photocurrent
R	:	Photo-responsivity
P_{in}	:	Incident optical power
S	:	Photo-conductivity
A	:	Active area of sensing film
D^*	:	Photo-detectivity
NEP	:	Noise equivalent power
EQE	:	Effective quantum efficiency

D/A	:	Donor-acceptor
HOMO	:	High occupied molecular orbitals
LUMO	:	Low unoccupied molecular orbitals
IR	:	Infrared radiation
UV	:	Ultraviolet
Vis	:	Visible light
Si	:	Silicon
SOI	:	Silicon-on-insulator
DSSC	:	Dye-sensitized solar cell
FTO	:	Fluorine doped tin oxide
CB	:	Conduction band
VB	:	Valence band
Pt	:	Platinum
ITO	:	Indium tin oxide
NaOH	:	Sodium hydroxide
PEG	:	Polyethylene glycol
N719	:	Ruthenizer
RT	:	Room temperature
TGA/DTG	:	Thermogravimetric
XRD	:	X-ray diffraction
FESEM	:	Field emission electron microscopy
°C	:	Celsius
BET	:	Brunauer-Emmett-Teller

LIST OF APPENDICES

Appendix A: Raw materials specifications and chemical formulas.....	140
Appendix B: Raw materials calculation for preparation of ZrA-LDH samples	142
Appendix C: Thermal analysis (TGA/DTG) of Z6A-MMO 400.....	144
Appendix D: The sequence order of photocurrent magnitude at 100 mW/cm ² as a function of thermal treatment temperature and molar ratio	145

University of Malaya

CHAPTER 1: INTRODUCTION

1.1 Background

Semiconductor nanomaterials-based photodetectors have attracted significant consideration from various research groups because of their low fabrication cost, easy handling, short carrier-diffusion path length and high density (Lopez-Sanchez *et al.*, 2013; W. Zhang *et al.*, 2014; Q. Zhao *et al.*, 2017). Photodetector, which is an optoelectronic device, is of growing concern since these solid-state devices can determine the incident photons intensity by transferring the yielded amount of absorbed light energy into a measureable electrical signal. Photodetectors are considerably significant from the industrial perspective because of their wide range of applications in military, industrial, environmental and even biological areas (Antoni Rogalski, 2002; Waynant & Ediger, 2000). Over the past two decades, an ongoing research efforts which led to vital breakthrough in the improvement of environmentally friendly, economical and compact photodetectors with their sensing parameters improved was conducted (Guo *et al.*, 2008; Y. Lee *et al.*, 2015; Qadir *et al.*, 2014; Xue *et al.*, 2007; S. H. Yu *et al.*, 2014). Basically, photodetectors are mainly classified into two different groups; thermal and photoelectric detectors.

Thermal detectors: The incident light is absorbed and subsequently raises the sensing element temperature. In the meanwhile, the thermal sensor output signal is obtained as a variation in temperature which in turn consider as electrical and/or physical characteristics of the detecting material. In 1800, the rehabilitated outcomes of Herschel research have been known as an evidence light detecting by thermometer (Herschel, 1800),

“Thermometer No. 1 rose 7 degrees in 10 minutes by an exposure to the full red coloured rays. I drew back the stand... thermometer No. 1 rose, in 16 minutes, 8 3/8 degrees when its center was 1/2 inch out of the visible rays”

These detectors are considered as passive devices, where the operational biasing for these devices is not required. An associated drawback with these types of photodetector is that the incident light spectral content of these devices is not detected. Nevertheless, Johnson noise and white noise are considered as the main noise source of these kinds of photodetectors.

Photoelectric detectors: the photo-excitation is the main function of the operation mechanism of these detectors. The incident photons are collected by the detecting film, where the output electrical signal is then generated by the detecting film materials. Photoelectric detectors as optoelectronic devices outsmart thermal detectors in terms of the sensing parameters (linearity in response, sensitivity and stability properties). Four main types of photoelectric sensors are classified as photoconductive photoemissive and photodiodes (Parreira *et al.*, 2012; Qadir *et al.*, 2015; A Rogalski & Razeghi, 1996; Saleh & Teich, 2007). The general operational mechanism of photoelectric detectors varies. The main focus of this thesis is the dye-sensitized photodetector (DS photodetector). In DS photodetectors, photon energy absorption occurs on the anode materials surface (detecting film) which serves as sensitizer loader and initializes photo-excitation (Figure 1.1). Subsequently, a charge transfer occurs within the interface of the sensitizer and the semiconductor conduction band, where both components are then called a photoanode, eventually facilitating carrier movement to the collector (O'regan & Grätzel, 1991b).

One of the key factors of enhancing the key sensing parameters of DS photodetector is to develop a deep understanding of each and every component in this optoelectronic

device. Among these component is the anode materials, which is considered the main component of the sensing element in DS photodetector. The anode materials, in DS photodetector, serves a dual function; firstly as a holder designed for the sensitizer loading and secondly as a transporter of electrons photo-excitation phenomenon. An ideal anode materials, therefore, must have both characteristics, large surface area in support to the sensitizer loading as well as fast charge transport rate in support to electron photo-excitation (Maçaira *et al.*, 2013; Ye *et al.*, 2015). Thus, the search for new class materials which provide both functions with high performance is of great importance.

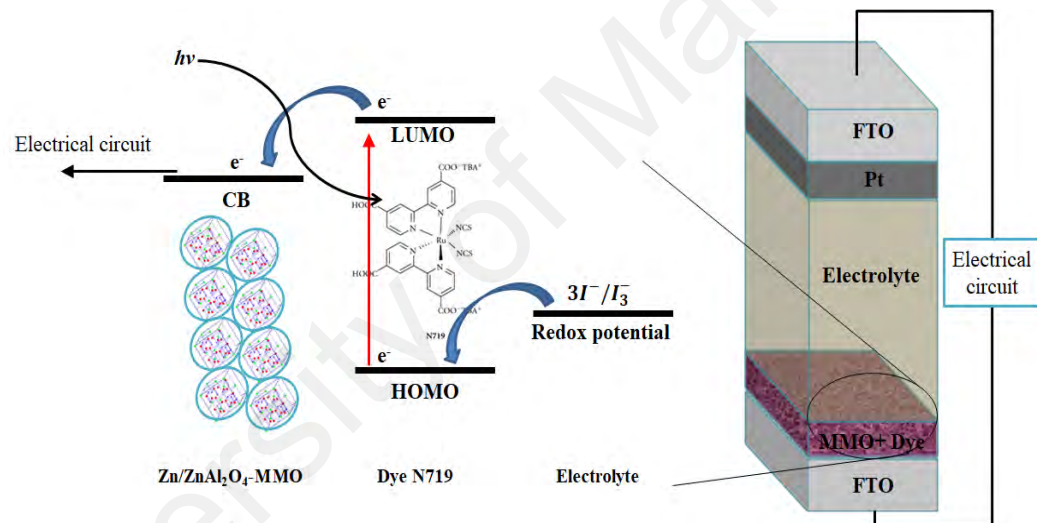


Figure 1.1: Working principle and device design of visible light dye-sensitized photodetector.

Layered double hydroxides (LDHs) is a brucite structure, $(M^{II} (OH)_2)$ constituting a class of two-dimensional (2D) anionic clays. The LDH can be expressed by the general formula, $[M_{1-x}^{II} M_x^{III} (OH)_2 (A^{n-})_{\frac{x}{n}} mH_2O]$, in which constant M^{III} , M^{II} and coefficient x represent trivalent metallic ions, divalent metallic ions and cation molar ratio, $[M^{III} / (M^{II} + M^{III})]$, respectively. The interlayer anion is represented by constant A whereas the charge of the interlayer anion is denoted as n in the formula (Cavani *et al.*, 1991; Rives, 2001; Williams & O'Hare, 2006). Therefore, a wide range of isostructural

materials can be easily acquired by varying the components of metal cations, interlayer anions or the cation molar ratio of M^{III}/M^{II} . LDHs has been widely applied in an enormous number of applications including photovoltaics, photocatalysts, drug delivery, micro container and etc (Cho *et al.*, 2013; Lei *et al.*, 2007; Liu *et al.*, 2007; Wei *et al.*, 2007; M. Yang *et al.*, 2014). Thermal treatment of LDH results in 2D layered structure collapse and continuously the formation of binary or ternary mixed metal oxides (MMOs) depending on the number of the ionic salts. MMOs have unique features, for instance sufficient electron injection efficiency, high surface area, high photo-response, and wide optical band gap, which make it a perfect candidate for applications that require anode materials with these features. MMOs offer wide range of applications such as photo-catalyst, lithium ion batteries, solar energy conversion and sensors (Béres *et al.*, 1999; Carja *et al.*, 2010; Foruzin *et al.*, 2016; Latorre-Sanchez *et al.*, 2012; Morandi *et al.*, 2006). The fabrication approaches of nanocomposites are widely diversified. Apart from the conventional physical and chemical routes, thermal treatment of LDHs could serve as an alternative approach for the preparation of MMOs.

1.2 Motivation of the study

Recently, a variety of studies aimed to enhance the photo-responsive behavior of photodetectors based mixed inorganic semiconductors have been reported (Musselman *et al.*, 2012; Sharma *et al.*, 2016; F. Zhang *et al.*, 2013; T.-F. Zhang *et al.*, 2016). All these approaches require complex facilities and/or need sophisticated chemical preparation process, and yet to be further advanced for specific applications. Dye-sensitization approach associated with inorganic materials offers an alternative short pathway to enhance the materials photo-responsive behavior. It was originally reported in 1991 by O'regan (O'regan & Grätzel, 1991a), and then accordingly employed in solar cells aiming at efficiency enhancement (J. Cao *et al.*, 2017; Cao *et al.*, 2016; Foruzin *et al.*, 2016; L. Zhang *et al.*, 2014). The fascination of this technique is easy handling

process at low fabrication cost. A potential breakthrough for this approach is using organic dye combined together with functional semiconductor materials for superior prospective application in optoelectronic devices such as DS photodetectors. A number of publications have been attracted to enhance and explore the photo-responsive properties of DS photodetector (Y. Lee *et al.*, 2015; Parreira *et al.*, 2012; Qadir *et al.*, 2014; Qadir *et al.*, 2015; Teng *et al.*, 2016; S. H. Yu *et al.*, 2014). However, further development to enhance the sensing parameters such as photo-responsivity, photo-conductivity and photo-detectivity is required; and to achieve this claim, each component in the DS photodetector must be developed especially the anode materials which in turn supports the enhancement of the sensing parameters.

The motivation and the main aim of this thesis is to discover the potentials in order to develop the photo-responsive behavior of the DS photodetector. It is well-known that careful selection of inorganic donor/acceptor semiconductor materials for photoactive electrode (photoanode) in the DS photodetector possibly leads to a dramatic growth in photo-responsive behavior with respect to carrier concentration in an organic framework (Teng *et al.*, 2016; L. Zhang *et al.*, 2014). Therefore, the alteration of contents and the selection of materials of photoanode film are highly essential for advance development in the sensing parameters of DS photodetector. MMO obtained from thermal treatment of LDH have been successfully proposed due to their unique features (Choi *et al.*, 2009; Dodd *et al.*, 2006; Zheng *et al.*, 2009). Moreover, MMOs have been investigated as promising semiconductors for a number of applications, for example photo-catalyst, lithium ion batteries, solar energy conversion and sensors (Béres *et al.*, 1999; Carja *et al.*, 2010; Foruzin *et al.*, 2016; Latorre-Sanchez *et al.*, 2012; Morandi *et al.*, 2006). Unfortunately, the application of ZnO/ZnAl₂O₄-MMO obtained from Zn/Al-DH as anode materials for DS photodetector has not been investigated. Moreover, Zn/Al-precursor gives rise to wide range of morphology structures especially a continuous

mesoporous film with large surface area after thermal treatment which is considered a beneficial characteristic for high sensitizer loading. Nevertheless, MMO film obtained from thermally-treated LDH exhibits high purity and crystallinity (L. Zhang *et al.*, 2014). Hence, this thesis aims to demonstrate a novel DS photodetector based mesoporous ZnO/ZnAl₂O₄-MMO as anode materials using Zn/Al-LDH as precursor.

1.3 Research objectives

For this thesis, the subsequent objectives were introduced to address the motivation of study mentioned above.

1. To examine extensively the thermal, structural and morphological properties of Zn/Al-LDH nanoparticles with mesoporous continuous structure at different molar ratios.
2. To establish an optimum thermal treatment temperature and molar ratio of the prepared Zn/ZnAl₂O₄-MMO anode materials with high crystallinity, porosity and surface area but low optical band gap and surface defects.
3. To fabricate DS photodetector based mesoporous ZnO/ZnAl₂O₄-MMO anode materials and investigate the photo-responsive behavior in term of the key-sensing parameters, switching behavior and response/recovery time.
4. To demonstrate a robust correlation between the prepared Zn/ZnAl₂O₄-MMO anode materials and the fabricated DS photodetectors through the microstructural and optical properties as well as the photo-responsive behavior.

1.4 Thesis framework

In Chapter 2, an extensive overview of the theory and literature review is presented aiming to outline the latest progresses in photodetectors. The materials structure used in this study has been explained. A comprehensive illustration of the working mechanism, structure and key sensing parameters of DS photodetector has been also presented.

Chapter 3 provides the materials used in this study and then summaries the experimental procedures together with the thermal, structural, morphological, physical, optical, electrical and photo-responsive characterization techniques.

Chapter 4 demonstrates the center focus of this thesis, by which it reports and discusses thoroughly the effect of thermal treatment temperature and molar ratio alteration on the thermal, microstructural, and optical properties of the fabricated anode semiconductors. Later in this Chapter, a comprehensive analysis of the spectral response, photo-responsive parameters, switching behavior and response/recovery times of the fabricated DS photodetectors is demonstrated in details.

Finally, the main contributions of this work are outlined in Chapter 5. A future research directions and recommendations on the field of DS photodetector are counseled through the final unit of the mentioned chapter.

CHAPTER 2: THEORY AND LITERATURE

The theory and literature of this study are outlined in the current chapter. The essential key features of anode materials and the components used in this thesis are presented in details in the first section of this chapter. Subsequently, a brief introduction of the recent photodetectors types including their recent development and working mechanism is detailed. The key sensing parameters of a typical photodetector are also explained. Finally, the last section of this chapter demonstrates a comprehensive illustration of the fabricated DS photodetector together with the electron transferring analysis in this type of solid-state device.

2.1 Anode materials

Nanostructured semiconductor anode materials are considered as one of the main framework components of DS solid-state devices. These materials are of great use in DS solid-state devices because of their essential functions. The anode materials mainly serves dual functions; firstly as sensitizer loading supporter and secondly as the photo-excited electrons carrier towards the external circuit. A successful anode material ought to perform both functions at the same time. Therefore, a reasonable surface area is required to confirm satisfactory sensitizer loading; likewise a reasonably high electron transport is necessary to ensure high mobility to the collector. These dual characteristics define the ideal anode materials (Maçaira *et al.*, 2013; Ye *et al.*, 2015). The anode materials in DS photodetector are dyed using sensitizer to alter their optical properties to visible light region in which photoanode is occurred. In conjunction with the mentioned two functions (surface area and transport rate), around 12 μm thick film formed of one or more semiconductors that have three-dimensional nanoparticles network is characteristically employed as the anode in DS photodetector. Although a high surface area of about 50-55 m^2/g enables high sensitizer loading ability, network

disorder with huge grain boundaries declines electron mobility which in turn decreases the charge transport rate (Feng *et al.*, 2012; J. Wang & Lin, 2012). This behavior significantly limits the overall performance of such solid-state device. The inherited issues associated with the anode materials, such as TiO₂ and ZnO, structure demand a search for additional constructive nanostructured anode semiconductors and advanced morphological structures. A variety of studies have been demonstrated to enhance the anode materials performance in DS solid-state devices by modifying the infrastructure of the anode materials using a number of approaches. Among these approaches are various structures fabrication, doping with ions, structuring with noble metals, coating with up/down conversion materials and modification with metal oxides (P.-Y. Chen *et al.*, 2013; Dembele *et al.*, 2013; Lijuan Luo *et al.*, 2011; Ye *et al.*, 2011; J. Yu *et al.*, 2013; L. Zhang *et al.*, 2014; R. Zhang *et al.*, 2008; Zhu *et al.*, 2017). Figure 2.1 shows the sharing of publications for each part of DS solid-state devices. It is clear to observe that the anode materials of DS solid-state devices participate with large portion of publications; whereas anode materials deliver the most important and challenging part of these devices.

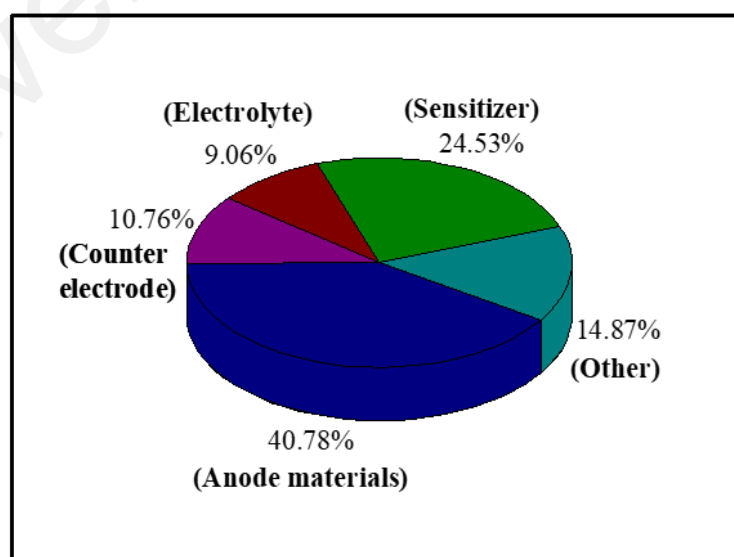


Figure 2.1: Evolution of the share distribution of publications (Ye *et al.*, 2015).

In this thesis, new class mesoporous ZnO/ZnAl₂O₄ anode materials consisting of more than one metal ion are introduced with their morphologies modified. These semiconductors are prepared and characterized as breakthrough anode materials based DS photodetector. Since it was proven that the combination of more than one metal oxide significantly reduces the recombination of charge in the hetero-structured anode materials sensing film, especially if the proposed materials exhibit high dye loading through high surface area (Hassanein *et al.*, 2017; Yuan *et al.*, 2017; R. Zhang *et al.*, 2008).

2.1.1 Layered double hydroxides

Layered double hydroxides (LDHs) are brucite-like layers class which is consisted of two-dimensional anionic clays whose structure can be expressed by the well-known formula of LDH $[M^{II}_{1-x}M^{III}_x(OH)_2]^{x+}(A^{n-})_{x/n}yH_2O$, where M^{II} and M^{III} cations as well as Aⁿ⁻ are divalent and trivalent metallic ions and interlayer anion, respectively. While x , stoichiometric coefficient which is varied over a wide range and n stand for the cation molar ratio and charge of the interlayer anion, respectively (Braterman *et al.*, 2004; Evans & Duan, 2006; Williams & O'Hare, 2006). Therefore, a various range of isostructural substitution materials and positively-charged sheets can be obtained. The balance of the positive charge is obtained by the intercalation of anions in hydrated interlayers galleries (Evans & Slade, 2006). The general structure of a typical LDH is shown in Figure 2.2. The flexibility of LDHs composition gives rise to functional LDHs with enormous range of properties and this property is one of the LDHs' greatest attractive features (Ali Ahmed, Talib, Hussein, *et al.*, 2012; J. He *et al.*, 2006).

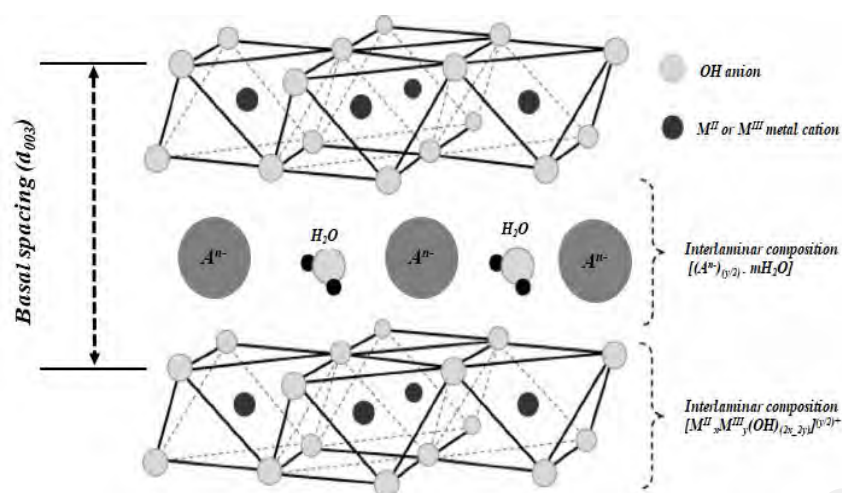


Figure 2.2: Schematic depiction of the layered double hydroxide structure (Salomao *et al.*, 2011).

LDHs demonstrate a wide range of applications including the use as photo-catalyst as well as in environmental remediation, additives in polymers, in medicine and biology and as precursor for electrical, optical and magnetic applications (F. Li & Duan, 2006). In a number of applications in specific solid-state devices such as inorganic detectors, photovoltaics and gas sensors, LDHs are required to be fabricated into a continuous well-oriented layer. Therefore, this step is considered as challenging in the preparation of LDHs material which is in powder form (Schwenzer *et al.*, 2009; Shu *et al.*, 2006; Z. Wu *et al.*, 2004). Since then, LDHs preparation process has been one of the most attractive and growing areas of LDH chemistry and therefore a number of researches have been conducted aiming to organizing LDH materials as uniformly aligned films or arrays using variety of substrates. Among these applications, LDHs are used in heterogeneous catalysts (Hadnadjev-Kostic *et al.*, 2017; Lü *et al.*, 2008), anti-corrosion coats for metals (F. Zhang, M. Sun, *et al.*, 2008; F. Zhang, L. Zhao, *et al.*, 2008), clay-modified anodes (Roto & Villemure, 2007; Roto *et al.*, 2004), components in magnetic or optical solid-state devices (J. H. Lee *et al.*, 2009; L. Li *et al.*, 2007; L. Song *et al.*, 2016), gas detectors (Ai *et al.*, 2008; Chen *et al.*, 2008; Hassanein *et al.*, 2017) and photovoltaics (L. Zhang *et al.*, 2014).

In this thesis, the synthesis and fabrication of mesoporous Zn/Al-LDH layer are demonstrated via adapted co-precipitation approach in which the characteristics of fabricated film is different to the powdered form of Zn/Al-LDH nanoparticles and hence give rise to novel applications. As a layered material, well designed synthesis process of LDH crystallites can led to well distributed continuous mesoporous layer morphology which is considered beneficial for DS photodetectors since it offers highly porous materials.

2.1.2 Mixed metal oxides

Metal oxide semiconductors are well-thought-out as one of the greatest crucial and commonly employed in optoelectronic devices, either as an active sensing element phase or as support. These semiconductors are utilized for both their redox and acid phase characteristics (Bond, 1962; Kung, 1989). Single metal semiconductor oxide can be crystallized with more than one crystal phase (amorphous, polycrystalline or crystalline). Metal oxide semiconductors can be prepared at room temperature (RT); however, several crystal phases can continue being amorphous especially at low thermal treatment temperature. Most of single component metal oxide materials are prepared with either crystalline or highly pure polycrystalline morphologies and their surface can be oriented as M-(), M-O, M-O-M or M-OH functionalities, whereas M-() presents a vacancy of oxygen (Gawande *et al.*, 2012).

Metal oxide materials, in particular, which contain more than one type of metallic cations are defined as mixed metal oxides (MMOs). MMOs is normally obtained as binary, ternary, quaternary, etc. with respect to different metal cation numbers (Marrs *et al.*, 2011). MMOs are further classified based on their crystal phase (crystalline, polycrystalline or amorphous). When the oxide materials are polycrystalline or crystalline, their crystal structure is used to define the oxide materials composition.

Perovskites, for example, are expressed by the well-known formula of scheelite (ABO_4), spinels (AB_2O_4) and plameirites ($A_3B_2O_8$). The unlike MMOs' metal cations (M^I and M^{II}) are presented as $M^{I\ n+}-Ox$ and $M^{II\ n+}-Ox$. These forms of MMOs are coupled in many ways like edge or corners sharing which in turn forms chains such as $M^{II}-O-M^{II}-O$, $M^I-O-M^{II}-O$ or M^I-O-M^I-O (Gawande *et al.*, 2012). Figure 2.3 illustrates a schematic representation of general MMO chain structure. Cations arrangement of a particular element varies by the nature and co-ordination of cations of the neighbor which in turn governs the kind of the cations bonding. Diverse environment of the metal cation which constitutes as a dynamic center can contribute with rise to many types of reactivity towards a desirable molecule. It is also difficult to estimate which cation demonstrate the main role of the active center in MMO matrix, however, the molar ratio of the metal cations can give rise to dominant constitute metal cation.

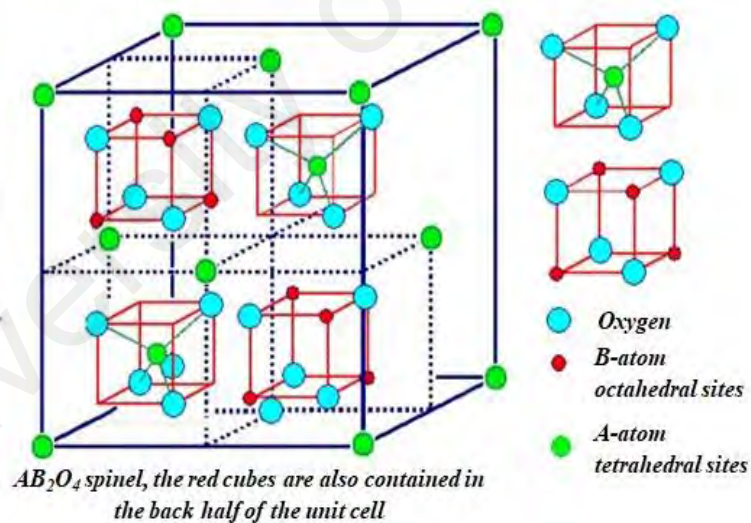


Figure 2.3: The general structure of a typical ordered MMO where A^{+2} and B^{+3} atoms occupy tetrahedral and octahedral holes, respectively (Issa *et al.*, 2013).

MMO semiconductors show a very significant role in many applications due to the unique features such as wide band gap, high surface area, fast electron injection, high purity (Salih *et al.*, 2018). Nevertheless, these materials give a great potential in large scale manufacturing due to their high purity, good quality control and extreme low cost

(Gawande *et al.*, 2012). MMO semiconductors has been one of the greatest rapidly growing research areas in chemistry aiming to organize these materials into uniformly distributed cations as a thin film or powder forms for the purpose of advancing new applications such as catalyst, (Yuan *et al.*, 2017), lithium ion batteries (F. Wu *et al.*, 2015), elements in optical and magnetic devices (Carja *et al.*, 2010) and solid-state devices (J. Cao *et al.*, 2017; Cao *et al.*, 2016; Foruzin *et al.*, 2016; L. Zhang *et al.*, 2014). There are many preparation methods of MMOs, for instance wet impregnation (Reddy *et al.*, 2001), hydrothermal method (Ajaikumar & Pandurangan, 2009), sol-gel (Elia *et al.*, 2011), mechanochemical synthesis (A. Tang & Zhang, 2006) and co-precipitation (D. Jiang *et al.*, 2010). Among these methods, thermal treatment of LDH can be of outstanding results due to very easy process, low cost and easy handling. Thermal treatment of LDH gives rise to MMO with desirable features such as high surface area, good electron injection efficiency, high photo-response properties, and high temperature stability.

In this thesis, MMO was prepared in the form of AB_2O_4 structure ($ZnO/ZnAl_2O_4$) using Zn/Al-LDH as precursor. Thermal treatment of Zn/Al-LDH can lead to the 2D layered structure collapse and subsequently a formation of $ZnO/ZnAl_2O_4$ -MMO which demonstrates a high specific surface area and many attracting features as mentioned above (Foruzin *et al.*, 2016; L. Zhang *et al.*, 2014) which in turn enhance the dye absorptivity and improve the device photo-responsive behavior. With well-established synthesis approaches of Zn/Al-LDH, finally $ZnO/ZnAl_2O_4$ -MMO can be acquired in mesoporous continuous film structure via thermal reduction approach due to the systematically distribution of the metal cations in the Zn/Al-LDH brucite layers.

2.1.3 Phase transformation of LDH to MMO

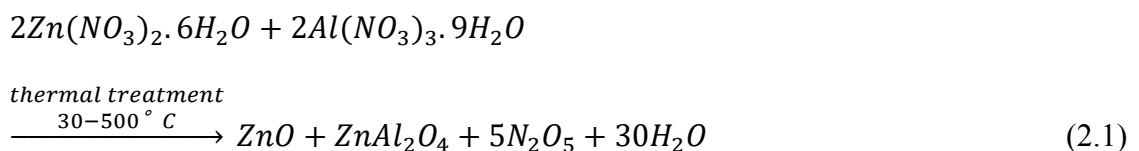
A diversity of LDH in nanomaterials form were established with outstanding properties which are considered useful for several energy conversion and storage applications. As already presented in section 2.1.1 and 2.1.2, MMO driven from thermally-treated LDH can be employed in catalysts, electrode materials for supercapacitors, optical, magnetic, sensor devices and other forms of solid-state devices. One of the key features that make MMO-based LDH is of great interest for energy conversion and sensing solid-state devices is that the uniformly distributed ions, which are located at the atomic structure, as well as the ions relatively open structure, enhance the movement of the charges.

Thermal treatment of $M^{II}M^{III}$ ions in the LDH is considered as a substitute pathway to the well-known physical and chemical procedures for the synthesis of a wide range of MMO semiconductor materials which contains metal oxide semiconductor ($M^{II}O$) and spinel phases ($M^{II}M^{III}_2O_4$). The characteristics of the consequential MMO semiconductors are to be considered greater to others which are synthesized by well-known physical and chemical methods (X. Zhao *et al.*, 2010). A deep understanding of the transformation mechanism of LDH as precursor to MMO phase is vital if the characteristics of the latter are of effective influence for specific applications.

The Zn/Al-LDHs decomposition has a number of attracting properties, the solid-state transformation from ZnO into $ZnAl_2O_4$ spinel (wurtzite and cubic structure, respectively) (Fan *et al.*, 2009) is not a random transformation procedure where these randomness may lead to some losses or gain boundary of material, which in turn makes the final lattice of the resulting MMO related to that of the original precursor (Zn/Al-LDH) by one or more crystallographically equivalent. Subsequently, both Zn and O migration is occurred through the decomposition of Zn/Al-LDH and ZnO

transformation into ZnAl₂O₄ spinel (Fan *et al.*, 2009). The major structure of the formed ZnO/ZnAl₂O₄-MMO called natural. Natural ZnO/ZnAl₂O₄-MMO materials ought to have divalent cations (Zn⁺²) and trivalent cations (Al⁺³) in tetrahedral and octahedral voids, respectively (Dwibedi *et al.*, 2018). The main stages of Zn/Al-LDH transformation into ZnO/ZnAl₂O₄-MMO are illustrated in Figure 2.4 and also summarized as follows:

- i. **Stage one:** starting at room temperature, RT ~30 °C, to nearly 180 °C, Zn/Al-LDH precursor is dehydroxylated which is occurred with the layer structure sustained (Ali Ahmed, Talib, *et al.*, 2012a; Chai *et al.*, 2009);
- ii. **Stage two:** the nucleation of ZnO phase occurs with the 2D structure of Zn/Al-LDH destructed. This happens together with ZnO particles became homogeneously distributed in oxide polycrystalline phase. Higher thermal treatment temperature level leads to favorable ZnO phase orientation growth. During this process, ZnO crystallinity rise importantly and residual amorphous phase fall to almost zero (Hassanein *et al.*, 2017; Van der Laag *et al.*, 2004);
- iii. **Stage three:** this stage is related to recrystallization, nitrate ions decomposition in the interlayer of LDH, and the existence of ZnAl₂O₄ brucite phase (Chai *et al.*, 2009). ZnAl₂O₄ nanoparticles are considered to be dispersed in the ZnO semiconductor unbroken phase; subsequently, the advancement and oxidation of ZnO phase and ZnAl₂O₄ spinel could be acquired at relatively high thermal temperatures (Salih *et al.*, 2018). The overall synthesis performance can be expressed as follow:



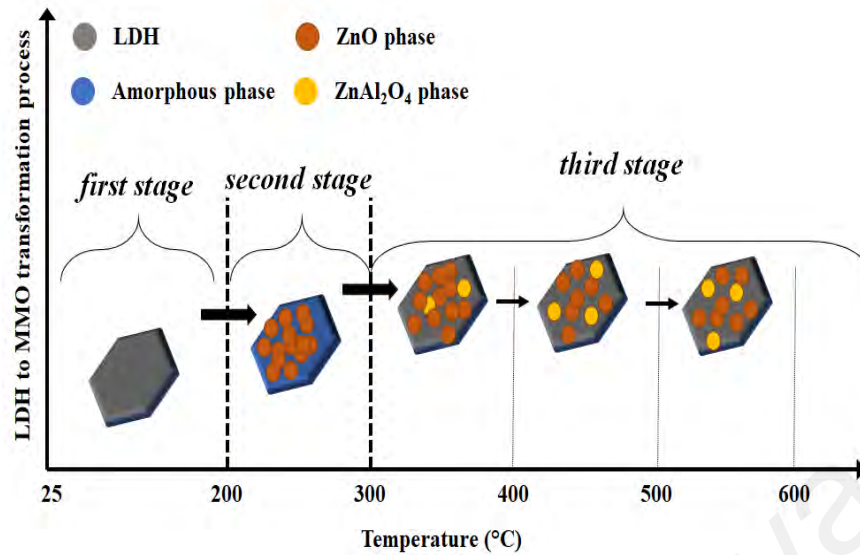


Figure 2.4: Schematic representation of the phase transformation of LDH precursor into the ZnO/ZnAl₂O₄-MMO.

2.2 Photodetector

In this section, the photodetector photo-responsive characteristics and parameters are discussed thoroughly. Later, types of photodetector with some literature overview are presented.

2.2.1 Photodetector current-voltage characteristics

Photodetector current-voltage characteristics are very similar to the well-known rectifying diode in term of its electrical characteristics. Therefore, the photodetector very often referred to as photodiode. In contrast to photo-voltage solid-state devices such as solar cells, the photodetector typically is functioned by external applied potential voltage, bias voltage. Equation 2.2 describes a photodetector current-voltage behavior that consisting of organic and inorganic materials under dark condition (Rauch, 2014):

$$I_D = I_S \exp\left(\frac{qV}{nK_B T}\right) - I_S \quad (2.2)$$

herein, I_D represents the photodetector current (ampere, A), while I_S which is applied through thermal assisted injection is considered a saturation current (A), q is electron absolute charge (1.6×10^{-6}), V is the bias voltage across the photodetector, n , K_B and T are the ideal factor of a photodetector, Boltzmann's constant and temperature (kelvin), respectively. The photodetector current-voltage characteristic is to be categorized into three main separate regions depending on the applied bias voltage:

i. Forward biased voltage region: when the applied biased voltage is forward through the photodetector (FTO-sensing film is exposed to a positive bias voltage and FTO-Pt is negatively exposed to bias voltage), an exponential increment in the current is acquired. In this case, the first part [$I_S \exp(\frac{qV}{nK_B T})$] of Equation 2.2 demonstrates an exponential increment in the current. Subsequently, it controls the second part of Equation 2.2 (I_S). Hence the second part (I_S) is normally small, Equation 2.2 of a photodetector is expressed as Equation 2.3:

$$I_D \approx I_S \exp\left(\frac{qV}{nK_B T}\right) \quad (2.3)$$

ii. Unbiased condition: in the unbiased condition, the photodetector is operated as typical solar cell, where the current is considered negligible through the photodetector circuit.

iii. Reverse biased condition: when the applied bias voltage is reversed through the photodetector (FTO-sensing film is exposed to a negative bias voltage and FTO-Pt is positively exposed to bias voltage), the ideal saturation current of particularly small magnitude moves through the photodetector. However, the signal-to noise ratio is limited as the phenomenon of the charge injection attends as dark current basis, especially when if this phenomenon applied from the electrode to the detecting film. Generally, a photodetector, which is under reversed bias condition, works in certain

bias-range of applied voltage. If the applied potential is augmented to a level which is above the threshold voltage, only then, the current that flow in photodetector rises dramatically, in which case the photodetector is placed in breakdown region. It must be mentioned that Equation 2.2 only expresses the current-voltage characteristics of the photodetector in its dark condition by which Equation 2.2 is not applied for the photocurrent (once exposed to photon influx) through the photodetector. Once a photon influx is applied to the photodetector, the detecting film of the photodetector absorbs all the light (wavelength range as the photodetector designed). Continuously, an exponential decay in light is obtained as the light goes through the detecting film. After the light goes through certain distance x in the detecting film materials, the power density of light is represented by Beer's law (Ahrenkiel *et al.*, 1988),

$$P(x) = P_o \cdot \exp(-\alpha(\lambda) \cdot x) \quad (2.4)$$

herein, P_o and $\alpha(\lambda)$ are the light power density and absorption coefficient spectral dependent of the detecting film (FTO-sensing layer)

Equation 2.5, which describes a maximum photocurrent magnitude through a photodetector, is only applied when the charge carriers' generation is sufficient, by which all absorbed photons take place in the photocurrent generation.

$$I_{ph} \sim I_{max}(d, \lambda) = \frac{qP_oA}{hv} (1 - \exp(-\alpha(\lambda)d)) \quad (2.5)$$

herein, λ represents incident light wavelength while d is sensing film actual thickness.

The produced photocurrent in a photodetector is expressed by Equation (2.5). In the illumination of light condition, the current of the sensing film (semiconductor) is enlarged and a dramatically shift is obtained in the current-voltage curve. In this case,

Equation (2.6) describes the photocurrent in reverse bias condition (I_m) (Lei Luo *et al.*, 2006),

$$I_m = I_D - I_{ph} \quad (2.6)$$

herein, the photocurrent of the photodetector is represented by I_{ph} . Figure 2.5, illustrates the typically obtained current-voltage characteristics of photodetector in both conditions. Although, it is clear to be noticed that during dark state ($\phi = 0$), the amount of dark current is identically low that streams in a photodetector. The generated photocurrent upsurges as the light illumination power (ϕ) growths by which the photo-detection behavior is generated.

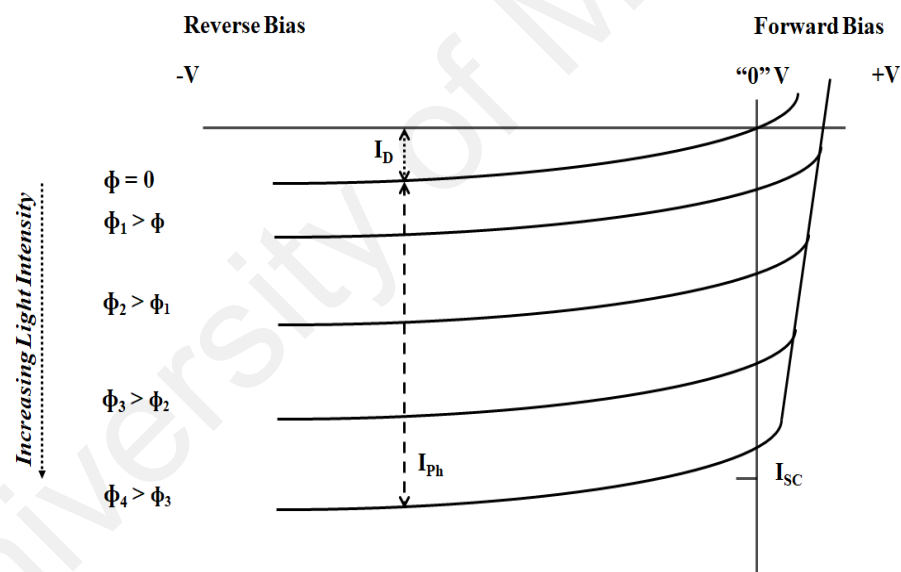


Figure 2.5: Current-Voltage characteristics schematic illustration.

2.2.2 Photodetector sensing parameters

The photodetector key-sensing parameters are discussed and listed in details below:

i. Spectral response: this type of photodetector key-sensing parameter approximates the amount of photo-current generated by certain wavelength which presumes that all incident wavelengths produce similar intensity of light. It is also considered that the

frequency bandwidth of a photodetector response to a certain bandwidth range. During the fabrication of DS photodetector, therefore, it must be considered to select suitable photo-active semiconductor (in the inorganic part) and visible light sensible organic materials. In the present study, only visible light was taken into consideration. Thus, while DS photodetector fabrication, UV-Vis analysis was employed to investigate the spectral response of the sensing film that contains both the anode materials and photo-active organic materials (prior to the device fabrication).

ii. Photo-responsivity: Another crucial parameter is the photo-responsivity R (expressed in A/W) which is a figure to estimate the behavior of a photodetector, also, typically, the photo-responsivity is described as a proportion of generated photo-current to the illumination power. It is particularly stated as the following Equation (Xie, 2013).

$$R = \frac{I_{ph}}{P_{in}} \quad (2.7)$$

herein, the generated photocurrent is expressed by the symbol I_{ph} while the measured illumination power is represented as P_{in} (expressed in Watt/cm²). The incident light conversion into measureable electrical signal is to be, typically, evaluated by calculating the photo-responsivity. The wavelength, on the other hand, plays an essential role in elevating the photo-responsivity, as well as the applied bias voltage, temperature, and illumination power.

iii. Photo-conductivity: The photo-conductivity S is another important property of the photodetector and it is defined as the increment in the electrical conductivity of specific materials as these materials became visible to light of adequate amount of energy (expressed in Sm/W). Photo-conductivity attends as a factor to estimate the inner processes in the fabricated photodetector as well as the photo-conductivity is broadly

employed to sense the existence of light and evaluate light intensity in optoelectronic solid-state devices. It is expressed as (2.8) (Qadir *et al.*, 2014; Xie, 2013),

$$S = I_{ph}T/P_{in}AV \quad (2.8)$$

whereby, I_{ph} is the photo-current generated during illumination condition, the sensing film thickness is expressed by T and P_{in} is the illumination power intensity (W/cm^2). The active area of the fabricated sensing film is represented by A (cm^2) while V is the applied bias voltage (V).

iv. Photo-detectivity: The photo-detectivity (D^*) is a figure of merit of a photodetector, it is also known as the noise equivalent power (NEP). In other words, the photo-detectivity outlines the lowest impinging optical power intensity that a photodetector is able to detect out of the generated noise. The photo-detectivity can be expressed as:

$$D^* = (A \Delta f)^{1/2} R / i_{in} \quad (2.9)$$

whereby R is the photo-responsivity (A/W), i_{in} is the noise current (A).

There are three main contributions in the noise which limits D^* : Johnson noise, shot noise and thermal fluctuation noise (X. Gong *et al.*, 2009). If the dark current shot noise is the only contributor, the detectivity then can be written as:

$$D^* = R / (2qI_D)^{1/2} = (I_{ph}/P_{in}) / (2qI_D)^{1/2} \quad (2.10)$$

The photo-detectivity can be calculated based on the measured photocurrent (A), dark current (A) as well as illumination power intensity (W/cm^2).

v. **Effective quantum efficiency:** The effective quantum efficiency (EQE), differs from external quantum efficiency, is considered as the product of the external quantum efficiency as well as the total gain of photodetector. EQE can be expressed as:

$$EQE(\%) = (I_{ph}/q)/(P_{in}/hv) \times 100 \quad (2.11)$$

In other words, EQE is the fraction of photons that mainly contribute to the photocurrent output (S. H. Yu *et al.*, 2014).

vi. **Switching behavior and spatial and temporal time response:** the response time of a photodetector is defined as the actual time needed by the photo-current to rise from 10 to 90%, while the recovery time is the time taken for the photo-current to reach its initial state from 90 to 10%. A good quality photodetector must demonstrate fast response and slow recovery times. The photodetector recovery time powerfully depends on the bias voltage applied; increment of the electric field causes the charge carriers to be firmly swept out of the photodetector under test (Valouch *et al.*).

vii. **Photo to dark current ratio:** additional crucial parameter is the ratio of photo to dark current (I_{ph}/I_D) for a photodetector. As aforementioned, the term the term (I_{ph}) represents the photo-current generating as a result of uninterrupted extraction and photo-generation of unbounded charge carriers, especially, if a photodetector is become visible to suitable light illumination source. The term (I_D), however, represents the current that streaming under dark condition in the photodetector. Higher ability of noise rejection is obtained if the ratio photo to dark current is, typically, high (Tzeng *et al.*, 2010). The ratio of photo to dark current can be manipulate via leakage current condoling, since the amount of the photo-current is initially dependent on the prepared photoactive materials structure that used in the fabrication of photodetector.

viii. Dark current: Generally, photodetectors are functioned under applied bias by which an electrical signal is generated, whereas the illumination light absence is not effective in this case. In fact, this electrical signal is generated because of the prepared sensing film with the existence of heat (higher than zero, RT for example). Herein, this electrical signal is denoted as the current under dark condition (I_D). Generally, if the applied bias voltage is large, the dark current will be increased as a result. The dark current causes a limit of the subsequent ability of detection to sense low signals generated by the photodetector, in other words low photo-detectivity value (Yotter & Wilson, 2003).

2.2.3 Photodetector operation modes

The applied bias voltage condition determines the mode of operation for a photodetector, in which two types of modes are discussed, particularly (i) photovoltaic mode as well as (ii) photo-conductive mode.

i. Photovoltaic mode: in this type of operation mode, typically, various light illumination power is applied on the photodetector with zero biased function. The main advantage of this type of operation is that the ratio of photo to dark current is high, low magnitude of current under dark condition. Particularly, for sensing materials, a band gap of ~ 2.7 eV encounters the anticipations of extremely low level of noise and subsequently wide dynamic range especially when operating with the photovoltaic mode (Schilinsky *et al.*, 2004). The incident flux of photons absorption provides increase in the electron hole pairs phenomenon, by which mobile charges are generated due to build in electric field. This electrical field is generated by the donor/acceptor semiconductors electronegativity values differences. The entire process, eventually, causes the short circuit current and/or photo-voltage through the photodetector under test. The short circuit current and/or photo-voltage through a photodetector finally rise with the

illumination light increment, in which the photovoltaic operation mode basis is formed in the photodetector.

ii. Photo-conductive mode: in the photo-conductive operation mode, conversely, usually not necessarily, the photodetector is exposed to variety if illumination powers with bias condition applied. The mobility of charge carriers phenomenon towards both electrodes, anode and cathode, is accelerated by an external electric field, which is in a perfect direction of the build in field. Consequently, the value of dark current is increased and subsequently the response time is decreased as a result of the applied bias voltage through a photodetector. Although, the dark current increment is well-thought-out as disadvantage, the main dark current contributor in hybrid photodetectors is the injection of charge and thus this issue could be avoided using an interfacial layer (Y. J. Kim *et al.*, 2014; H. Zhang *et al.*, 2015).

Typically, an optoelectronic device, photodetector, is generated in photovoltaic operation mode only if a low level of noise is required. However, the photo-conductive operation mode of generation is employed if a high speed of response is needed. Therefore, in the current study, both modes were used; in which the photo-responsive behavior was conducted under both 0 and +0.2 V biasing conditions.

2.2.4 Types of photodetector

Various literatures show that photo sensing feature has been widely applied for light sensing application. This subtopic dictates briefly the architecture of the device and sensing mechanism associated with photodetectors.

2.2.4.1 Organic photodetectors

Over the decades, researchers have been exploring the attractive properties of organic optoelectronic devices in the scope of photodetectors domain. C.W.Tang (C. W.

Tang, 1986) reported the initial discovery of light harvesting optoelectronic device in 1986. It was built with donor-acceptor (D/A) heterojunction as base. Since the initial discovery, the development pace of solution-processed polymer blend organic photodetectors was rapid. The inter-perforation blend of donor (D) and the acceptor (A) is defined as bulk heterojunction. In general, donor (D) is a material with low ionization properties; meanwhile acceptor (A) is a material with relatively high electron affinity and electron mobility (Jailaubekov *et al.*, 2013; K. Kim *et al.*, 2017). Besides that, $-D'$ material features high hole mobility and $-A''$ possesses high electron mobility. In order to combine the exciting and promising physical and electrical properties of two individual components, the polymer blending techniques was invented. Bulk heterojunction offers the capability of fine tuning the optical characteristics of the blend film such as tunability of wavelength. This is often identified as the major benefit of bulk heterojunction concept. Controlling the optical properties delivers photodetectors with responsive spectral range for specific application. For example, controlling of the optical properties delivers photodetectors with specific range for light detection application. Besides that, for visible light detectors, the extension of visibility range for absorption spectra of photo-active film shall be easily done by the blending technique, comprising the specific optical characteristics. The electrical properties of $-D'$ and $-A''$ material highly influence the sensing parameters of organic photodetectors. Following are the key properties of the materials that are highly influential: (i) the mobility of charge carriers, either hole or electron mobility (ii) the level of energy of $-D'$ and $-A''$ materials.

The composition of strategically selected pair of conjugated polymer $-D'$ and $-A''$ material will initiate high photon induced charge generation and recognizable transfer of charge (Skotheim & Reynolds, 2006). In the occurrence of judicious $-D'$ and $-A''$ material blending as photoactive film, the efficiency of photon-to-electron conversion and the photo sensitivity is expected to increase.

Generally, there is a predicament that the formation of photo-generated exactions was firstly evolved in the photo detection mechanism of BHJ photo detectors. After that, as second phase of this process, the photo-generated exactions diffuse to the $-D''$ and $-A''$ interface. Upon diffusion the exactions are dispersed into their constituent electrons and holes. The dispersion then leads to generation of photo-current at the $-D''$ and $-A''$ interface (Jailaubekov *et al.*, 2013; G. Yu *et al.*, 1994). The low unoccupied molecular orbitals (LUMO) with higher electron affinity attract the electrons. Meanwhile, highly occupied molecular orbitals (HOMO) which possess lower ionization potential attract the holes. As final stage, both the separated charges are transported together to the electrodes. This transportation will generate photocurrent in the connected external circuit. In summary, the photo detection mechanism comprises the generation, diffusion and separation of exaction and finally the carriage of charge carriers to the respective electrodes.

2.2.4.2 Inorganic photodetectors

This subtopic reviews several numbers of latest findings and development in the scope of narrow and wide band gap semiconductor, focusing on IR and UV photodetectors. Besides that, the details of photodetectors based on inorganic nanostructures also discussed in this subtopic.

i. Narrow band gap semiconductors: Currently, for utilization of ultrafast and highly sensitive photo-detection, infrared (IR) photodetectors are commercially available. Commonly this IR photodetectors are either Silicon (Si), amorphous inorganic semiconductor (Lhuillier & Guyot-Sionnest, 2017; Schubert *et al.*, 2011; Suzuki *et al.*, 2003), or narrow band gap (III-V) semiconductor such as GaAs, GaAsP and GaP (Lhuillier & Guyot-Sionnest, 2017; Mikulics *et al.*, 2003). Above mentioned detectors are found to have high ratio on photo/dark current (I_{Ph}/I_D) and displays highly

significant photo-responsivity. Besides that, practical evidences show that photodetectors developed based on crystalline Si are more pervasive and readily available in commercial markets, besides being mature in terms of technology (Soref, 2006). Beam epitaxy (MBE) is the common industrial process used for the mass production of these photodetectors (Konle *et al.*, 2001). For the production of photodetectors (PDs) in integrated array form, the CMOS silicon-on-insulator (SOI) units are used. In the advanced scope, the Si technology gives way to the monolithic assimilation of the detector, in parallel with the electronic circuit on the same Si substrate (Zimmermann, 2009). Thus, it can be concluded that image sensors and PDs developed based on Si are promising option in determining the improvised performance of electronic components despite the high price range.

ii. Wide band gap semiconductors based PDs: Semiconductors like SiC, certain II-V compounds and III-nitrides are prominent option for the UV photo-sensing application, due to their wide band gap virtue (Omnès *et al.*, 2007). Comparing narrow and wide band gap semiconductor thermal conductivity, the wide band gap semiconductors (WBG) has relatively higher thermal conductivity. Thus, the WBG semiconductors are classified as the most suitable unit for applications with high power and temperature (due to the highly energized UV radiation exposure) (Monroy *et al.*, 2003; Pan *et al.*, 2017). However, there are two utmost drawbacks on narrow and wide band gap semiconductors. Firstly, as reported by (S. Chang *et al.*, 2008) and (S.-H. Chang *et al.*, 2008), they are dependent on substrates such as Si, sapphire and SiC, which are relatively expensive. To be specific, for processes involving WBG semiconductors, lattice matched substrate type is mandatory for the growth of epitaxial (Yoshikawa *et al.*, 2007). Secondly, both PDs generate unnecessary IR or UV sensitivity (Yoshikawa *et al.*, 2007) such as unwanted noise the photo-detection's visible wavelength (Casady & Johnson, 1996; Millan *et al.*, 2014), due to the band gap difference than that is

required for visible detection. A Si semiconductor has smaller band gap meanwhile a WBG semiconductor has larger band gap.

iii. Inorganic nanostructures: One-dimensional (1D) inorganic nanostructures have been widely explored to study their suitability in light sensing application (Z. He *et al.*, 2010; Jie *et al.*, 2010) besides other inorganic semiconductors. 1D nanostructures offers improvised responsivity to lights (Zhai, Fang, *et al.*, 2010; Zhai, Li, *et al.*, 2010). This is because of the small size and large surface to volume ratio compared to the Debye length. Moreover, the mean duration of diffusion of photo-excited charge carriers, from the interior to the oxide nanowire surface is also observed with noticeable reduction (Kolmakov & Moskovits, 2004). Dimension of nanostructure (Prades *et al.*, 2008) and material are the two factors that influences band gap. Thus, the adjustment of active or blind spectral regions of the PDs can be done via fine-tuning the band gap of the nanostructure materials. Precisely, evidences show that CdSe (Z. He *et al.*, 2010; Y. Jiang *et al.*, 2007) and In_2Se_3 (Zhai, Fang, *et al.*, 2010) are examples of nanostructures that displays improvised photosensitivity in range of visible wavelength.

Besides 1D, metal oxide nanostructures are also accounted as a research scope for optoelectronics (Sahoo *et al.*, 2009). Nano-structure is a scope that comprises nanowires, nano-ribbon, nano-belts and nano-tubes (Umar & Hahn, 2010). By comparing the nano-level dimensions and bulk counterparts, metal oxide shows outstanding characteristics in terms of wide band gap, transition of reactive electronic and high dielectric constants. Yet, researches show that the synthetic technology of these nanostructures is often complex. For instance, the synthetic techniques commonly applied for these nanostructures are sputtering, laser ablation, hot filament metal-oxide vapor deposition (HFMOVD), chemical vapor deposition (CVD), vapor-liquid-solid (VLS) and thermal oxidation (Devan *et al.*, 2012).

vi. Colloidal quantum dots: In recent studies, technology advancement and explore in colloidal quantum dots (CQDs) has resulted in beneficial photodetector responsivity, especially in the spectral regime where inability of Si to absorb light presents. CQDs are observed to befitting with low temperature processing, besides being easily integrated with flexible and rigid substrates. CQDs are materials that gain utmost advantage from the quantum confinement phenomenon. This enables the charge carriers in CQDs to constitute distinct energy levels, synonym to an atom's electron. Besides that, the band gap of the material (Konstantatos *et al.*, 2006; Konstantatos & Sargent, 2011) can be adjusted via the effect of the quantum size. The adjustment of band gap will then result in the improvising of photodetector sensitivity in the visible spectrum.

2.2.4.3 Hybrid inorganic-organic photodetectors

Hybrid organic-inorganic PDs have been also studied on their application in optoelectronic field. p-type and n-type photo-sensing film, organic and inorganic components respectively increases the functionality of the PDs despite overcoming their independent deficiency. Hybrid sensing film features ease of chemical tune-ability besides allowing processing at low temperature and cost-effective. In general practice, organic semiconductor based devices are opted well for economical, low weight and environmentally benign PDs. Despite the good terms, organic semiconductors possess low mobility of charge carriers and poor separation of exactions. This deficiency often lead to poor photoconductive gains and responsivity of the PDs (Chung *et al.*, 2013). Meanwhile, for inorganic semiconductors, they are highly distinguished for the high electron mobility attribute. Herewith, when the organic and inorganic semiconductors are combined together to generate a hybrid sensing film, huge interface area for charge separation is formed. Due to the high mobility of n-type inorganic semiconductor, the extended charge separation and high charge transport is obtained in hybrid sensing

films. This will then hamper the recombination losses (Huynh *et al.*, 2002; Kalita *et al.*, 2009). Organic-inorganic hybrid PDs also are observed with sustainable device stability.

Besides the above mentioned devices, the inorganic PbS, Cu-In-Se, and CdS nanostructures are also applied to the adjustment of sensing parameters (Jarzab *et al.*, 2011; Lin *et al.*, 2011; Luszczynska *et al.*, 2013; X. Wang *et al.*, 2013). Although the Si nanowires are found to be eco-friendly (Huang *et al.*, 2009), they require expensive and complicated fabricating techniques, at high temperatures such as CVD, laser ablation and VLS (Huang *et al.*, 2009). Similarly, the dye-sensitized photodetector is operated on a similar basis of hybrid photodetectors with minor differences. Since the main focus of this study is the DS photodetector, thus a thorough detail on the recent literature, structure and working mechanism of DS photodetector is demonstrated in section 2.3.

2.3 Dye-sensitized photodetector

Recently, semiconductor photodetectors based dye-sensitizer have fascinated noteworthy consideration in research society because of their superior features such as long term photo-carrier lifetime and high light sensitivity as compared to other types of photodetectors. Moreover, dye sensitization technique offers an alternative approach aiming at the enhancement of the device spectral response and improves its photo-responsive behavior. The newly proposed DS photodetectors have been investigated thoroughly in last few years because of low fabrication cost, flexibility and suitability as well as easy process handling (Gao *et al.*, 2013; Parreira *et al.*, 2012; Qadir *et al.*, 2014; Qadir *et al.*, 2015; Teng *et al.*, 2016; Z. Wang *et al.*, 2011; S. H. Yu *et al.*, 2014). The DS photodetector offers an economically and technically reliable alternative model as compared to other photodetectors' geometries.

The working mechanism of the DS photodetector is very alike to dye-sensitized solar cell (DSSC) which was firstly reported by O'regan and Gratzel in 1991 (O'regan &

Grätzel, 1991a). In contrast to the conventional photodetector geometry where both absorption of light and charge transfer are assumed by the semiconductor, in DS photodetector both functions are individually handled. In particular, light absorption is assumed by the sensitizer, which is desorbed from a wide band gap semiconductor surface. Continuously, the charge separation phenomenon is generated by the photo-induced injected electron from the molecules of sensitizer into a conduction band (CB) of a metal oxide semiconductor. Hereinafter, the charge carriers are transported from the semiconductor CB to another electrode. The main benefit of the sensitizer is the broad band wavelength (visible light) absorption in conjunction with mesoporous morphology oxide layer. Table 2.1 summarizes an overview of the sensing parameters for most recent DS photodetectors based on different types of semiconductors.

Table 2.1: Brief of the materials type and sensing parameter used in DS photodetector.

Semi-conductor	Dye	photocurrent (mA)	Photo-responsivity (A/W)	Reference
TiO ₂	N719	-	0.15	(Z. Wang <i>et al.</i> , 2011)
TiO ₂	N719	1.4×10 ⁻³	-	(Parreira <i>et al.</i> , 2012)
TiO ₂	C1-LEN	1.0×10 ⁻³	-	(Parreira <i>et al.</i> , 2012)
TiO ₂	C2-LEN	1.8×10 ⁻⁵	-	(Parreira <i>et al.</i> , 2012)
ZnO	TiO ₂	1.3×10 ⁻³	3.5×10 ⁻²	(Gao <i>et al.</i> , 2013)
MoS ₂	R6G	1.0×10 ⁻⁹	0.9	(S. H. Yu <i>et al.</i> , 2014)
TiO ₂	NiTsPc	~1.5×10 ⁻⁴	~4.0×10 ⁻³	(Qadir <i>et al.</i> , 2014)
TiO ₂	MEH-PPV	~4.7×10 ⁻³	~4.7×10 ⁻⁵	(Qadir <i>et al.</i> , 2015)
TiO ₂	PCPDTBT	~1.1×10 ⁻³	~1.1×10 ⁻⁵	(Qadir <i>et al.</i> , 2015)
MoS ₂	Graphene	1.2	1.0×10 ³	(Y. Lee <i>et al.</i> , 2015)
MoS ₂	N719	0.4	4.0×10 ²	(Y. Lee <i>et al.</i> , 2015)
ZnO	Perovskite	2×10 ⁻⁵	0.1	(F. Cao <i>et al.</i> , 2017)
ZnO	RhB	0.1	0.9	(Bai & Liu, 2017)
ZnO NRs	ZnS	0.5×10 ⁻³	0.5×10 ⁻²	(Sarkar <i>et al.</i> , 2018)

2.3.1 Dye-sensitized photodetector structure

In order to understand the DS photodetector working mechanism, DSSC is originally presented since all the concepts of DS photodetector are alike to that of DSSC. DS photodetector is, typically, consisted of reasonable materials in which these materials are eco-friendly and cost effective. The main components in DS photodetector are illustrated in Figure 2.6. Particularly, **two conductive substrates** which are normally coated using FTO. These two substrates offer a robust construction and provide a complete short circuit of the fabricated device. A **photoanode** or **working electrode** (sensing film) which is one of the main electrodes (FTO) and it is consisted of layer that contain the metal oxide semiconductor colored (sensitized) with particular **dye**. The dye (sensitizer) specifically anchored in a porous layer and its main function is that absorbing the incident photons and roles as the harvesting component. Its main function is to absorb a photon and subsequently inject the absorbed photon into the CB of the metal oxide layer leading it to its excited state. The second electrode is **photocathode**, which is also known as the counter electrode, it is consisted of thin layer (usually carbon or platinum) deposited on the conductive side of the glass substrate (FTO). Finally, the **electrolyte**, which scientifically named the redox mediator, it is placed in between both electrodes (working electrode and counter electrode). Its main function is to provide the sensitizer with an electron when the sensitizer injects electron in the CB of the metal oxide layer. All these gears and working mechanisms are discussed thoroughly in the following subsections:

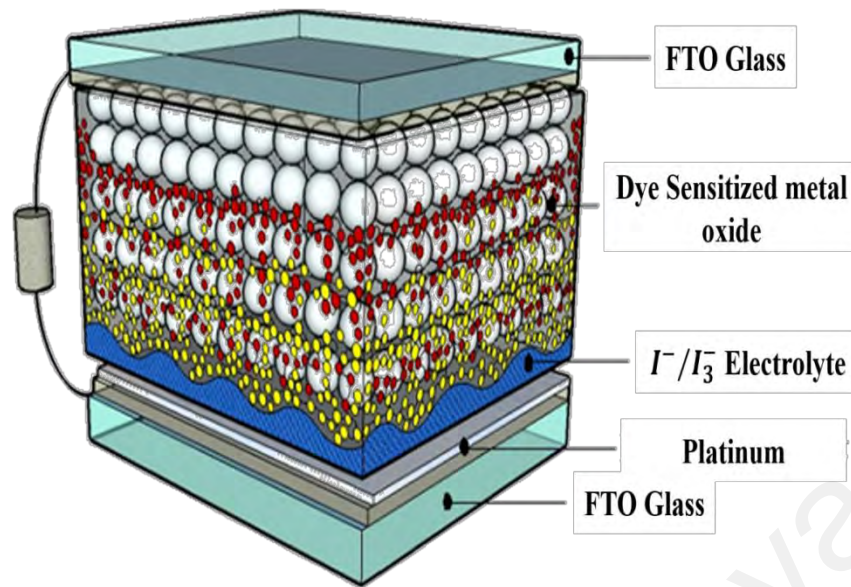


Figure 2.6: Schematic representation of a typical DSSC function and structure.

2.3.1.1 Photoanode

The photoanode mainly consists of two types of components; metal oxide semiconductor and sensitizer. A detailed illustration for each component is demonstrated below:

i. The sensitizer: the sensitizer serves as the photons main absorber in optoelectronic devices. The sensitizer features are of great influence on photons harvesting as well as the total photo-current output. A perfect sensitizer that used in DS photodetector ought to absorb all incident light under wavelength of 720 nm. Nevertheless, the sensitizer must be ideally loaded onto the metal oxide layer surface (working electrode). The sensitizer HOMO level must be greater in term of energy than the CB of metal oxide layer so that an effectual electron transfer phenomenon between the HOMO of the sensitizer and CB of the metal oxide layer can be occur (Hagfeldt *et al.*, 2010). Its redox potential also ought to be adequately high that it can be sufficiently and rapidly regenerated by electron from the electrolyte that placed between the two electrodes (Hagfeldt & Grätzel, 2000).

Based on the needs proposed by a successful optoelectronic device, many types of photosensitizer have been investigated. Among these, metal complexes and ruthenium (Ru(II)) complexes, specifically, have been thoroughly explored due to the broad wavelength absorption range as well as promising photovoltaic behavior. In general, metal complexes sensitizers are consisted of a main metal ion together with ancillary ligands that having as a minimum one anchoring group. Light (photons) absorption in the visible solar spectrum part is attributed to a metal to ligand charge transfer (MLCT) phenomenon. The main metal ion is, consequently, an essential part of the general features of the complexes. Ancillary ligands, characteristically bipyridines or terpyridines, is able to be modified by diverse substituents (alkyl, aryl, heterocycle, etc.) to alter its electrochemical and photo-physical outcomes and accordingly advance the photodetector overall efficiency. Anchoring groups are engaged in order to establish a link between the metal oxide and the sensitizer and, subsequently, enable the excited electron injection into the CB of the metal oxide. One can adapt any part of the complex to change the MLCT's energy levels and to further optimize the injection of electron as well as dye regeneration process.

Among the metal complexes, Ru complexes such as N3, N749 and N719 (Ardo & Meyer, 2009) have demonstrated an incomparable absorption behavior: a wide absorption wavelength spectrum, sufficient ground and excited state energy levels, comparatively extended excited-state period, and upright electro-chemical constancy. N719 which is driven from N3 dye exhibited an improved performance of the photovoltaic device. In the present thesis, N719 is used to serve as the light absorber for the fabricated device since N719 is the most efficient sensitizer with the chemical formula of bis(tetrabutylammonium)-*cis*-di(thiocyanato)-*N,N'*-bis(4-carboxylato- 4'-carboxylic acid-2,2'-bipyridine) ruthenium(II).

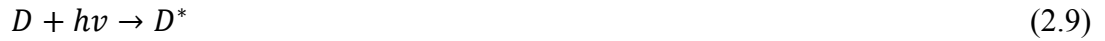
ii. The metal oxide semiconductor: The metal oxide semiconductor is typically a film of targeted material which is deposited on the surface of the FTO substrate. The semiconductor ought to have high surface area to support the monolayer of a sensitizer. The incident light absorption, electron injection phenomenon and collection of electron as well as the process of electron recombination are associated with metal oxide semiconductor which in turn plays very noteworthy part in the photons to measurable electrical amount of energy conversion process in DS photodetector. It is very significant mentioning that Titanium oxide (TiO_2) is certainly one of the best metal oxide used in these devices where it provides the maximum conversion efficiency as compared to other semiconductors. However, there are a number of alternatives, for instance ZnO , Nb_2O_4 , ZrO and SnO_2 are existed. (J. Gong *et al.*, 2012; Lenzmann & Kroon, 2007; Mathew *et al.*, 2014; Omar & Abdullah, 2014). Another key factor to advance the performance of the targeted metal oxide semiconductor is to enhance its surface morphology which directly affects the adsorption of the applied sensitizer. Variety of studies were found focusing on the development of this part of the DS photodetector including the fabrication of various structures, doping with ions, decoration with noble metals, coating with up/down conversion materials and modification with metal oxides (P.-Y. Chen *et al.*, 2013; Dembele *et al.*, 2013; Lijuan Luo *et al.*, 2011; Ye *et al.*, 2011; J. Yu *et al.*, 2013; L. Zhang *et al.*, 2014; Zhu *et al.*, 2017).

In this thesis, $\text{ZnO}/\text{ZnAl}_2\text{O}_4$ -MMO extracted from thermally-treated Zn/Al -LDH which prepared via modified co-precipitation and thermal treatment methods is proposed since this type of MMO has demonstrated a superior behavior in photovoltaic solar cells, sensors and as photocatalytic materials owing their high surface area, good electron injection efficiency, wide band gap and high electrical conductivity (Park *et al.*, 2015; Salih *et al.*, 2018; Tao *et al.*, 2012; L. Zhang *et al.*, 2014).

2.3.1.2 Redox mediator (Electrolyte)

The electrolyte is, typically, a chemical structure in which an electrolytic interaction between the working and the counter electrodes is provided in the fabricated device. In DS photodetector, usually, an organic solvent that consisted of redox couple is used to form the electrolyte. The electrolyte (redox couple) is, typically, Iodide/triiodide (I^-/I_3^-) which in turn is dissolved in, usually not necessarily, acetonitrile, as it was used (O'regan & Grätzel, 1991a). The redox couple, electrolyte, is of great significant for constant functional optoelectronic device whereby it is in charge of charge carriers transfer between the photoanode (working electrode) and photocathode (counter electrode) throughout the period of time that the oxidized dye molecules are regenerated. Hereinafter, the photo-generated electrons are to be injected in the photoanode to complete the circuit (Hamann *et al.*, 2008; Reynal & Palomares, 2011). The redox mediator ought to reinstate the oxidized molecules ground state and only then the sensitizer is formed which is condensed to the photocathode while migrating which in turn is caused by the two electrodes diffusion. The rate of regeneration of oxidized sensitizer molecules to its initial state at reachable concentrations ought to happen as fast as conceivable due to possible inclination to physical degradation.

The redox mediator, for instance I^-/I_3^- , is consisted of two electrons. In a photovoltaic optoelectronic device that involve the photo-current generation, Equation 2.9 to Equation 2.13 represent the electron transportation which is based on the redox couple (Daeneke *et al.*, 2011). In particular, electron transportation between D^+ and I^- is presented in Equation 2.11. Due to energy reasons, it is mostly unlikely that an iodine radical (I^\bullet) to be freed from the iodide (Hagfeldt *et al.*, 2010). Meanwhile, the regeneration “driving force” of the sensitizer species can be evaluated through the formal I_2^-/I^- and D^+/D reduction potential differences (Hagfeldt *et al.*, 2010), where the value of $E^0(I_2^-/I^-)$ in acetonitrile was estimated to be +1.23 V vs NHE.



Diiodide radicals ($I_2^{\bullet -}$) is designed on or after the reaction among oxidized sensitizer species and iodide (Boschloo & Hagfeldt, 2009; Hagfeldt *et al.*, 2010). In Equation 2.11, complex ($D - I$) is designed only when the oxidized sensitizer (D^+) is condensed via the iodide (I^-), once an electron is injected from the excited sensitizer species (D^*) as expressed in Equation 2.9. Herein, the second iodide ion approaches in, where complex ($D - I$) disconnects from the sensitizer in the initial ground level D and $I_2^{\bullet -}$. Hereinafter, as expressed in Equation 2.12, iodide and triiodide are designed as a result of the reaction of two diiodide radicals (Boschloo & Hagfeldt, 2009; Hagfeldt *et al.*, 2010).

It must be mentioned that by far, a number of electrolytes and redox couples (mediators) was proposed in various types, such as small organic molecules (Krüger *et al.*, 2001), gel (P. Wang *et al.*, 2003), solid inorganic materials (Meng *et al.*, 2003), plastic crystal system (P. Wang, Dai, *et al.*, 2004), hole conducting organic polymers (Saito *et al.*, 2004), ionic liquid (P. Wang, Zakeeruddin, *et al.*, 2004) and solid polymer (Kang *et al.*, 2005). However, nowadays, I^-/I_3^- redox couple (electrolyte) in combination with ruthenium (Ru) based dyes is by far demonstrated the best outcomes in term of the output photo-current.

2.3.1.3 Photo cathode

The photocathode, counter electrode, is employed in the device for the sake of electrolyte regeneration. An electrolyte that is oxidized scatters towards the

photocathode where the oxidized electrolyte receives an electron that is donated by the external circuit. In order to speed up the reduction reaction, a catalyst is necessary for this process. Platinum (Pt) is considered, by far, preferable catalyst due to good catalytic activity, sufficient current density as well as transparency. The counter electrode, nanoscale platinum, has demonstrated long term constancy and very high performance. Low loading of platinum as a counter electrode is required for these electrodes demolition (Papageorgiou, 2004; D. Wang *et al.*, 2017). Therefore, the Pt counter electrode is typically transparent and exhibits sufficiently low resistance of charge transfer ($< 1 \Omega \text{ cm}^2$).

The Pt photocathode's performance depends significantly on deposition technique on an FTO glass substrate. Many deposition techniques have been proposed, for instance thermal decomposition of hexachloroplatinic salt in isopropanol (Papageorgiou *et al.*, 1997), electrodeposition (Tsekouras *et al.*, 2008), sputtering which was used in this thesis (X. Fang *et al.*, 2004), vapor deposition and screen printing (Khelashvili *et al.*, 2006). It has been found that the activity of the Pt catalyst decreases with time in the presence of iodide/tri-iodide redox couple (Syrrokostas *et al.*, 2012).

The Key factors of a well performance counter electrode are determined as follow:

- The photocathode must have sufficient current density exchange rate. Therefore, transfer and sheet resistance are required in order to kinetically make the photocathode easy as a passage when electrons transfer and subsequently reduce the oxidized sensitizer species.
- No chemical reaction is required at the photocathode surface (dissolution in I^-/I_3^- electrolyte).
- A reflective photocathode is significant especially when an optoelectronic solid-state device is illuminated from the photo-anode side.

- In order to obtain a reduction in the redox couple through creating driving force, the photocathode should be negatively charged (Papageorgiou, 2004; D. Wang *et al.*, 2017).

2.3.1.4 Conductive glass substrate

During the fabrication of DS photodetector, a conductive material ought to be used in order to make the photocathode and the photoanode lay on, by which the holes and electrons are easily collected and subsequently move with no pronounced losses. In accordance with the DS photodetector fabrication in this study, the conductive materials which is coated on the surface of substrate ought to have certain features such as heat stability, neither absorb nor reflect or scatter visible light and sufficiently rigid.

Generally, fluorine tin oxide (FTO, $\text{SnO}_2:\text{F}$) and indium tin oxide (ITO, $\text{In}_2\text{O}_3:\text{Sn}$) are commonly employed in DS optoelectronic devices as a conductive glass substrate. FTO and ITO conductive glass substrates are consisted of soda lime which is coated using both fluorine tin oxide and indium tin oxide separately, respectively. ITO glass substrate has a sheet resistance of $18 \Omega / \text{cm}^2$ and transmittance higher than 80%. On the contrary, FTO glass substrate exhibited sheet resistance of $8.5 \Omega / \text{cm}^2$ and transmittance in the visible light region of, approximately, 75% (J. Gong *et al.*, 2012). It is essential to be noticed that sintering a single layer of glass substrate (ITO or FTO) at 300 °C and beyond, their sheet resistance increased and conversely the electrical conductivity decline which in turn lead to energy losses and subsequently lower device efficiency. An increment in the sheet resistance of the glass substrate is mainly due to a decrease in the amount of charge carries. According to a recent study, which was conducted by Sima *et al.* 2010, a comparison between ITO and FTO was performed photovoltaic performance. Both photoanodes based on ITO and FTO were thermally treated at 300 °C for a period of 2 h in air. It was found that ITO sheet resistance augmented from 18

Ω/cm^2 to $52 \Omega/\text{cm}^2$, in the meanwhile, the sheet resistance of FTO glass substrate remained unchanged. Thus, the current study employed FTO as the photo-electrode glass substrate (Sima *et al.*, 2010).

2.3.1.5 Device packing (Sealing)

One of the foremost significant challenges of DS photodetector fabrication technology is its sealing, by which the stability and extended period performance are determined. Leakages or losses as well as the evaporation of electrolytes are prevented by sealing materials. The ambient intrusion of water and/or oxygen possibly leads photo oxidation phenomenon. To start with, photo-chemical and chemical stability of the sealing materials against both electrolyte and solvent components are of great importance. Furthermore, the sealing materials should be well anchored with the FTO or ITO glass substrate. There are variety of sealing materials types such as epoxy and silicon. While, another widely used type, which is employed in the current work, is meltonix (thermoplastic film, Solaronix- DuPont surlyn). Nevertheless, oxygen-tight glues are commonly used as external sealing for extended period of constancy such as epoxy resin.

2.3.2 Electron transport process in dye-sensitized photodetector

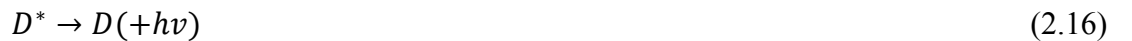
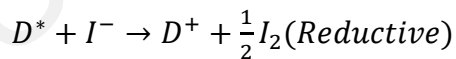
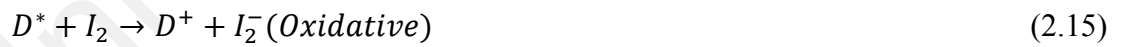
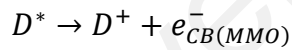
The DS photodetector operating mechanism is constructed on the energy, transfer of electrons as well as charge transportation phenomena kinetic competition in which each and every reaction is expressed kinetically by the rate constant of the reaction. Therefore, the key-factor for high photo-responsive behavior depends on the ratio of time scale between an advantageous and uncomplimentary electron transfer forces. As such, these types of reaction are separated into two main groups: an anticipated advancing reaction which includes the photo-excitation, injection of electron in the CB of metal oxide semiconductor, regeneration of sensitizer species and transportation of

electron-hole pairs via the electrolyte (redox potential); the undesirable disadvantageous reaction which in turn includes photo-excited relaxation of the sensitizer species, recombination between electrons in the metal oxide layer and redox potential in the electrolyte and another type of recombination between sensitizer species and free electrons. A schematic representation is illustrated in Figure 2.7 (a and b) by which relevant photo-physical process and electron transportation phenomenon are demonstrated. Figure 2.7 (a) also shows the time-scale for individual processes. As depicted in Figure 2.7, the advantageous reaction profit from the separation of charge and thus contributes in the conversion of energy (blue arrows), however, the disadvantageous reaction (black arrows) signifies the recombination of charge and thus considered as a limitation of the device efficiency (L. Yang, 2014). These reactions are discussed thoroughly in the following sections:

i. Photo-excitation: a photon is absorbed by the sensitizer species; this phenomenon in turn causes an electron excitation from the high occupied molecular orbitals (HOMO) of the sensitizer as expressed in Equation 2.14. The HOMO should be high as compared to the CB level of the semiconductor layer. The excited electron is then transferred to the low unoccupied molecular orbital (LUMO) of the sensitizer as expressed in Equation 2.14. The energy of the excited photon must be higher than or equivalent to the band gap of the sensitizer (HOMO-LUMO gap). Therefore, the separation of charge is obtained. Equation 2.15 shows an excited sensitizer which contributes with electron to be injected into the CB of the metal oxide semiconductor. Equation 2.16, on the contrary, describes an electron that is relaxed back to the ground state of the sensitizer through non-irradiative or irradiative decays.

ii. Electron injection: the procedure of electron transportation from the photo-excited state of sensitizer into the CB of the metal oxide semiconductor happens within

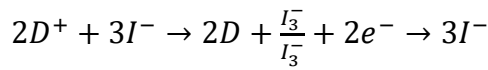
femto-second to pico-second with respect to the timescale. However, the photo-excited state of electron prior to relaxation happens within nano-second life-time (Dualeh, 2014; Listorti *et al.*, 2011; Omar & Abdullah, 2014). Therefore, the sensitizer excited state may be quenched through the electrolyte species (redox couple). As described in Equation 2.15, the redox couple iodine may quench the excited sensitizer via either oxidative (D^+) or reductive (D^-) generation (Listorti *et al.*, 2011). The charge separation procedure might decrease as a result of the oxidative process, whilst photo-generation charge efficiency can increase if the sensitizer anion inject an electron onto the CB of the metal oxide semiconductor, during reductive process (Listorti *et al.*, 2011). Thus, the reaction rate of electron transportation (ET) constant of injected electron (K_{inj}) is then more than one magnitude order higher than that of relaxation of sensitizer (K_{rel}). To explain, Equation 2.17 expresses the process of a satisfactory electron injection efficiency (η_{inj}) in which the electron that is injected in the CB of metal oxide semiconductor (e_{CB}^-) is measured only subsequent to the photo-excitation.



$$\eta_{inj} = \frac{K_{inj}}{K_{inj} + K_{rel}} \quad (2.17)$$

iii. Regeneration of sensitizer: the sensitizer (in its oxidation state) regeneration is obtained due to the electron transportation from the electrolyte (redox potential) or else

by the transport of hole to the photocathode subsequent to separation of charge as well as injection of electron as expressed in Equation 2.18. Conversely, the recombination of free electrons in CB of metal oxide semiconductor with the sensitizer species (in its oxidized state) is expressed in Equation 2.19. Equation 2.20 describes the recombination of free electrons in the CB with the holes that are located on the mediator. Generally, a sufficient regeneration is obtained if the constant rate of sensitizer regeneration (η_{reg}) is high as compared to recombination to species of hole (K_{rec}), in which Equation 2.21 is demonstrated is alike way to (η_{inj}).



$$\eta_{reg} = \frac{K_{reg}}{K_{reg} + K_{rec}} \quad (2.21)$$

vi. Charge transport: the electrons (e_{CB}^-), which are injected in the CB of metal oxide semiconductor, are being shifted through the metal oxide semiconductor layer by controlled procedure diffusion instead of the drift current. In the fabricated device of this study, liquid state of electrolyte, both ways of free electron recombination to either the sensitizer (oxidation state) species, in which the active species of the redox are designed, following regeneration of sensitizer to the photocathode (Pt electrode) as it is decreased, or the carrier of hole of the mediators hole transport challenges with the transport of electron. Continuously, the "constant rate" of diffusion (K_{trans}) ought to be higher than that of recombination of electron (K_{rec}) through a semiconductor layer,

whereas otherwise causes photo-generated charge loss (Equation 2.22). Therefore, the kinetic challenge between the loss process and initial charge of photo-induced separation controls the efficiency of the fabricated device (photo-to-current conversion) (Hagfeldt *et al.*, 2010; L. Yang, 2014).

$$\eta_{cc} = \frac{K_{trans}}{K_{trans} + K_{rec}} \quad (2.22)$$

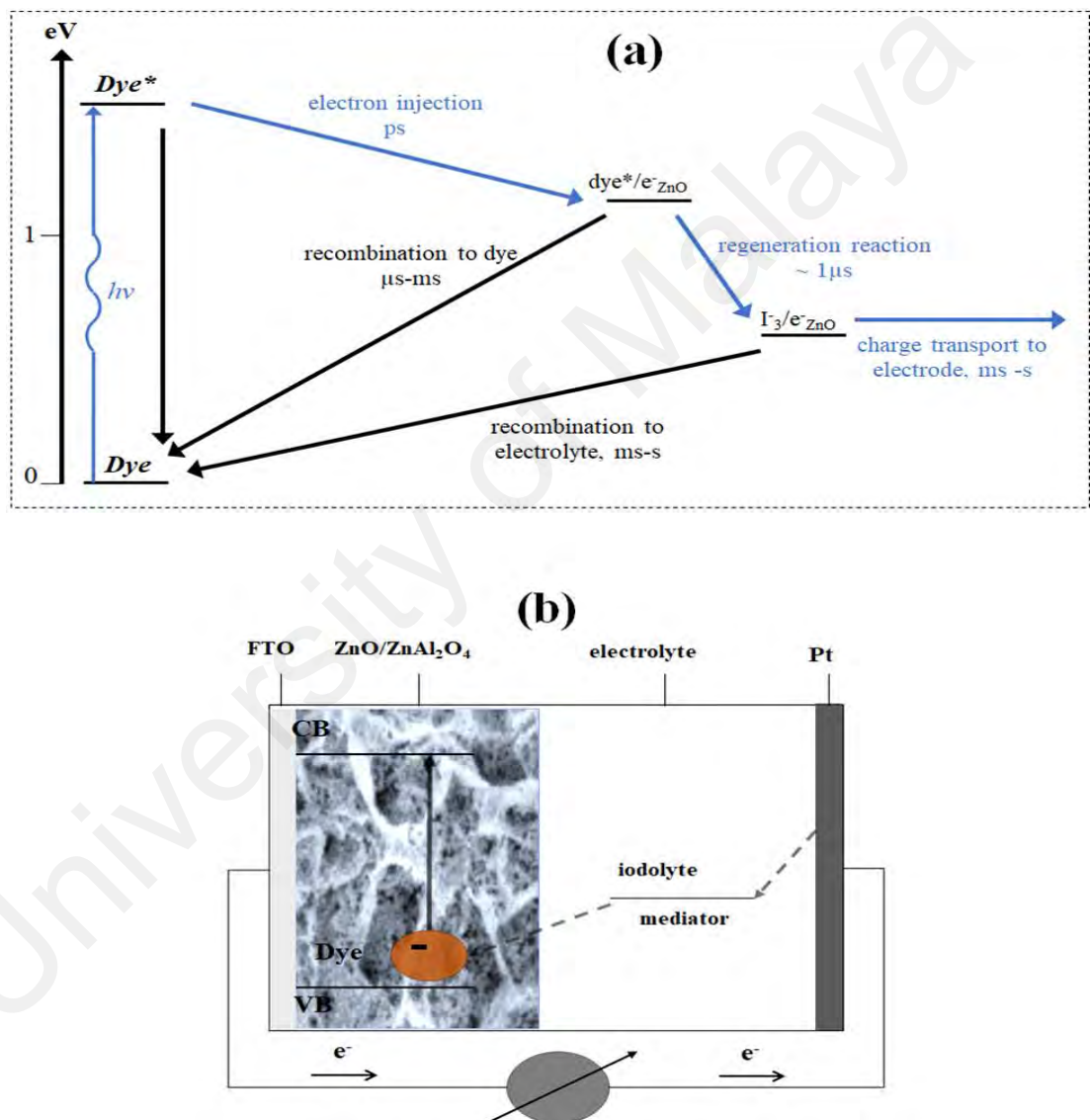


Figure 2.7: (a) schematic representation of the DS photodetector kinetics (Omar & Abdullah, 2014) and (b) operation principle and scheme of the energy levels of a solid-state device.

2.4 Summary

From the comprehensive literature analysis, LDHs have shown a number of promising features for wide-range of applications including photo-catalyst, micro-container, drug delivery, photo-response and dye-sensitized solar cells. Thermal treatment of LDH leads to a collapse in the LDH 2D layered structure and then formation of MMOs which are composed of metal oxide and spinel phases. Recently, MMOs have shown great interest among research society as anode materials in lithium ion batteries and photo-catalyst, especially in the visible light region, due their unique mesoporous structure and high surface area. In optoelectronic applications, MMOs are well-thought-out as promising electrode due to their wide energy band gap, similar electron injection efficiency and photo-response which are similar to ZnO and TiO₂, the most frequently used semiconductors for optoelectronic applications. With well-established synthesis approaches such as thermal treatment of LDH, dispersed bimetal oxide, finally, can be acquired due to cations uniform distribution and upright arrangement. Moreover, a number of studies aiming at the enhancement of the optoelectronic devices' photo-responsive behavior and overcome the "visible blind" issue have been of great need, wavelength ranging from 400 to 780 nm in particular. Subsequently, many approaches have been developed. These strategies demand careful preparation methods and moreover complicated equipment. The sensitization method, which is employed in this study, offers an alternative pathway to broaden the spectral photo-response. The fascinating breakthrough of this method is the use of organic dye as visible light sensitizer attended with wide band-gap semiconductor such as ZnO/ZnAl₂O₄-MMO as functional anode material. Taking all these into account, this study was designed to address the ZnO/ZnAl₂O₄-MMO as the sensing film for dye-sensitized photodetector.

CHAPTER 3: MATERIALS, EXPERIMENTAL METHODS AND PROCEDURES

The current chapter describes the experimental methodology, materials, instruments and characterization techniques involved to conduct this research. Section 3.1 introduces the chemicals used for sample preparations. Next, Sections 3.2 thoroughly describes detail procedures used in Zn/Al-LDH and ZnO/ZnAl₂O₄-MMO anode material samples preparation and DS photodetector devices fabrication. Finally, throughout Section 3.3 a list of the equipment used for microstructural, morphological, texture, optical and photo-response performance characterizations used in the study is demonstrated. Figure 3.1 demonstrates the methodology procedure which was used in this thesis.

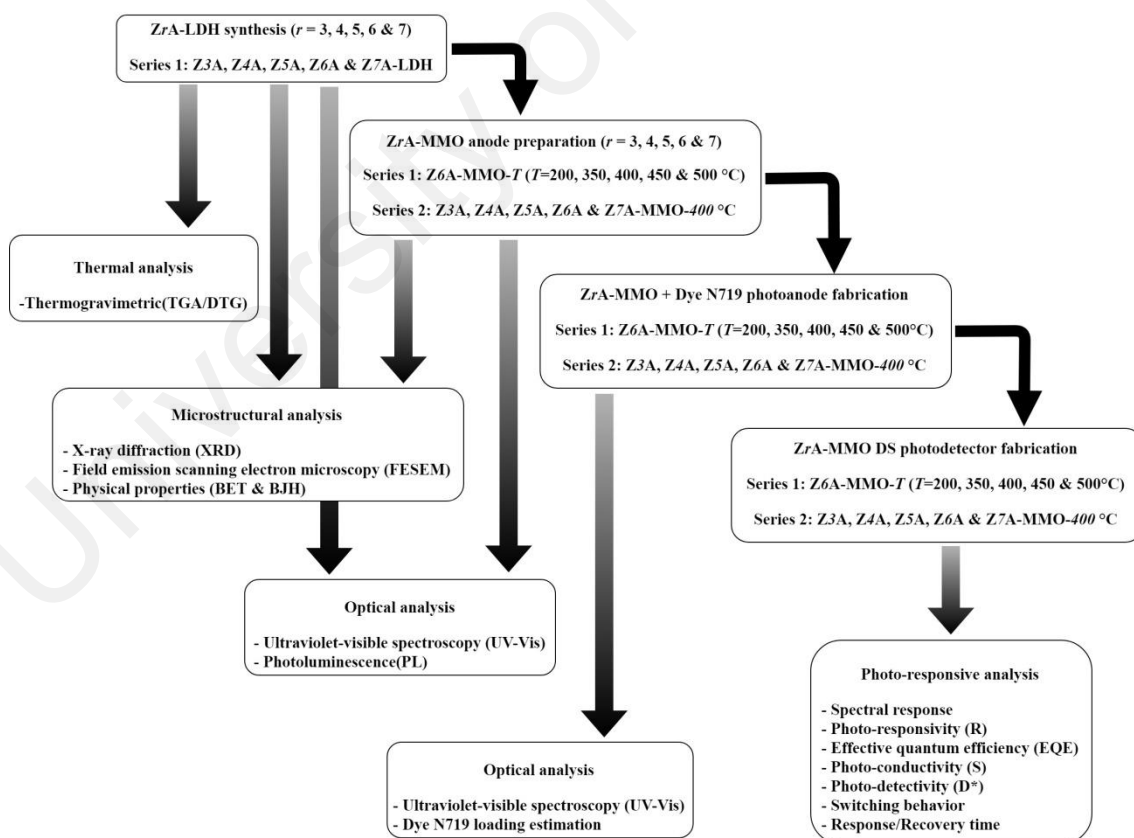


Figure 3.1: Methodology flowchart.

3.1 Methodology

3.1.1 Substrate cleaning protocol

The cleaning process is crucial in improving the wettability and hydrophilicity of the substrate surface for homogenous materials deposition and nanostructures fabrication. FTO (Solaronix) substrates were immersed in a beaker filled with soapy water and cleaned via ultra-sonication for 20 minutes. Then, they were further sonicated with acetone, deionized water and ethanol for 20 minutes each, respectively, aiming to completely eliminate whichever undesirable contaminations on FTO substrates. After the sonication process, the FTO substrates were dried using nitrogen (N₂) gas blow.

3.1.2 Zn/Al-LDH preparation

Zn/Al-LDH phase structure was synthesised in the function of the molar ratio between Zn²⁺ and Al³⁺ (r), where r is 3, 4, 5, 6, and 7. In a typical procedure, a precursor solution that consisted of 200 mL of aqueous solution of deionized water (DI), x M of Zn(NO₃)₂·6H₂O (Aldrich, 98.1%) and y M of Al(NO₃)₃·9H₂O (Merck Co., 99.4%) was prepared under the stirring rate of 700 rpm under ambient environment. Importantly, the growth solution pH was preserved at 7 throughout the experiment (under the existence of 1.5 M of NaOH dropwise addition, Aldrich, 99%) for the preservation of a homogeneous crystal growth system (Salih *et al.*, 2018). The final white slurry Zn/Al-LDH precipitate was subsequently kept in regular oven at 65 °C for 12 h to grow a homogeneous mesoporous structure. Subsequently, the solution was washed thoroughly using ethanol and centrifuged. Only then it was dried at 80 °C for 24 h. In order to obtain a satisfactory nanocomposite (LDHs) dispenser, the powder was grinded using a silica mortar. Herein after, the obtained pristine LDHs are denoted as ZrA-LDH, whereby r represents the metallic molar ratio between Zn²⁺ and Al³⁺. The schematic illustration for the synthesis procedure of Zn/Al-LDH is shown in Figure 3.2. The amount of raw materials (Zn⁺², Al⁺³, NaOH), which were used during the synthesis

procedure, were calculated according to equation 3.1. A detailed calculation is to be found in appendix B.

$$Wt = \text{Molarity} \times \text{Volume (L)} \times \text{Mol. Wt} \left(\frac{\text{g}}{\text{mol}}\right) \times \frac{100}{\text{purity}} \quad (3.1)$$

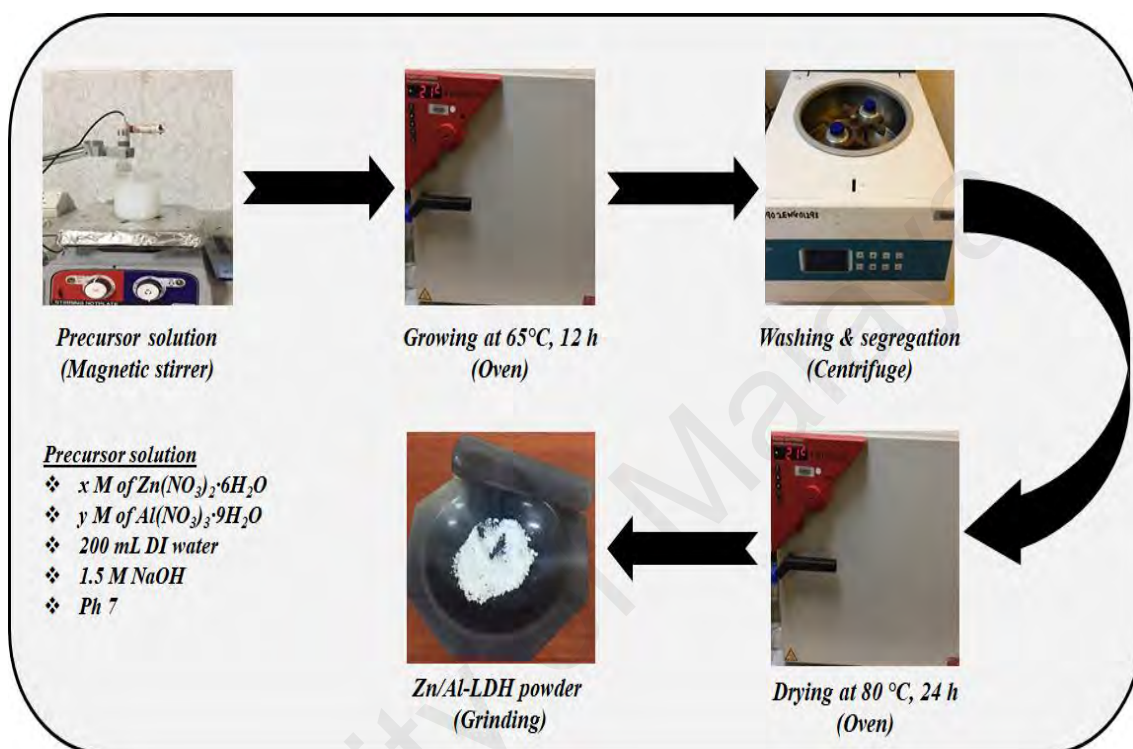


Figure 3.2: Schematic diagram of Zn/Al-LDH nanoparticles synthesis procedure.

3.1.3 ZnO/ZnAl₂O₄-MMO anode materials preparation and phase Transformation

Mesoporous ZnO/ZnAl₂O₄-MMO anode continuous films using Zn/Al-LDH as the precursor were prepared via doctor blade method and thermal treatment. A sufficient amount of the prepared Zn/Al-LDH powder (0.5 g) was subsequently mixed with (0.05 g) PEG 400 until a paste was formed. Paste viscosity was controlled by adding a few drops of ethanol to the paste. The resulting mixture was subjected to a deposition process intended for a 1 cm² film layer formation on the FTO substrate surface via doctor blade method. Subsequently, the LDH to MMO phase transformation was performed through a thermal treatment technique at various thermal treatment

temperatures for 60 minutes at 5 °C/min heating rate for all the prepared anode films (Figure 3.3). Herein after, the fabricated MMO samples were donated as Z_rA -MMO-400 whereby $r = 3, 4, 5, 6$ and 7 , while 400 represents the thermal treatment temperature. Furthermore, Z_6A -LDH sample was subjected to a variety of thermal temperatures ranging from 200 to 500 °C and thus donated as Z_6A -MMO- T , where $T = 200, 300, 350, 400, 450$ and 500 . Figure 3.3 illustrates a schematic demonstration for the anode films preparation together with labeled samples and thermal treatment stages.

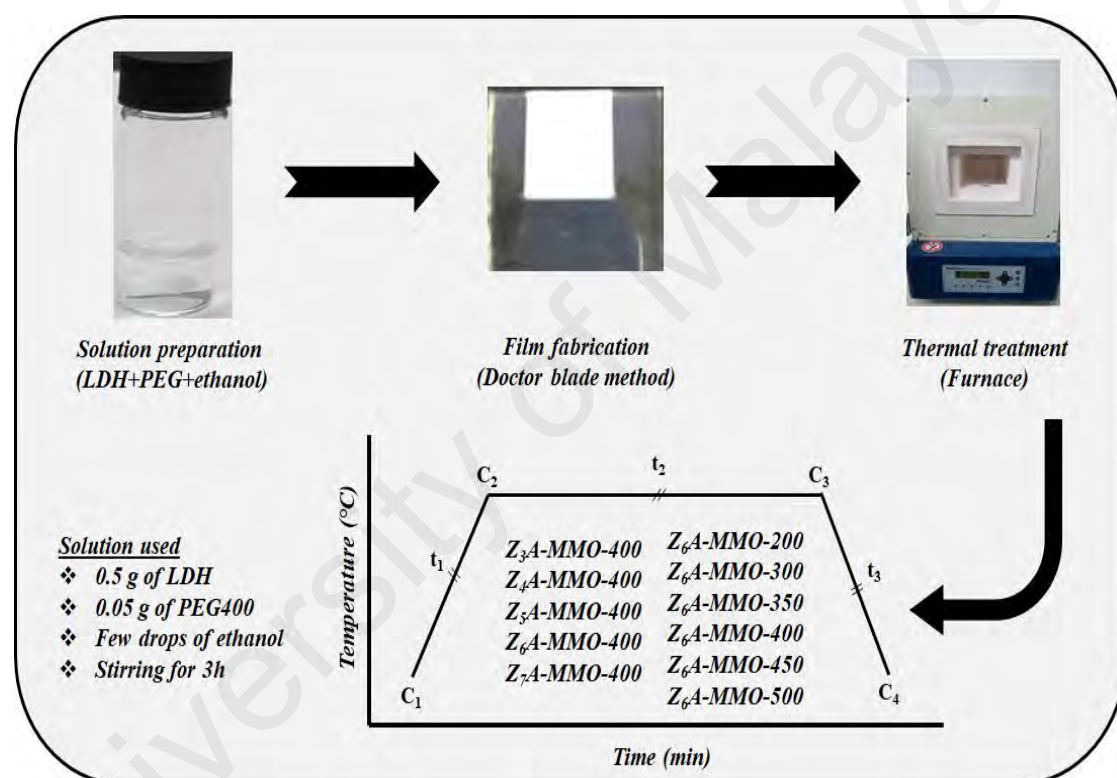


Figure 3.3: Schematic diagram of MMO anode materials preparation and thermal treatment process.

3.1.4 Dye-sensitized photodetector fabrication

The MMO anode films were dipped in 5 mM dye solution that consisted of Ruthenizer (N719, Solaronix) for 3 h at room temperature (RT), subsequently; in order to remove the undesired residuals; the photoanode film was rinsed with ethanol. Figure 3.4 demonstrates the schematic structure of the fabricated DS photodetector. The DS photodetector is composed of two parts. One part is a counter electrode consisting of 50

nm-thick Pt electrode prepared using FTO-coated glass substrate serving as cathode via sputtering technique. The other part is a mesoporous ZnO/ZnAl₂O₄-MMO layer prepared on the FTO-coated glass substrate. Subsequently, a thermoplastic film (Solaronix, 100 μm) was sandwiched between the two substrates. The thermoplastic film served as a brace that separates the two contact surfaces. Electrolyte Iodolyte Z30 redox couple:iodide/triiodide (Solaronix) was later injected into the fabricated device by capillarity. Lastly, a conducting wire was connected to the corresponding electrode for measurement.

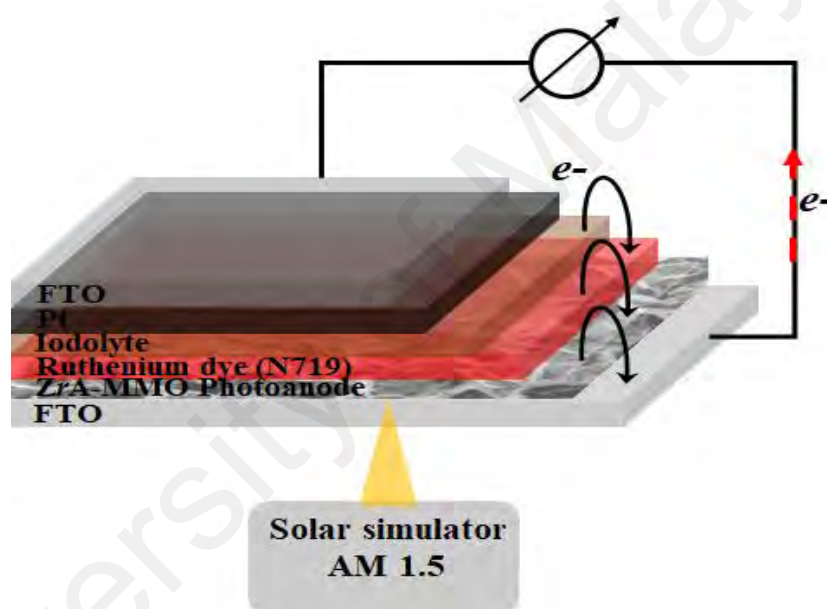


Figure 3.4: Schematic diagram of the DS photodetector.

3.2 Characterization techniques

Thermal properties were carried out using Thermogravimetric analysis (TGA/DTG). Among the characterization equipment used for the microstructural properties analysis of the prepared samples are X-ray diffractometer (XRD), field emission scanning electron microscopy (FESEM) and the surface area and pore volume (BET & BJH) of the prepared MMO anode materials were analysed using a nitrogen gas (N₂) adsorption/desorption technique. The prepared MMO anode film thickness was measured using surface profilometer. Furthermore, the optical properties of the samples

were characterized using ultraviolet-visible-infrared (UV-Vis) and photoluminescence (PL) spectroscopies techniques. Finally, photo-responsive properties of the fabricated DS photodetectors were carried out using Keithley 237 source measure unit.

3.2.1 Thermogravimetric analysis

Thermogravimetric analysis (TGA) is a technique used to measure the loss of mass of a material while changing the temperature over time. The thermal stability of materials can be determined via TGA test. This type of measurement gives important information about thermal decomposition of a prepared material. TGA analyzer contains a precision balance and a sample holder which is located in a furnace (a programmable temperature controller is provided). The temperature increment is typically achieved through a constant rate so as to incur a suitable thermal reaction. The thermal reaction could be performed at many atmospheric conditions such as air, vacuum or even installed gas. TGA analyzer weighs the sample mass as the material under test is heated with temperature increment, up to 2000 °C. As the applied temperature rise, many components of the material under test are subject to be decomposed, continuously the mass weight percentage is measured. To calculate the inflection points, DTG curve is determined from TGA result which is considered very useful for further insight analysis and interpretations of the TGA curve.

In the present study, the ZrA-LDH samples were tested using Mettler Toledo TGA/SBTA851 analyzer with 5 °C/min heating rate in air initializing at (RT) room temperature to 500 °C until full decomposition of the prepared samples was acquired. TGA/DTG analysis is employed in this study to demonstrate an extensive illustration of the synthesized materials thermal behavior and located the maximum weight loss temperature range.

3.2.2 X-ray diffraction

The XRD is an essential approach in determining a crystal structure for the materials used in this thesis. XRD could also deliver evidence of crystalline phase, purity as well as plane orientation of a material (Cullity & Stock, 2001). When a monochromatic beam of X-ray hits the atoms in the crystal lattice of the sample, each atom acts as a source of dispersion whereas crystals act as a series of parallel planar reflection. When dispersions are symmetry to the distance between atomic planes (d), the spherical wave will be parallel. In such cases, part of the incident X-ray beam is deflected by the angle 2θ , producing a reflection on the diffraction pattern, as shown in the Bragg's equation:

$$n\lambda = 2d \sin\theta \quad (3.2)$$

where n represents the order of diffraction (usually $n = 1$), λ is the wavelength of X-ray using Cu-K α source of radiation ($\lambda = 1.5418 \text{ \AA}$) and d is considered the distance between the plane shared by Miller indices h , k and l .

herein, D represents the crystal size, λ is the wavelength ($=1.5418 \text{ \AA}$) of X-ray employed, while β is broadening of diffraction line which is measured at half of its highest intensity (in radians unit) and θ is the diffraction angle used for measurement.

In the current study, ZrA-LDH, ZrA-MMO-400 and Z6A-MMO-T samples were tested using Bruker AXS D8 Advance model diffractometer with Cu-K α rays ($\lambda = 1.54060\text{\AA}$). The scan angle ranges between $4 - 70^\circ$ and XRD data were collected on Philips X'Pert ProMPD.

3.2.3 Field emission scanning electron microscopy

The surface morphology of a nanostructured layered film can be investigated using FESEM. In this technique, electrons beam is used to analyze and generate the microstructure images of the specimen surface. The quality electron beam is controlled

via the changes of accelerating voltage in the range of 1.20kV. Principally, electrons are emitted from the hot filament tungsten wire source and accelerated in the high energy electric field. The primary electron beams are focused and refracted by a series of electromagnetic lenses (such as objective or condensed lens) and apertures in a scale of a few nanometers toward the sample. Meanwhile, sensors are used to trap the secondary electrons and produce an electronic signal. The secondary electrons are crucial in showing the morphology and topography of the samples, in which their angle and velocity are closely associated with the surface structure of a material under test. In the meanwhile, the electronic signal is then transformed into an image to be viewed and analyzed later.

In the current study, the FESEM is employed to develop a deep understanding of the prepared materials morphological analysis aiming to estimate the best porosity for higher dye loading. All the prepared samples with mesoporous films surface morphology (*ZrA-LDH*, *ZrA-MMO-400* and *Z6A-MMO-T*) were characterized by field emission scanning electron microscopy (FESEM, Hitachi-SU8030) at accelerating voltage of 1.20kV.

3.2.4 Surface area and pore size analysis

Brunauer-Emmett-Teller (BET) analysis provides precise determination of the degree of adsorption by a material on a solid surface. It also serves as the fundamental for crucial analysis technique for specific surface area assessment using multilayers of nitrogen (N) adsorption evaluated as a relative pressure function. The BET technique covers outer and pore area determination in order to evaluate the overall specific surface area (m^2/g) which helps understanding very essential evidence in revising the properties of the porosity of the surface as well as the particle size and their effect in a number of applications. It is crucial in this thesis to develop deep understanding of the surface area

for materials used since it directly guides to better understanding the dye adsorption on the photoanode solid surface. Barrett-Joyner-Halenda (BJH) analysis mainly employed in order to evaluate the pore size as well as specific pore volume by employing two techniques, namely, adsorption and desorption. The mentioned procedure analyzes the distribution of pore size which is independent of outer area because of the particle size of the material. In the present thesis, the specific surface area, pore size and pore volume of the samples were analysed through a nitrogen gas (N₂) adsorption/desorption approach by employing Micromeritics ASAP 2000 instrument (Norcross, GA). This technique is used to support the FESEM analysis by which the amount of dye loaded on the MMO materials is predicted. Prior to measurements, a degassing process was performed overnight at 200 °C, while the nitrogen adsorption was measured at 77 K. The samples which were analysed are ZrA-MMO-400, Z6A-MMO-T and Z6A-LDH.

3.2.5 Surface profilometer

Surface profilometer (KLA Tencor, model: P-6 stylus) was employed to measure the effective thickness of fabricated layers. In the profilometer used, a method of contact has been applied by which stylus vertically moves across the film surface and measures its thickness variation. The thickness variation is measured as a position function and scan length and stylus force of 150 mm and 0.3-5.0 mg, respectively, while the altitude (vertical) is 327 µm. Prior to measurements, the film must be prepared by linear scratch, obtained manually, to provide steps trace between the surface of the substrate and the layered film. The stylus tip is to be perpendicularly pulled alongside the linear scratch in which the variation between the levels of the prepared layered film and the substrate is detected. Herein, this technique is used to measure the thickness of the printed MMO layer on the FTO substrate for later use in band gap and photo-conductivity calculations.

3.2.6 Ultraviolet/Visible/Infrared spectroscopy analysis

Generally, the UV-Vis measurements can be conducted in a wide range of light spectrum, including ultraviolet light (UV), visible (Vis) and near infrared (NIR) region. When the light with specific wavelength which is propagated in the sample under test, the material's molecules is interacted with the propagated wave which in turn causes three phenomena namely; absorption, reflection and transmission. These phenomena only obtained if the energy of incident photons was absorbed through electrons which is located in the HOMO level, in which electrons are transmitted to the LUMO level of the respective material under test. In this study, the UV-Vis spectrophotometer used was Pekin Elmer Lambda 750UV/Vis/NIR spectrophotometer with wavelength ranging from 190 to 3300 nm. The spectrophotometer is of two holders; the first one is employed in order to calibrate the baseline while another for the optical analysis of the prepared semiconductor materials. The baseline calibration must be accomplished by engaging two clean FTO glasses in the mentioned holders. Once the baseline calibration is performed, then one of the substrates can be removed while the second remained at the second holder. The intensity of the reference beam (FTO substrate) which is very low with almost no light absorption is defined as I_0 . Meanwhile, the beam intensity of the sample (FTO/MMO or FTO/MMO/N719) is defined as I . All of the measurements were performed within a scan range of wavelengths from 300 to 800 nm. The absorption of the sample can be derived from transmittance ($T = I/I_0$) or absorbance ($A = \log I_0/I$) data. Then, the absorption coefficient of the sample can be deduced from the well-known Lambert-Beer law (H. Li *et al.*, 2013):

$$\alpha = 2.303 A/d \quad (3.4)$$

where d is the path length and A is the absorbance determined from UV-vis. After that, the Tauc relation is used to extract the optical band gap (E_g) of the sample based on

its mathematical relation with absorption coefficient, as represented in the equation below (H. Li *et al.*, 2013):

$$(\alpha h\nu)^2 = A(h\nu - E_g) \quad (3.5)$$

To determine the optical band gap energy (E_g) of the sample, $(\alpha h\nu)^2$ was plotted as a function of photon energy ($h\nu$) and the linear portion of the curve was extrapolated to obtain the value of E_g . The main aim of both UV-Vis absorbance measurement and band gap calculation is to develop an understanding of the energy levels of the used materials which in turn is used as a support for the fabricated DS photodetector behavior analysis.

3.2.7 Photoluminescence spectroscopy

PL spectroscopy is considered as a non-destructive characterization method for semiconductors because sample under test is to be excited optically in the measurements without electrical contact required. In PL characterization, the intensity of the PL signal provides information on the quality of surface and interface (Gfroerer, 2000). In addition, the PL spectrum also provides information on energy transition that can be used to determine the electronic energy levels of the sample, whereas the PL intensity indicates the relative rate of radiative and non-radiative recombination in the sample (Z. Li *et al.*, 2008). When the incident light is illuminated onto the surface of the sample, electrons which gained sufficient energy will be excited from the VB or HOMO to the CB or LUMO. Eventually, the excited electrons will become relaxed and decay back to the ground state in VB. If radiative relaxation occurs, the emitted light radiation is known as the PL. However, when excitations (pairs of electrons and holes) recombine in the crystal or at the site of impurities the recombination will result in the non-radiative emission.

In this study, Perkin-Elmer LS-50B luminescence spectrophotometer was employed in order to perform PL measurements of the prepared *ZrA-MMO-400*, *Z6A-MMO-T* and *Z6A-LDH* samples. The PL analysis is employed in this thesis as an indicator of the crystal quality of the deposited MMO materials which in turn provides a rough estimation of the fabricated DS photodetector photo-responsive performance. A Xenon light source with 50 Hz flashes was used as the excitation source and the light wavelength was set at 325 nm. The excitation and emission slit width was set at 2.5 which is important to reduce the noise level. The emitted photons will be detected by the photon detector. The recorded PL spectra were analyzed using Origin Pro 8.5 software.

3.2.8 DS photodetector performance measurements

The Photocurrent switching characterization is a standard and essential technique to measure the photo-responsive performance of a photodetector. The maximum photocurrent generated by the photodetector can be determined from its current response when the forward bias voltage is applied and under zero bias condition as well. Figure 3.5 shows the typical current response measurements setup of the DS photodetector. The current response of the photodetector was divided by its active area (1 cm^2) to obtain the response of current density (J) against applied bias voltage and various illumination power. The key sensing parameters calculation of the photodetector is demonstrated in section 2.2.2, and thus it is unnecessary re-discuss them once again in the current chapter. In present thesis, a Keithley 237 source measure unit was used to obtain the photo switching characteristics of the fabricated DS photodetector devices (*ZrA-MMO-400* and *Z6A-MMO-T*) under dark and illuminated conditions (0, 25, 50, 75 and 100 mW cm^{-2}) from a solar simulator equipped with AM 1.5G filter at 0 and 0.5 biasing. The photocurrent data for all of the fabricated devices was recorded by LabView software during measurements.

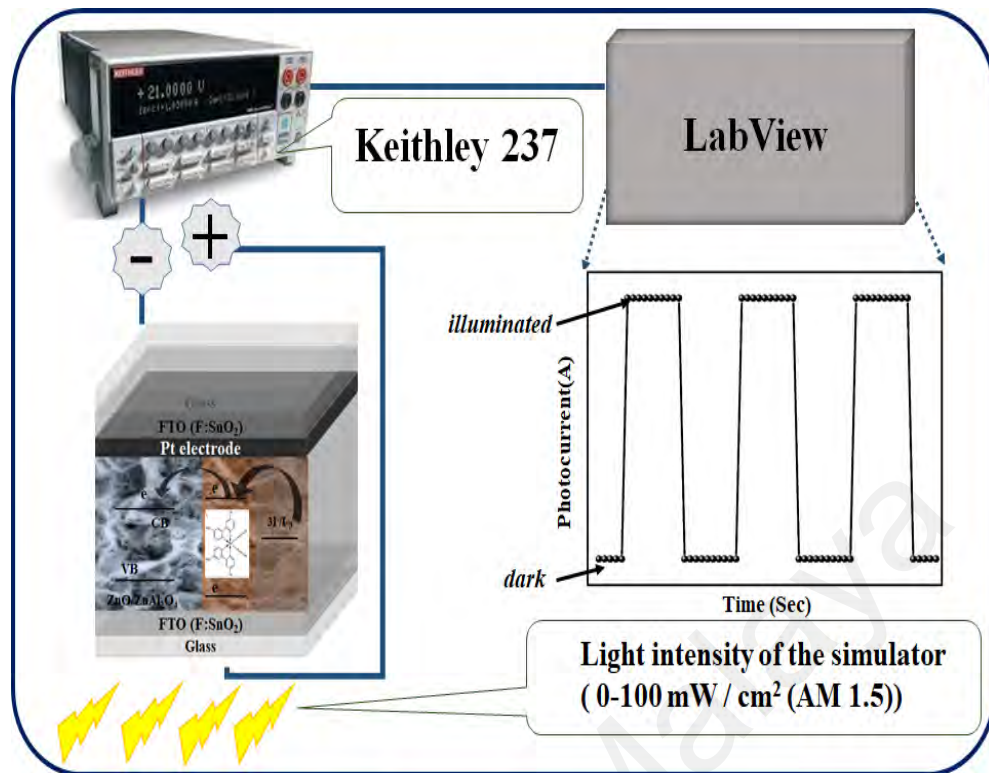


Figure 3.5: Photocurrent measurements setup of the fabricated DS photodetector.

CHAPTER 4: RESULTS AND DISCUSSION

The main goal of the current chapter is to demonstrate an extensive investigation of the thermal, structural, morphological and optical properties of the prepared materials as well as the performance analysis of the fabricated dye-sensitized photodetectors. This chapter is divided into four main sections. The thermal behavior of pristine *ZrA-LDH* is presented in Section 4.1. In the meanwhile, in Section 4.2, a detail microstructural analysis of the prepared materials (*ZrA-LDH*, *Z6A-MMO-T* and *ZrA-MMO-400*) is presented at different thermal treatment temperature and molar ratios. Furthermore, Section 4.3 analytically discusses the effect of thermal treatment temperature and molar ratio on *Z6A-MMO-T* and *ZrA-MMO-400* anode materials optical properties using two techniques, namely, UV-Vis and PL spectroscopies. Additionally, pristine *Z6A-LDH* is also presented as a comparison point for the aforementioned two techniques. Finally, throughout Section 4.4, the spectral response, illumination power dependence and key sensing parameters and photo-switching behavior of the fabricated *Z6A-MMO-T* and *ZrA-MMO-400* dye-sensitized photodetectors are illustrated and discussed systematically.

4.1 Thermal properties analysis

The stability of the synthesized *ZrA*-LDH samples in thermal-controlled condition was analysed using thermogravimetry and differential thermal analysis (TGA-DTG), where *r* signifies the actual molar ratio of Zn^{+2} to Al^{+3} . In this study, only *ZrA*-LDH samples were taken into consideration for thermal analysis. Other samples (*Z6A*-MMO-*T* and *ZrA*-MMO-400) were not studied due to very low weight loss (~1%) after thermal treatment. However, the optimum sample (*Z6A*-MMO-400) is illustrated in appendix C, where only ~1% weight loss was observed. Thermal treatment of LDH caused the collapse of 2D layered structure and the formation of the MMO composed of metal oxide and spinel phases (Cheng *et al.*, 2010b). As depicted in Figure 4.1 and Table 4.1, TGA-DTG curves are shown in Figure 4.1 (a-e) at different molar ratios of Zn^{+2} to Al^{+3} . Generally, TGA curves displayed three-stages weight loss of ~38 wt% degradation behaviour for all *ZrA*-LDH molar ratios (Table 4.1). These stages were named R1, R2 and R3 as shown in Figure 1(f). In the range of R1 (~ 30°C- ~140 °C) weight loss was mainly attributed to water release from the interlayer and surface of the prepared *ZrA*-LDH samples. The second stage (R2) was observed in the range of (~140°C- ~250 °C) which was originated from the *ZrA*-LDH brucite-like layers dehydration. In the meanwhile, R3 (the last stage, 300 °C–550 °C) was related to the recrystallization, nitrate ions decomposition in the interlayer of *ZrA*-LDHs and the existence of ZnAl_2O_4 brucite spinel phase (Chai *et al.*, 2009). The large mass loss phenomenon indicates the crystal reorientation and phase transformation of *ZrA*-LDHs to $\text{ZnO}/\text{ZnAl}_2\text{O}_4$ -MMO after Zn^{2+} incorporation (Cui *et al.*, 2010). Hence the results of the DTG curves (Figure 4.1, a-e and Table 4.1) were found to be in good agreement with the findings by other researchers (Chai *et al.*, 2009; Cui *et al.*, 2010) . In particular, three main peaks located at P1 (~100°C), P2 (~198°C) and P3 (~ 445 °C) were observed in the DTG curves. Similar to these findings, P1 was related to the water

elimination, P2 to the dehydration of interlayer *ZrA*-LDH samples, and P3 to the nitrate ions decomposition and recrystallization. In details, the pronounced small peaks at 157 °C and 155 °C of *Z6A*-LDH and *Z7A*-LDH samples, respectively, are mainly due to the dehydration of *ZrA*-LDHs layers (Chai *et al.*, 2009; Cui *et al.*, 2010). As for low molar ratios (*Z3A*, *Z4A* and *Z5A*-LDHs) the named peaks are not found, in which this phenomenon may be because of an overlap between the water release and dehydration process during the weight loss. These weight loss stages which took place with increasing the temperature are believed to be in relation to the endothermic transformation (Saber & Tagaya, 2009). From DTG peaks and TGA curves (Figure 4.1 a-e), as mentioned above, a collapse in the 2D *ZrA*-LDHs layered structure is caused by thermal treatment with MMO phases formation. This hypothesis clearly suggests that a favorable thermal treatment temperature of prepared LDHs is between 400 °C and 450 °C, and thus the present study employed an in-depth analysis of fabricated dye-sensitized photodetector in the mentioned temperature range.

Table 4.1: TGA/DTG in-depth data of pristine *ZrA*-LDH; where $r = 3, 4, 5, 6$ and 7 .

Sample	T _{range} (°C)	T _{max} (°C)	Weight loss (%)
Z3A-LDH	30-145	100	6.62
	145-375	220	24.35
	375-580	450	6.7
Z4A-LDH	30-138	100	8.29
	138-375	205	23.3
	375-590	460	6.3
Z5A-LDH	30-137	98	8.25
	137-400	195	22.86
	400-640	475	6.7
Z6A-LDH	30-148	103	8.60
	148-360	194	23.2
	360-590	445	5.44
Z7A-LDH	30-126	97	8.32
	126-380	187	23.79
	380-625	460	5.51

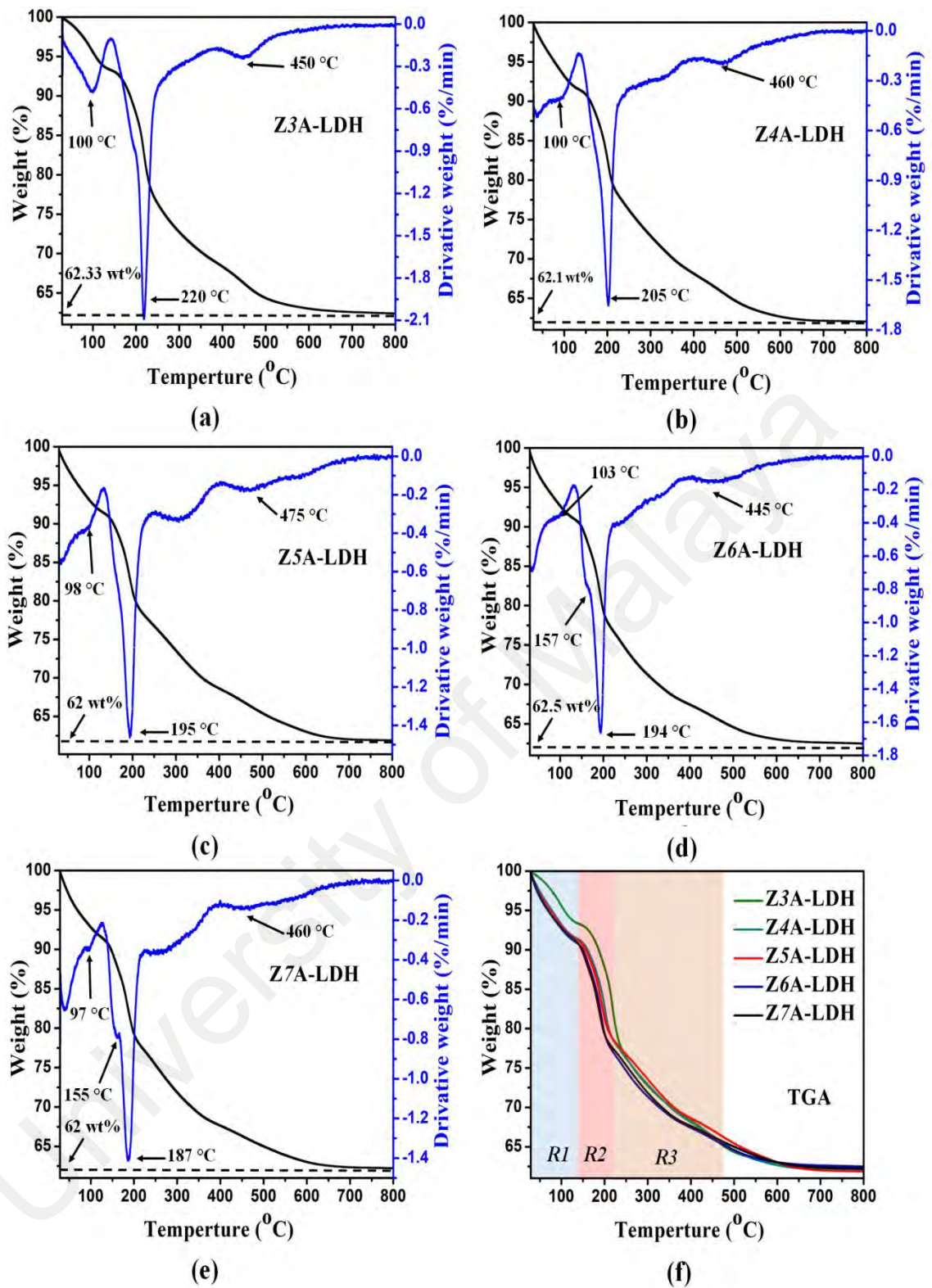


Figure 4.1: TGA-DTG curves of (a) Z3A-LDH (b) Z4A-LDH, (c) Z5A-LDH, (d) Z6A-LDH and (e) Z7A-LDH samples; whereas (f) a comparison between TGA curves.

4.2 Microstructural properties analysis

The microstructural characteristics of the prepared samples (*ZrA-LDH*, *Z6A-MMO-T* and *ZrA-MMO-400*) were analyzed via X-ray diffraction (XRD), field emission scanning electron microscopy (FESEM) and nitrogen (g) adsorption/desorption isotherms. The corresponding findings are discussed thoroughly in the following sections:

4.2.1 X-ray Diffraction

In this section, the structural analysis of pristine samples (*ZrA-LDH*) using XRD technique is demonstrated. Figure 4.2 shows the XRD patterns of pristine *ZrA-LDH* samples at different molar ratios, where r (3, 4, 5, 6 and 7) represents the molar ratio of Zn^{+2} to Al^{+2} . Generally, all of the diffraction patterns can be indexed to Zn/Al-LDH structure (JCPDS No: 38-0486). Specifically, there are four main peaks detected in each of the XRD patterns, which correspond to basal planes of (003), (006) and (009) and non-basal plane of (110) in LDH matrix (Ali Ahmed *et al.*, 2013; Yingli Yang *et al.*, 2017). Other additional peaks detected in the spectrum of all the samples could be indexed to ZnO hexagonal wurtzite structure around $2\theta \sim 34$ of JCPDS No: 36-1451. In addition, these peaks have become more pronounced particularly in the spectrum of *Z6A-LDH* and *Z7A-LDH* samples, indicating the favourable formation of ZnO network at low crystallinity (Ali Ahmed *et al.*, 2013; Yingli Yang *et al.*, 2017). Upon increasing the molar ratio, it was found that all synthesized *ZrA-LDH* samples exhibited a positive peak shift towards higher 2θ , signifying the occurrence of lattice distortion occurred in LDH unit cells. Additional peak was noticed at $2\theta \sim 65^\circ$ which is indexed to the ZnAl_2O_4 spinel phase (JCPDS No. 05-0669).

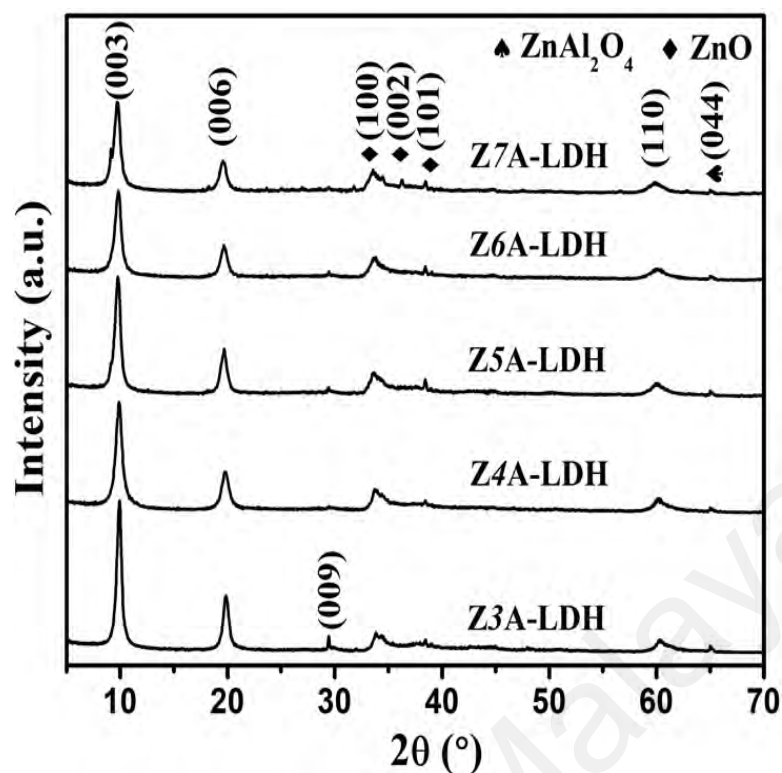


Figure 4.2: X-ray diffraction patterns of ZrA -LDH prepared at different molar ratios, where $r = 3, 4, 5, 6$ and 7 .

To further validate the above phenomena, an in-depth analysis in relation to lattice parameters a and c of pristine ZrA -LDH samples was conducted, as summarized in Table 4.2. In particular, parameters a and c were calculated via the relation: $a = 2d_{110}$ as well as $c = 2d_{003} = 6d_{006}$, respectively, where d presents the distance between the LDH layers. It must be mentioned that parameter a is related to the adjacent cation distance in the Brucite layer, however, parameter c is closely attendant to the anion interlayer, anion size and hydration (Ali Ahmed, Talib, Hussein, *et al.*, 2012; Velu *et al.*, 1997). As illustrated in Table 4.2, the lattice parameter a value increased remarkably from 0.306 to 0.309 nm as the molar ratio increased from 3 to 6. This behavior is due to LDH unit cell lattice expansion which in turn can be attributed to the difference in ionic radius of Al^{+3} to Zn^{+2} (ionic radius of 0.51 and 0.74 nm for Al^{+3} and Zn^{+2} , respectively) (Salih *et al.*, 2018). Simultaneously, this finding reveals that the substitution of LDH matrix (Zn^{+2} into Al^{+3}) is highly favorable at higher molar ratio. In the meanwhile, parameter c

showed almost the same trend of parameter a . Similarly, the increasing value of parameter c can be ascribed to the difference in columbic attraction among the existing interlayer ion in ZrA -LDH matrix (Ali Ahmed, Talib, *et al.*, 2012b; Tao *et al.*, 2012). The results of this study agree well with previous findings by other researches which indicates the successful synthesis of ZrA -LDH materials (Yingli Yang *et al.*, 2017).

Table 4.2: In-depth analysis of pristine ZrA -LDH synthesized at different molar ratios.

Sample	d_{110} (nm)	Lattice parameter (nm)	
		a	c
Z3A-LDH	0.153	0.306	2.663
Z4A-LDH	0.154	0.307	2.695
Z5A-LDH	0.154	0.307	2.711
Z6A-LDH	0.154	0.309	2.694
Z7A-LDH	0.155	0.309	2.715

The effect of thermal treatment temperature on the structural modifications of $Z6A$ -MMO- T samples at various temperatures (200, 300, 350, 400, 450 and 500 °C) were also examined using X-ray diffractometer (samples are herein denoted as $Z6A$ -MMO- T , where T represents the thermal treatment temperature). Figure 4.3 (a) illustrates the XRD patterns of $Z6A$ -MMO- T at different thermal treatment temperatures. In general, thermal treatment temperatures below 180 °C showed no effect on LDHs structure (Ali Ahmed, Talib, *et al.*, 2012b), and thus values of 200 °C and higher were considered for this study. In comparison with XRD pattern of $Z6A$ -LDH (Figure 4.2), there was no LDH basal plane detection in the spectra of $Z6A$ -MMO- T samples after thermal treatment at 200 °C and above (Figure 4.3, a). Nevertheless, the detection of the pronounced diffraction peaks between 2θ of 30° and 40°, which can be indexed to ZnO hexagonal Wurtzite structure (JCPDS No. 89-1397) and $ZnAl_2O_4$ spinel planes (044) at 65.5° (JCPDS No. 05-0669), in the spectra directly evidences the successful crystal phase formation in $Z6A$ -MMO- T samples after thermal treatment. Furthermore, the

intensity of the Z6A-*MMO-T* average peak planes (100, 002 and 101) augmented as the thermal treatment temperature increased, Figure 4.3 (b) (Z. Fang *et al.*, 2005), which in turn indicates an improvement of these peaks formation and crystallinity (Hussein *et al.*, 2002). This increase in the intensity could be due to high thermal treatment temperature provided improvement in the electron mobility which is due to the decrease of MMO matrix defects and subsequently enhance the quality of the resulting porous materials.

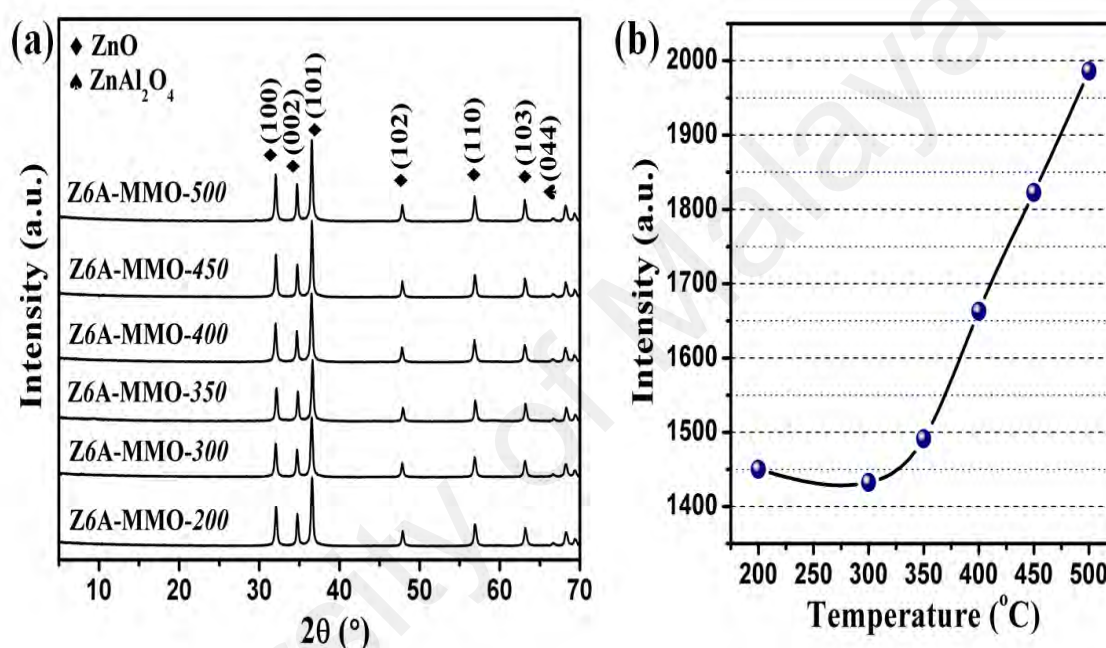


Figure 4.3: (a) X-ray diffraction patterns of Z6A-*MMO-T* prepared at different temperatures, where $T = 200, 300, 350, 400, 450$ and 500 °C; and (b) average (100), (002) and (101) planes intensity of Z6A-*MMO-T*.

To further optimize the effect of molar ratio on the microstructural properties after thermal treatment of *ZrA-LDH* samples, an X-ray diffraction analysis was carried out for the prepared *ZrA-*MMO-400** samples and depicted in Figure 4.4 (a) (where r represents the molar ratio, 3, 4, 5, 6 and 7). Generally, all named samples exhibited diffraction peaks of which can be indexed to ZnO hexagonal Wurtzite structure (JCPDS No. 89-1397), namely (100), (002) and (101) planes at $2\theta \sim 32^\circ, 34^\circ$ and 36° . Furthermore, additional peak was noticed at $2\theta \sim 65.5^\circ$ which is corresponded to ZnAl_2O_4 spinel structure (JCPDS No. 05-0669). These findings evidence a successful

phase formation of mixed metal oxides after thermal treatment of LDH at 400 °C. This indication was found together without any LDH basal planes record indicating the disappearance of LDH structure. Additional peak related to $ZnAl_2O_4$ spinel was noticed at $2\theta \sim 38.5^\circ$. This observation was only found at low molar ratios where the concentration of Al^{+3} is high (Z3A, Z4A-*MMO-400*). In the meanwhile, the mentioned peak was not traceable at high molar ratios (samples Z6A and Z7A-*MMO-400*) due to low Al^{+3} concentration. Continuously, Figure 4.4 (b) shows a variation of the average peaks intensity (100, 002 and 101). It can be clearly observed that increasing the molar ratio of Zn^{+2} to Al^{+3} resulted in higher intensity of the pronounced peaks which indicates higher crystallinity of the prepared *ZrA- $MMO-400$* at higher molar ratios.

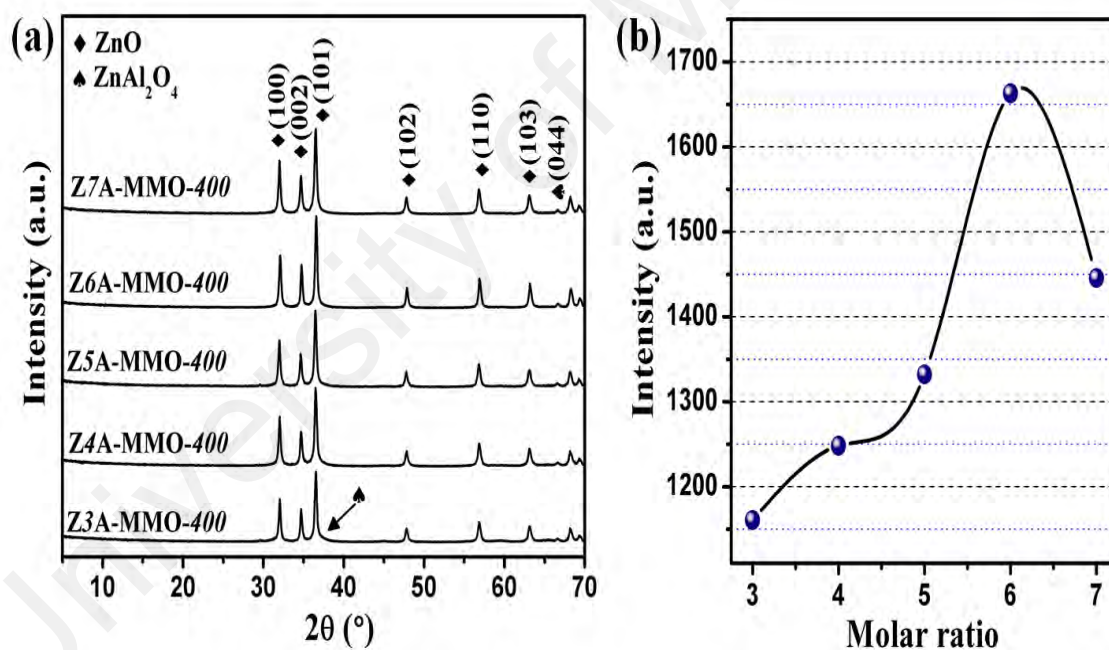


Figure 4.4: (a) X-ray diffraction patterns of thermally treated *ZrA- $MMO-400$* prepared at different molar ratio where $r = 3, 4, 5, 6$ and 7 ; and (b) average (100), (002) and (101) planes intensity of *ZrA- $MMO-400$* .

4.2.2 Field emission scanning electron microscopy

In this section, the surface morphology of pristine ZrA -LDHs and prepared $Z6A$ -MMO- T and ZrA -MMO-400 samples are analyzed using FESEM technique. All samples, regardless of the molar ratio and/or thermal treatment temperature variation, are presented in 1 μm scale bar.

Figure 4.5 (a-e) shows the surface morphology images of ZrA -LDH, where $r = 3, 4, 5, 6$ and 7 . Generally, it can be noticed from Figure 4.5 that all LDH layers are uniform and compact on the FTO substrate. In particular, pristine $Z3A$ -LDH showed almost darkness morphology with a solid granular film formed on FTO substrate (Figure 4.5, a). As for pristine $Z4A$ -LDH, Figure 4.5 (b), the granular layer started to disappear with transformation into a continuous mesoporous film with almost vertically aligned sheets like structure existing and thickness of ~ 60 nm (R. Zhang *et al.*, 2008). This indication was further noticed in pristine $Z5A$ -LDH (Figure 4.5, c). As the molar ratio increased, however, less granular nature was traceable with higher density of Zn/Al-LDH sheets like as can be seen in pristine $Z6A$ and $Z7A$ -LDH (Figure 4.5 (d-e)). This observation could be due to the formation of ZnO phase at high molar ratio of Zn^{+2} to Al^{+3} , as it was demonstrated in the XRD outcomes. Continuously, the size of porosity of the prepared ZrA -LDH pristines was estimated by taking multi points of FESEM images using ImageJ software. Pristine $Z3A$ -LDH exhibited low average porosity of 19.5 nm which can be attributed to the granular nature of the mentioned sample. In the meanwhile, pristine $Z6A$ -LDH showed higher porosity of 42 nm in average. This indication makes the optimum sample ($Z6A$ -LDH) to be further optimized in terms of thermal treatment temperature, whereas higher porosity is favourable for dye-sensitized solid-state devices application since it delivers higher dye loading on the surface of the prepared anode materials (Al-Kahlout, 2015; Ye *et al.*, 2015; Q. Zhang *et al.*, 2009). Pristine $Z4A$, $Z5A$ and $Z7A$ -LDH showed average porosities of 27, 36 and 29 nm,

respectively. It can be concluded that higher average porosity was observed as the molar ratio increased (Z. Fang *et al.*, 2005; Zhu *et al.*, 2017).

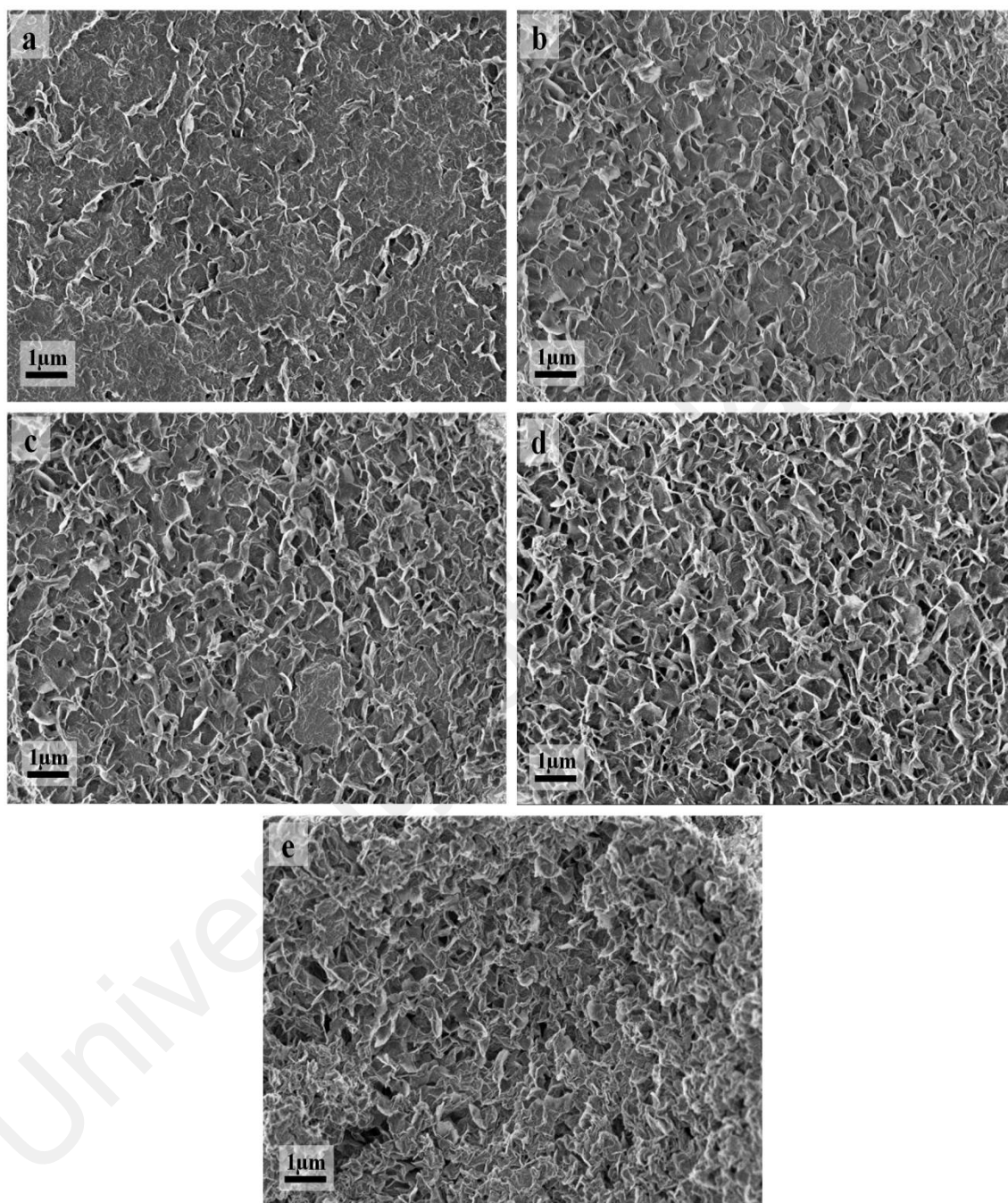


Figure 4.5: FESEM images of the pristine ZrA -LDH at different molar ratios; (a) Z3A-LDH, (b) Z4A-LDH, (c) Z5A-LDH, (d) Z6A-LDH and (e) Z7A-LDH.

The effect of thermal treatment temperature on the morphological properties was further analyzed for Z6A- $MMO-T$ samples as illustrated in Figure 4.6 (a-f), where $T = 200, 300, 350, 400, 450$ and 500 °C. In general inspection, the prepared anode materials

were found to be uniform and compact on the FTO substrate. In addition, it was also observed from Figure 4.6 that a perpendicular sheets structure with mesoporous nature was maintained and these sheets exhibited average of ~ 75 nm in thickness, regardless of thermal treatment temperature increment. Such a structure is believed to be promising for electron transport from the photo-generation point to the collector electrode in dye-sensitized solid-state devices, also, promising for diffusion of the electrolyte through the sheets which in turn results in lower sheet resistance and recombination rate (Al-Kahlout, 2015; Q. Zhang *et al.*, 2009). Thermal treatment temperature at 200 °C, Figure 4.6 (a), did not show clear effect on the morphological structure as compared to its pristine LDH precursor, where Z6A-MMO-200 sample showed almost the same structure of that in Z6A-LDH (Figure 4.5, d). In the meanwhile, further increment of the thermal treatment from 200 to 350 °C, Figure 4.6 (b-c), increased the porous nature of the prepared samples with low existence of granular structure. The samples treated at 400 and 450 °C showed a homogeneous distribution and ordered film (inset of Figure 4.6 (d-e)). Thermal treatment temperature higher than 350 °C was found to be favorable in term of the growth of sheet like structure with higher porosity nature. However, thermal treatment at 500 °C showed a distortion in the sheets structure and more compact nature with less pores which is considered a drawback for dye-sensitized solid-state devices applications since it exhibits lower surface area and subsequently lower dye loading on the prepared anode materials surface. The above hypothesis was further validated through a variation of the measured average porosity as a function of thermal treatment temperature. It was found that thermal treatment temperature as low as 200 °C exhibited average porosity of 46.5 nm whereby increasing the temperature to 300 and 350 °C resulted in porosity of 47 and 62 nm, respectively. The highest average porosity value was obtained at 400 °C (68.5 nm) before further decreased to 36 nm at 500 °C.

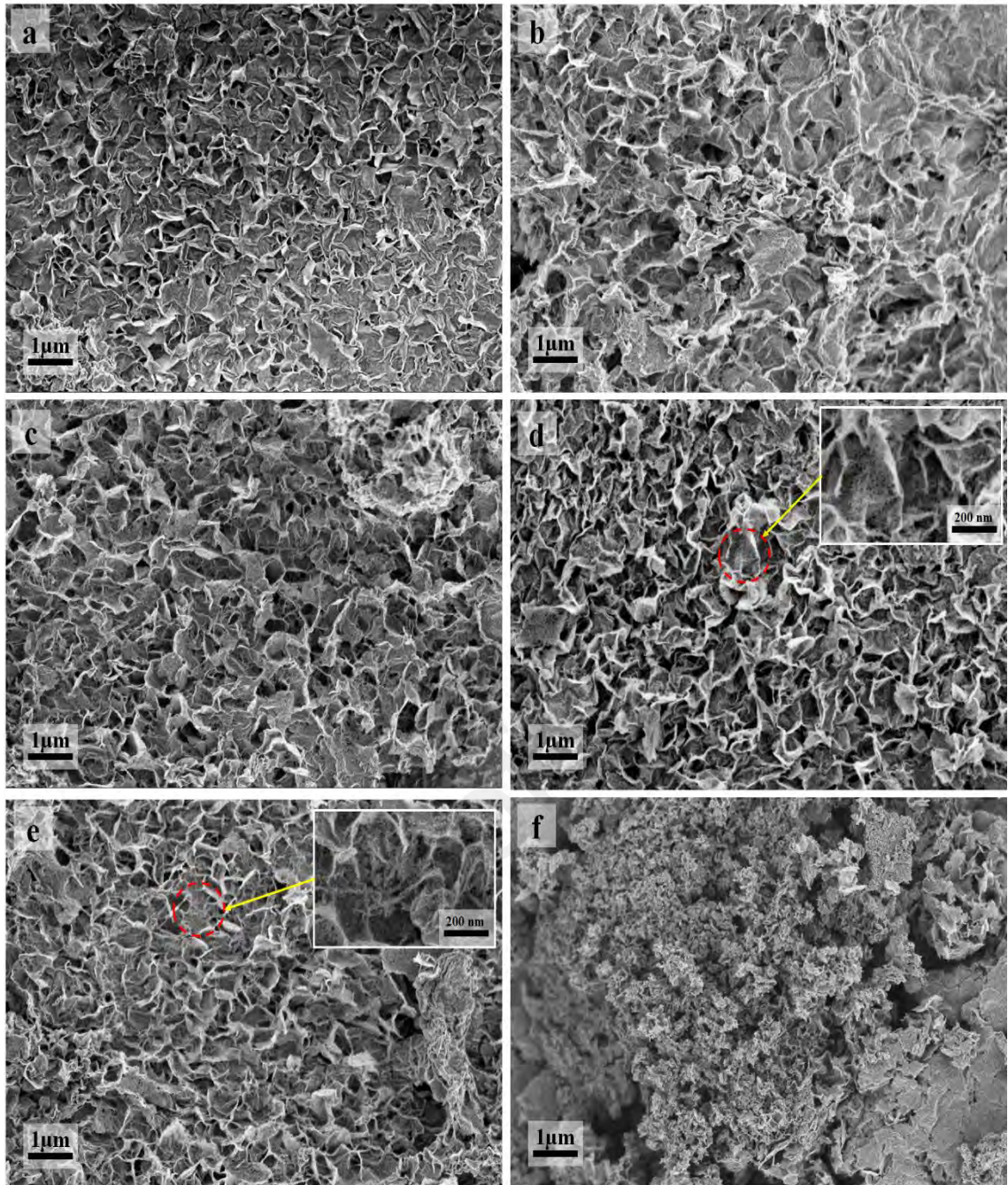


Figure 4.6: FESEM images of the prepared Z6A-*MMO-T* at different thermal treatment temperatures; (a) Z6A-*MMO-200*, (b) Z6A-*MMO-300*, (c) Z6A-*MMO-350*, (d) Z6A-*MMO-400*, (e) Z6A-*MMO-450* and (f) Z6A-*MMO-500*.

The surface morphology of the prepared Z*r*A-*MMO-400* samples at different molar ratios are presented in Figure 4.7 (a–e), where $r = 3, 4, 5, 6$ and 7. Notably, a continuous solid granular film formed on the surface of the FTO substrate for Z3A-*MMO-400* sample was noticed (Figure 4.7, a). Z3A-*MMO-400* sample showed very low porous nature as compared to samples with higher molar ratio. After the Zn^{2+} ratio was

increased, the granular structure started to transform into a sheet-like layer with mesoporous nature (Figure 4.7, b). The average thickness of these sheets was found to be 65 nm. Continuously, increasing the molar ratio (Z5A and Z6A-*MMO-400*) resulted in ordered mesoporous film as depicted in Figure 4.7 (c-d). There was no trace of granular film in sample Z5A-*MMO-400* onward. When the molar ratio exceeded 6 (sample Z7A-*MMO-400*), the film started to grow continuously with small void because of the coalescence effect (Lehtinen & Zachariah, 2001). In addition, some nanoparticles merged and formed a single continuous film. This phenomenon is intended to achieve a thermodynamic stability in the perturbed crystal growth system.

The above hypothesis was further validated through the calculated porosity of the prepared ZrA-*MMO-400* samples. The porosity size between the sheets of the nanostructured film increased from ~44 to ~68.5 nm when the molar ratio increased from 4 to 6. However, porous size was decreased to ~ 32.5 nm when the molar ratio further increased (Z7A-*MMO-400*). It can be clearly observed that increasing the molar ratio led to increase in the porous size. Evidently, the aspect surface ratio of the nanostructure was linearly dependent on the incorporated molar ratio. In contrast, FESEM findings suggest that a molar ratio of 6 is the optimum ratio since it delivered the highest porous nature with well distributed sheet like structure. As stated previously, higher porosity is required for higher dye loading (Al-Kahlout, 2015; Hosono *et al.*, 2005; Ye *et al.*, 2015). It was also found that sample prepared at molar ratio 3 and 5 (Z3A-*MMO-400* and Z5A-*MMO-400*) exhibited average porosities of 13 and 47 nm, respectively.

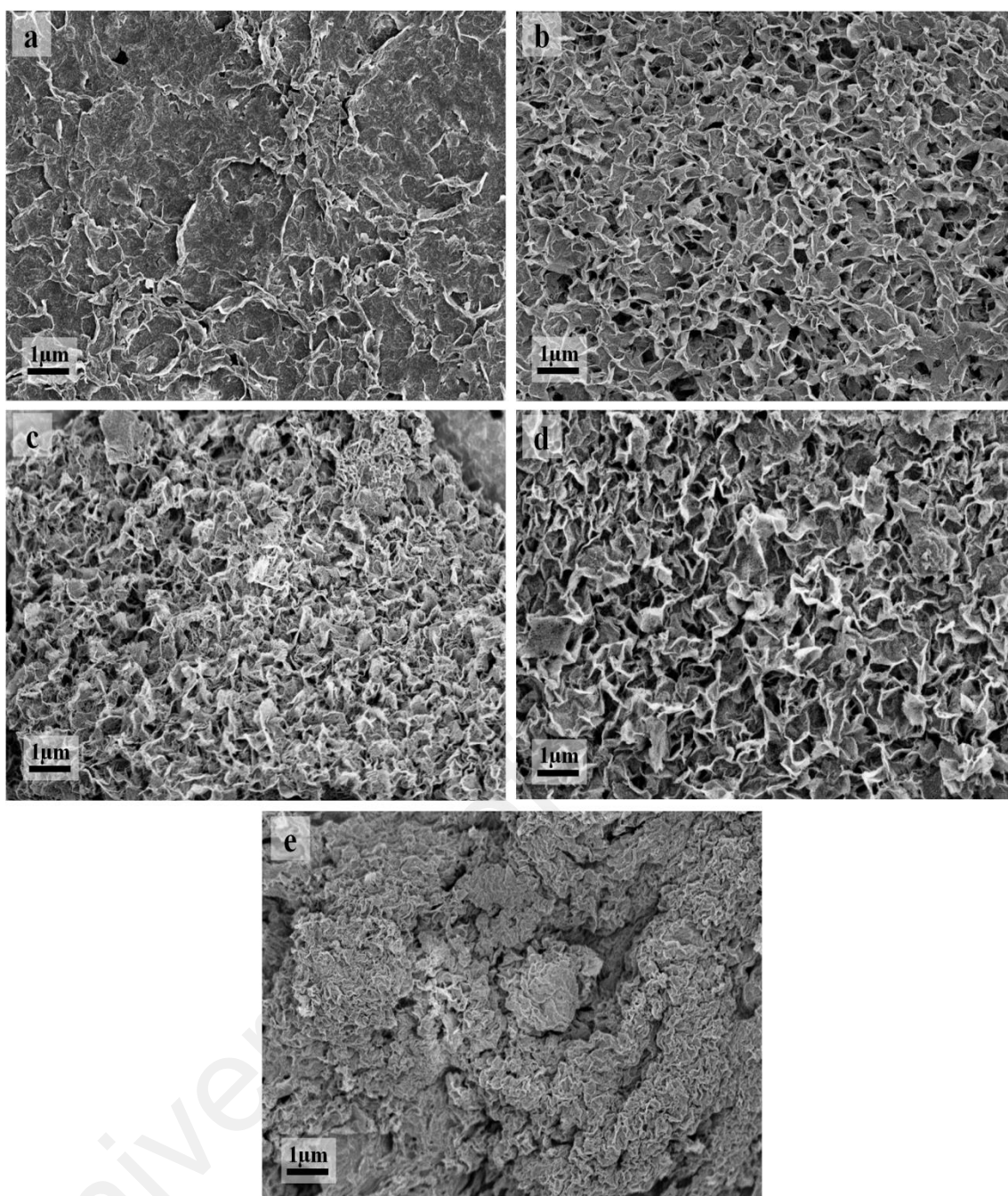


Figure 4.7: FESEM images of the prepared ZrA -MMO-400 at different molar ratios; (a) Z3A- MMO-400, (b) Z4A- MMO-400, (c) Z5A- MMO-400, (d) Z6A- MMO-400 and (e) Z7A- MMO-400.

4.2.3 Surface area, pore volume and pore size analysis

To study the effect of thermal treatment temperature as well as molar ratio alterations on the physical properties of *Z6A-MMO-T*, *ZrA-MMO-400* and pristine *Z6A-LDH* samples, a nitrogen adsorption/desorption isotherms analysis was used and demonstrated in this section.

Figure 4.8 shows the nitrogen adsorption/desorption isotherms for *Z6A-MMO-T* samples treated at different thermal treatment temperatures ranging from 200 to 500 °C, where $T = 200, 300, 350, 400, 450$ and 500 °C. All adsorption/desorption isotherms are Type IV with H_3 hysteresis loop which exhibit high adsorption at relative high pressure (P/P_0), suggesting the occurrence of mesoporous anode materials in accordance with IUPAC classification (Sing, 1985). In contrast, the evaluated surface area via multi-points BET method is summarized in Figure 4.9 and Table 4.3. Mainly, two stages could be observed for the BET surface area profile: an increase in BET surface area with the thermal treatment temperature increased to 400 °C (sample *Z6A-MMO-400*, 53 m²/g) followed by a reduction as the thermal treatment temperature further increased (samples *Z6A-MMO-450* and *Z6A-MMO-500*). Upon thermal treatment of pristine *Z6A-LDH*, the formation of ZnO phase and ZnAl₂O₄ spinel at low temperatures resulted in the porous structure formation which in turn gave rise to the BET surface area as can be seen in FESEM and XRD corresponding findings. However, the reduction in the BET surface area at temperatures higher than 400 °C (450 and 500 °C) could be attributed to the distortion upon higher temperature as demonstrated in the FESEM analysis (J. Song *et al.*, 2012).

On the contrary, the pore size distribution of the prepared *Z6A-MMO-T* samples was calculated via Barrett-Joyner-Halenda (BJH) approach from the adsorption isotherms branch. The pore size was found to be evolved in the opposite direction to those of BET

surface area (Table 4.3), whereas the lowest value was obtained for sample Z6A-MMO-400, and continuously, the pore size value was increased at thermal treatment temperatures above 400 °C (samples Z6A-MMO-450 and Z6A-MMO-500). As previously mentioned in chapter 2, section 2.1.1, higher BET surface area with mesoporous structure is favorable in dye-sensitized solid state devices as it delivers higher dye loading which in turn leads to higher device performance (Al-Kahlout, 2015; Yuan *et al.*, 2017). This claim is also supported by FESEM analysis, section 4.2.2, where higher porous percentage leads to wider area loaded with dye and subsequently efficient visible light harvesting and higher photocurrent magnitude.

In term of nanoparticles pore volume, Table 4.3 and Figure 4.9, the lowest value was obtained for sample Z6A-MMO-400 (0.10 cm³/g) and the highest for samples Z6A-MMO-500 (0.19 cm³/g). These results could be explained by the thermal treatment effect which resulted in the LDH layered structure collapse as well as the formation of ZnAl₂O₄ spinal. This may cause the occurrence of low pore size and subsequently lower pore volume (Ahmed *et al.*, 2012a; Cheng *et al.*, 2010a).

Table 4.3: Surface area, pore volume and average pore size of the prepared Z6A-
MMO-*T* samples at different thermal treatment temperatures.

Sample	Surface area (m²/g)	Pore volume (cm³/g)	Average pore size (nm)
Z6A-MMO-200	32	0.13	16
Z6A-MMO-300	38	0.14	14
Z6A-MMO-350	40	0.13	12
Z6A-MMO-400	53	0.10	7
Z6A-MMO-450	51	0.17	12
Z6A-MMO-500	46	0.19	16

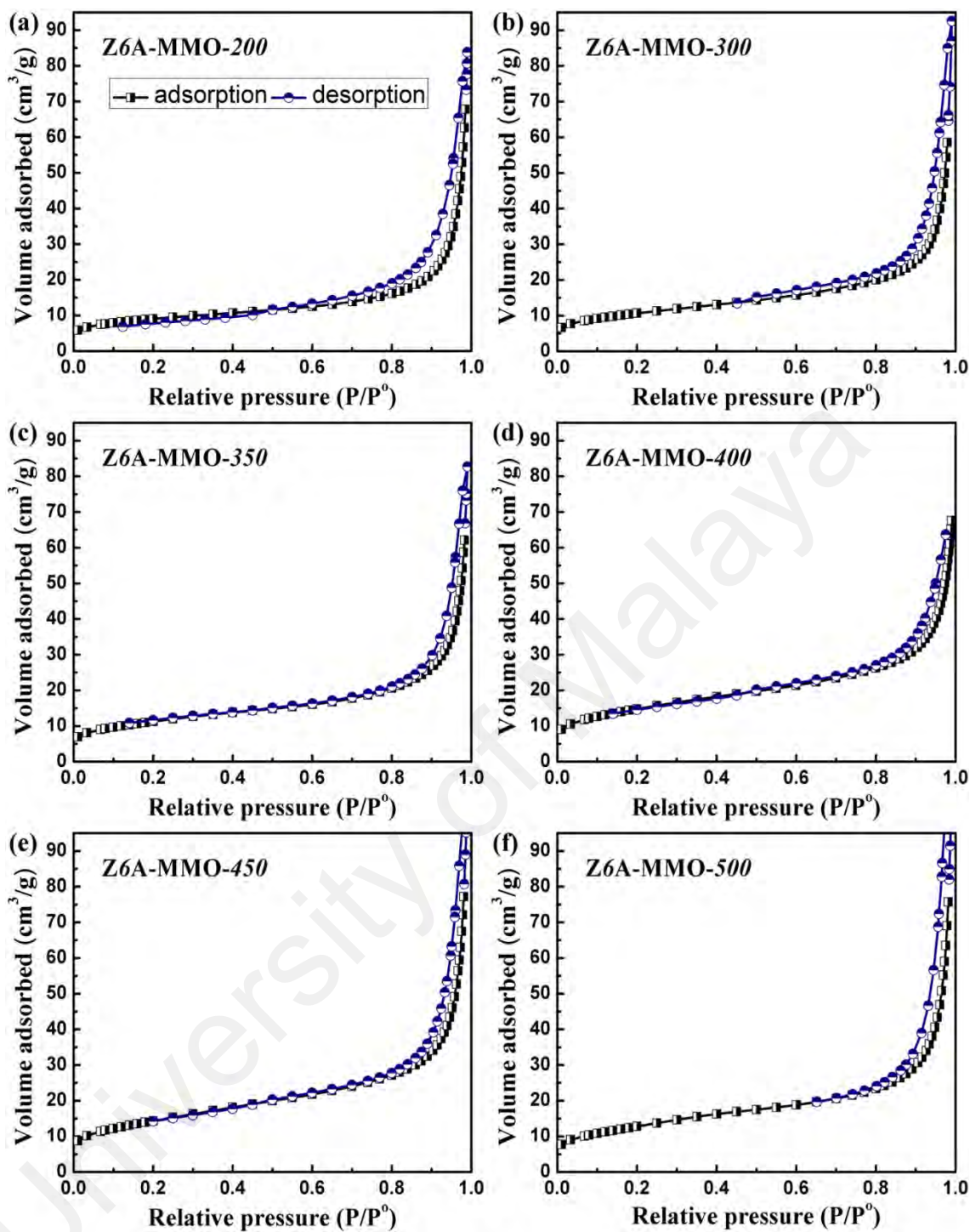


Figure 4.8: Nitrogen adsorption/desorption isotherms of Z6A-MMO-*T* samples; (a) Z6A-MMO-200, (b) Z6A-MMO-300, (c) Z6A-MMO-350, (d) Z6A-MMO-400, (e) Z6A-MMO-450 and (f) Z6A-MMO-500.

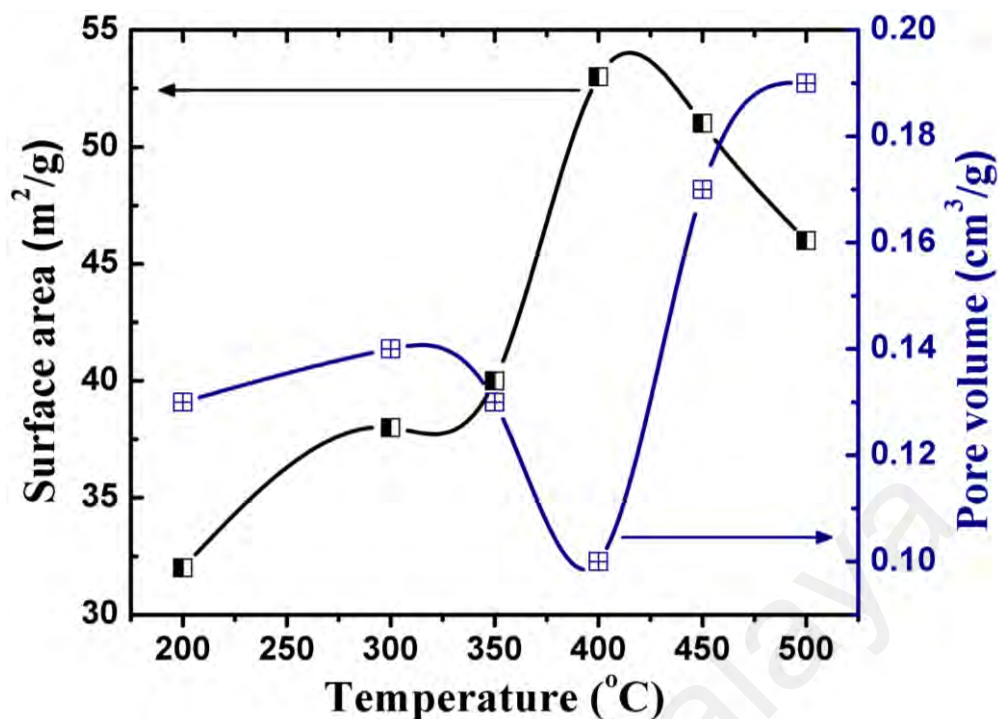


Figure 4.9: Surface area and pore volume of Z6A-*MMO-T* samples, where $T = 200, 300, 350, 400, 450$ and 500 °C.

Figure 4.10 shows the nitrogen adsorption/desorption isotherms for *ZrA- $MMO-400$* samples prepared at different molar ratios, where $r = 2, 3, 4, 5,$ and 6 . As shown in Figure 4.10, all the prepared *ZrA- $MMO-400$* samples are Type IV with H_3 hysteresis loop which exhibited no limited adsorption at relative high pressure (P/P_0) (Sing, 1985). This is commonly observed with mesoporous nanomaterials structure. In contrast, the evaluated BET surface area, pore volume and average pore size are illustrated in Figure 4.11 and summarized in Table 4.4. Increasing the molar ratio resulted in increasing the surface area of the prepared samples whereas samples *Z3A* and *Z6A- $MMO-400$* exhibited BET surface area of 39 and 53 m²/g, respectively. This finding can be ascribed to the increment in porous segregation phenomena through thermal treatment process which leads to high BET surface area in sample *Z6A- $MMO-400$* . This can also be seen in FESEM analysis whereby a homogenous film was formed with high quality porous. Subsequently, the BET surface area was decreased when the molar ratio was increased to 7 (*Z7A- $MMO-400$*). It is believed that such phenomenon is related to

different structural features after thermal treatment at 400 °C: as shown in the corresponding FESEM images.

Meanwhile, as demonstrated in Table 4.4, the pore size distribution ranging from 7 to 8 nm. The average pore diameters were found to follow the molar ratio order: 4 > 3 > 7 > 6 > 5. This differences could be explained by the formation of the oxides after the thermal treatment, which in turn resulted in the large pores collapse and subsequently decrease the average pore size (L. Zhang *et al.*, 2016).

In term of nanoparticles pore volume, Figure 4.11 and Table 4.4, it can be observed that, generally, increasing the molar ratio resulted in increment in the pore volume where sample Z3A-*MMO-400* exhibited a value of 0.08 cm³/g whereas sample Z6A-*MMO-400* showed value of 0.10 cm³/g. It was found that the pore volume trend, generally, in a good accordance with those of BET surface area. This can be explained via the higher surface area obtained which might results in higher volume adsorbed onto the prepared Z6A-*MMO-400* and Z7A-*MMO-400* samples.

Table 4.4: Surface area, pore volume and average pore size of the prepared ZrA-*MMO-400* samples at different molar ratio.

Sample	Surface area (m ² /g)	Pore volume (cm ³ /g)	Average pore size (nm)
Z3A- <i>MMO-400</i>	39	0.08	8
Z4A- <i>MMO-400</i>	40	0.09	8
Z5A- <i>MMO-400</i>	44	0.07	6
Z6A- <i>MMO-400</i>	53	0.10	7
Z7A- <i>MMO-400</i>	51	0.10	7

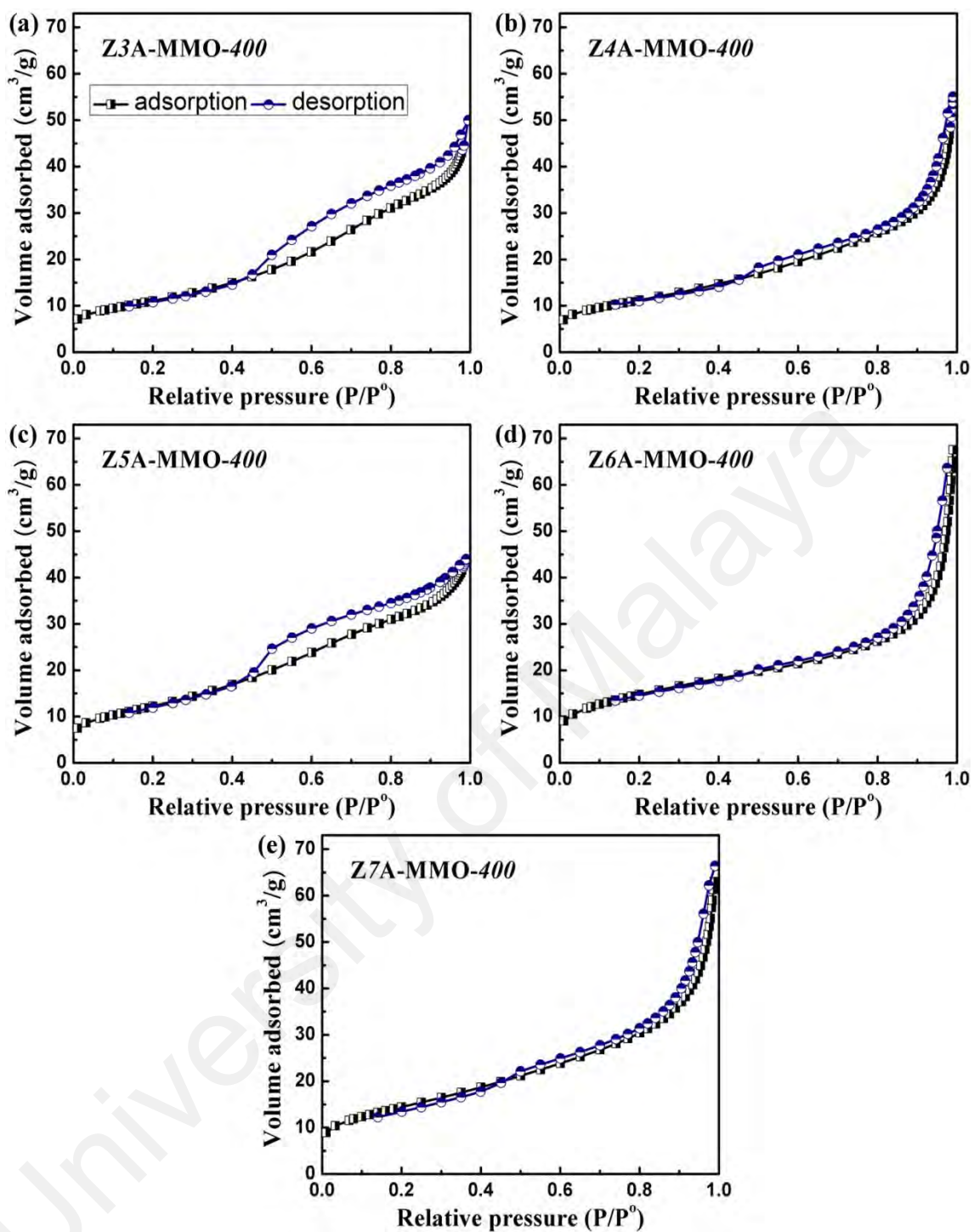


Figure 4.10: Nitrogen adsorption/desorption isotherms of ZrA-*MMO-400* samples; (a) Z3A-*MMO-400*, (b) Z4A-*MMO-400*, (c) Z5A-*MMO-400*, (d) Z6A-*MMO-400* and (e) Z7A-*MMO-400*.

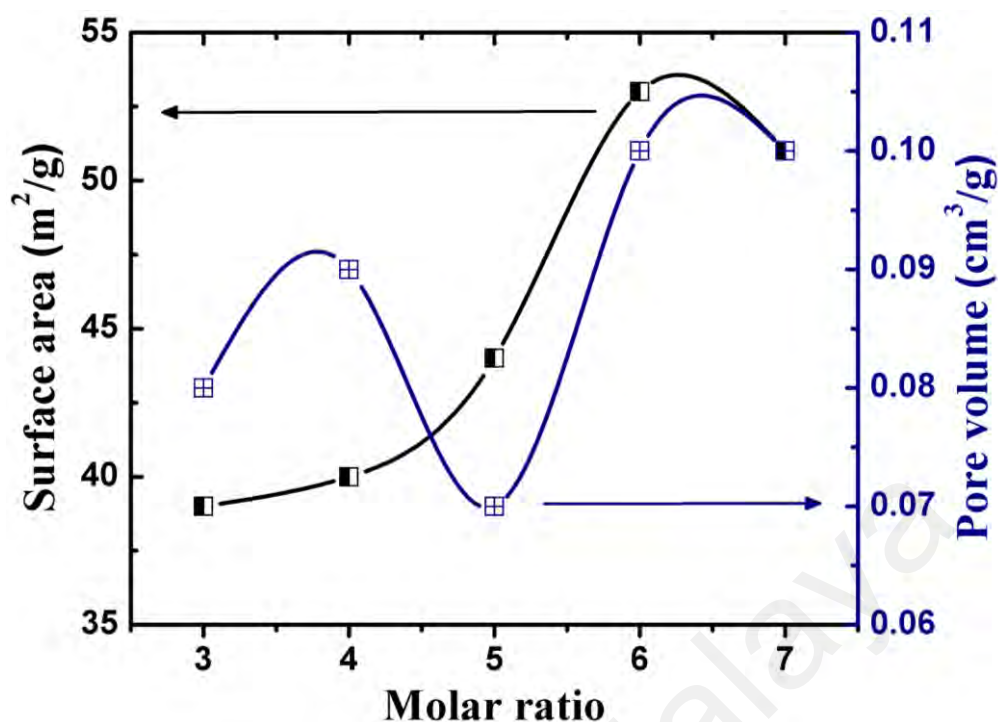


Figure 4.11: Surface area and pore volume of ZrA-*MMO-400* samples, where $r = 3, 4, 5, 6$ and 7 .

Figure 4.12 shows adsorption/desorption isotherm comparison between pristine Z6A-LDH and the prepared Z6A-*MMO-400*. As depicted in Figure 4.12, pristine Z6A-LDH samples is Type IV with H₃ hysteresis loop which is similar to adsorption/desorption isotherm of Z6A-*MMO-400* sample suggesting the presence of mesoporous structure in accordance with IUPAC classification (Sing, 1985). In the surface area investigation, it was found that the pristine sample exhibited low surface area (17 m²/g) as compared to Z6A-*MMO-400* (53 m²/g). In the meanwhile, the average pore size of the pristine sample (14 nm) was found to be increased in comparison to Z6A-*MMO-400* (7 nm). The former can be explained by the collapse of 2D LDH layer structure while the latter is due to thermal treatment effect and ZnAl₂O₄ recrystallization. It was found that these results are in a good agreement with the phase transformation from LDH to MMO as demonstrated in the XRD results analysis. However, the pore volume of the pristine sample was found to be 0.05 cm³/g as compared to 0.10 cm³/g. This can be explained by the low porosity of the former as compared to Z6A-*MMO-400*.

The presented results, regardless of thermal treatment temperature and/or molar ratio variations, were found to be comparable to other researchers' outcomes (Table 4.5) by which it can be concluded that the synthesized ZrA-LDH samples are well-established for further preparation of Z6A-*MMO-T* and ZrA-*MMO-400* which in turn plays a vital role in the DS photodetector performance.

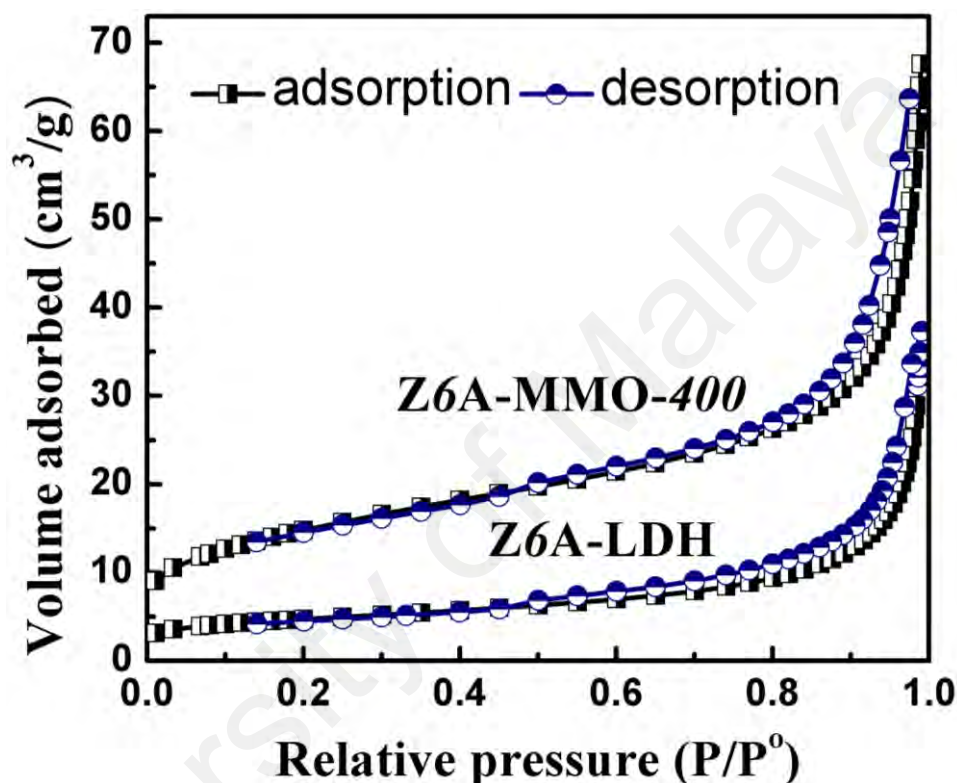


Figure 4.12: Nitrogen adsorption/desorption isotherms of pristine Z6A-LDH and Z6A-*MMO-400* samples.

Table 4.5: Comparison table with other researches' outcomes.

<i>Sample</i>	<i>Surface area (m²/g)</i>	<i>Reference</i>
Pristine LDH	1	(Ahmed <i>et al.</i> , 2012a)
Z2A-<i>MMO-400</i>	9.5	(Zhu <i>et al.</i> , 2017)
Z2A-<i>MMO-400</i>	75	(Cheng <i>et al.</i> , 2010b)
Z4A-<i>MMO-400</i>	20.3	(Zhu <i>et al.</i> , 2017)
Z4A-<i>MMO-400</i>	43	(Ahmed <i>et al.</i> , 2012a)
Z6A-<i>MMO-400</i>	37.3	(Zhu <i>et al.</i> , 2017)

4.3 Optical properties analysis

The optical properties of the prepared samples (*Z6A-MMO-T*, *ZrA-MMO-400* and pristine *Z6A-LDH*) were studied using both ultraviolet-visible (UV-Vis) and photoluminescence (PL) spectroscopies. The corresponding results are discussed in detail in the following sections:

4.3.1 Ultraviolet-visible light spectroscopy

Figure 4.13 demonstrates a schematic diagram of the energy levels of ZnO phase and ZnAl₂O₄ spinel semiconductors together with the transfer process of electron (-) and hole (+) pairs. It was proven that interaction between coupled semiconductors nanocomposite is capable of enhancing the photo-generation process as a function of their UV-vis properties. Subsequently, a good matching between the semiconductors conduction band (CB) and valence band (VB) levels is required; in which the electron (e⁻) and hole (h⁺) pairs from one particle to another (its neighbor) is driven. Theoretically, as depicted in Figure 4.13, the VB top and CB bottom of ZnO dwell at -7.39 and -4.19 eV, respectively. While, in ZnAl₂O₄, the VB top and CB bottom dwell at -7.16 and -3.36 eV, respectively, with respect to the absolute vacuum scale (X. Zhao *et al.*, 2012). Hence, when these two semiconductors are coupled together, any form of radiation could be absorbed by both ZnO as well as ZnAl₂O₄ and yield e⁻ and h⁺ pairs, with respect to their wavelength edge. Upon photo-excitation, electrons in ZnAl₂O₄ CB would travel to that of ZnO; whereas, holes in the ZnAl₂O₄ VB would remain at position. On the contrary, holes in ZnO VB would travel to that of ZnAl₂O₄, while electrons in ZnO CB would remain there (Sampath & Cordaro, 1998; X. Zhao *et al.*, 2012). It is essential to take into consideration that an effective solid-state device does not only depend on the band structure, whereas other factors such as surface area, surface morphology and crystallinity play essential role in elevating the performance.

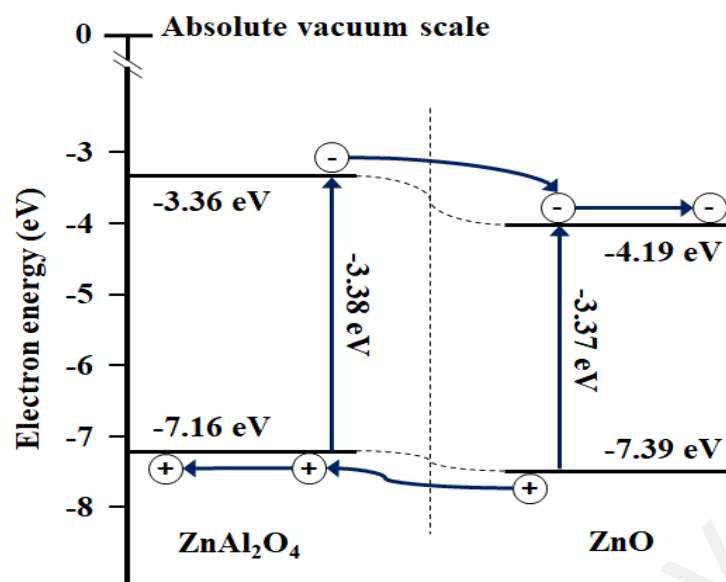


Figure 4.13: Schematic diagram of ZnO and ZnAl₂O₄ energy levels together with their photo-excitation process (X. Zhao *et al.*, 2012).

The relationship between the coupling effect and thermal treatment temperature variation of Z6A-*MMO-T* samples in the final MMO matrix was investigated using UV-Vis technique. Figure 4.14 shows the absorbance spectra of Z6A-*MMO-T* samples at different thermal treatment temperatures ($T = 200, 300, 350, 400, 450$ and 500). The absorption spectra of all the Z6A-*MMO-T* samples exhibited intense UV absorption at ~ 380 nm owing to the near-band edge (NBE) emission that originated from the electronic band transition of ZnO and ZnAl₂O₄ semiconductors matrix (Caglar *et al.*, 2009; Dong *et al.*, 2018; Pérez-Casero *et al.*, 2005). Interestingly, the intensity of the absorption spectra increased with thermal treatment temperature increment from 200 to 500 °C. The obtained redshift in the absorbance spectra indicates that MMO matrix composition became more crystalline as the temperature increased (samples treated at 400, 450 and 500 °C). This behavior can be also attributed to higher crystallinity of ZnO phase and ZnAl₂O₄ spinel as the temperature increased which was proven during the XRD analysis. This finding was manifested by the highest area under the absorption curve, as shown in the inset of Figure 4.14.

To validate the above hypothesis, an in-depth analysis concerning the optical energy band gap was performed via Tauc relation (Foruzin *et al.*, 2016; Salih *et al.*, 2018):

$$(\alpha hv)^{\frac{1}{n}} = C(hv - E_g) \quad (4.1)$$

where α is the absorption coefficient, hv is the photon energy and E_g is the energy band gap. The related results are shown in Figure 4.15 (a-f).

Overall, the prepared Z6A-MMO-*T* samples exhibited a bathochromic shift from 3.3 to 3.21 eV when the temperature increased from 200 to 450 °C. This outcome indicates a formation of narrow electron transition pathways within the MMO electronic band structure which is attributed to ZnO structure associated with ZnAl₂O₄ spinel as illustrated in Figure 4.13. The band gap structure of the prepared samples proposes that there are two types of electron band transitions: a transition between filled O 2*p* and vacant Zn 4*s* orbitals, while the second type of this transition happens between the filled O 2*p* and vacant Al 3*s* orbitals. The former transition is attributed to ZnO band structure while the latter is due to ZnAl₂O₄ spinel (Ahmed *et al.*, 2012a; Sampath & Cordaro, 1998; X. Zhao *et al.*, 2010). In the XRD spectrum (Figures 4.3, a) the intensity and crystallinity of ZnO phase is stronger than those of ZnAl₂O₄ spinel, and thus, the second type of transition is not considered as competitive as the first type (electronic transition in ZnO). This indicates that the calculated band gap is mainly due to ZnO band structure with low association of ZnAl₂O₄ spinel structure. All these findings prove that the energy gaps of MMO matrix coupling mode drives the charge carriers from a nanoparticle to another to generate the required separation between holes and electrons.

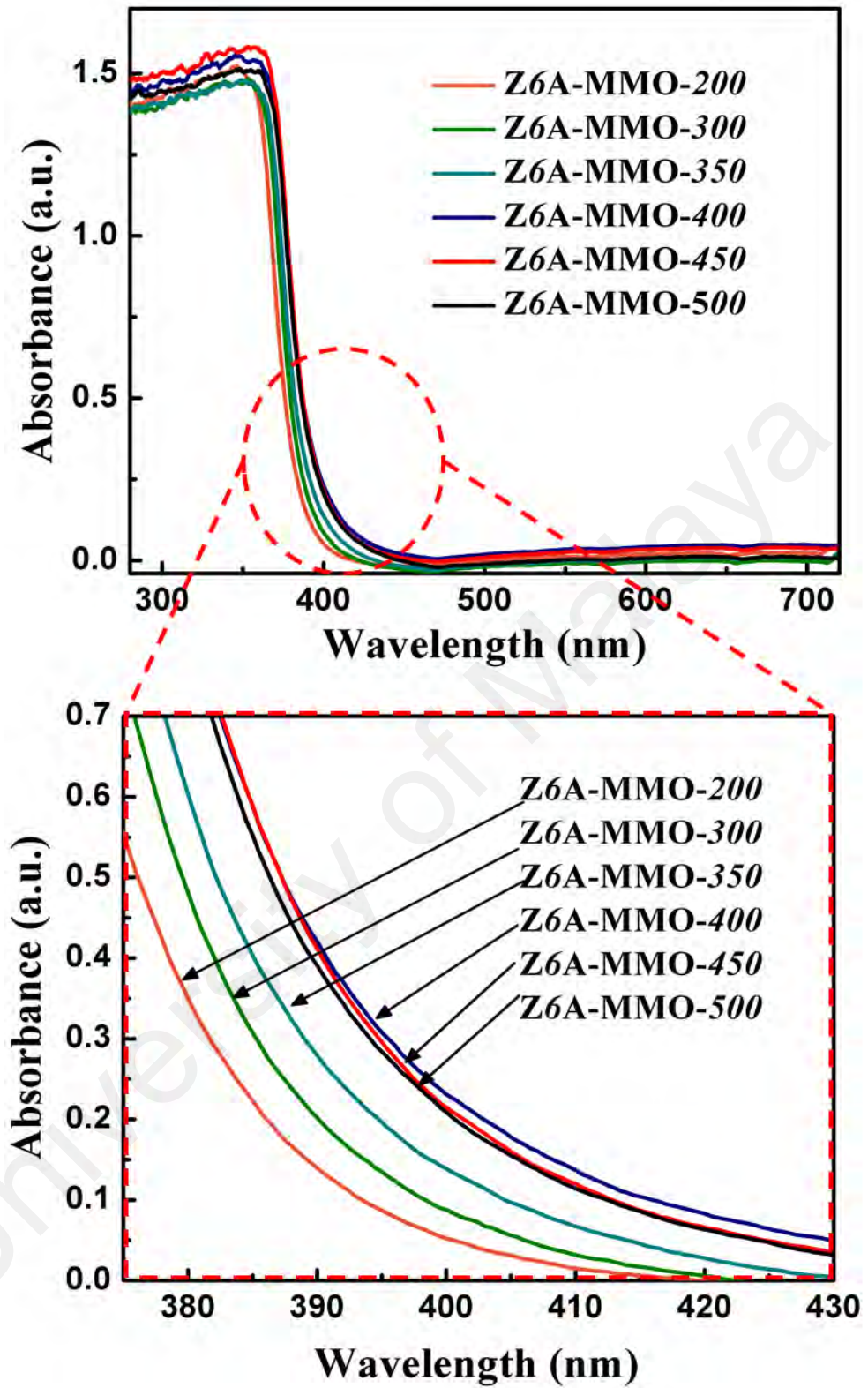


Figure 4.14: Absorbance spectra of Z6A-MMO- T samples at different thermal treatment temperatures ($T = 200, 300, 350, 400, 450$ and 500 °C).

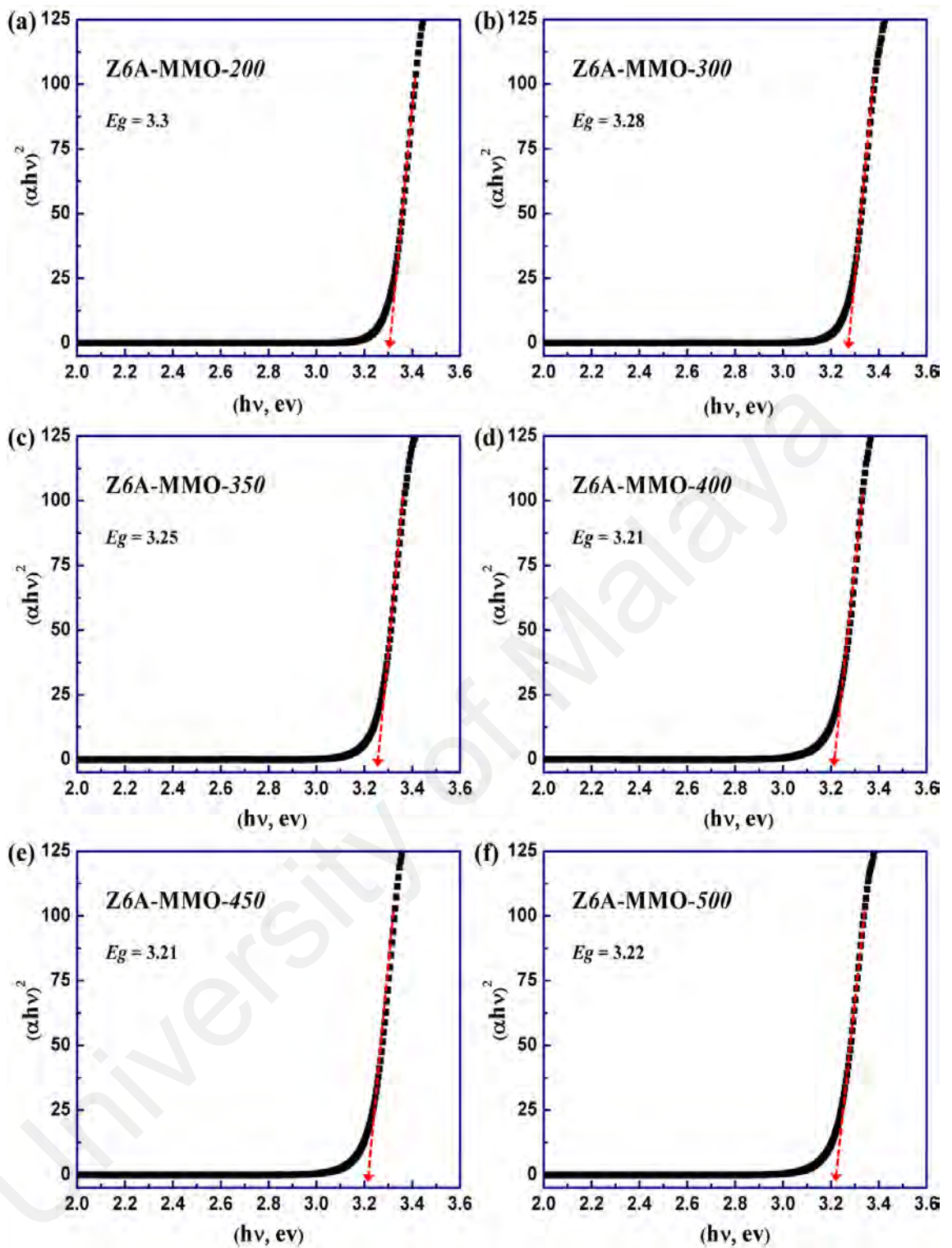


Figure 4.15: Optical band gap of Z6A-MMO- T samples at different thermal treatment temperatures; (a) Z6A-MMO-200, (b) Z6A-MMO-300, (c) Z6A-MMO-350, (d) Z6A-MMO-400, (e) Z6A-MMO-450 and (f) Z6A-MMO-500.

The UV-Vis analysis was also used to study the relationship between ZnO phase and ZnAl₂O₄ spinal coupling effect at different molar ratios of the prepared samples after thermal treatment at 400 °C, where r represents the molar ratio of Zn⁺² to Al⁺³ ($r = 3, 4, 5, 6$ and 7). Figure 4.16 depicts the absorbance spectra of the ZrA-MMO-400 samples prepared at various molar ratios. All ZrA-MMO-400 samples exhibited an intense UV absorption at around 380 nm, which is mainly originated from the direct band edge emission of ZnO and ZnAl₂O₄ semiconductors (L. Zhang *et al.*, 2014; Zhu *et al.*, 2017). It is noteworthy to mention that the intensity of the absorption spectra increased when the molar ratio value increased from 3 to 6 (samples Z3A and Z6A-MMO-400), before being further reduced when the molar ratio was 7 (sample Z7A-MMO-400). The increase can be attributed to the variations in sample thickness during crystal growth. In the proposed MMO system, the molar ratio of Zn⁺² to Al⁺³ showed a significant role on the absorbance spectra range of the final ZrA-MMO matrix, where higher molar ratio resulted in higher absorption range towards the visible light. Among the samples, the Z6A-MMO-400 sample showed the highest absorption range in the near-band edge emission region, affirming the enhanced optical properties of the samples at higher wavelengths. This finding was manifested by the highest area under the absorption curve, as shown in the inset of Figure 4.16.

To validate the above hypothesis, an in-depth analysis concerning the optical energy band edge was performed via Tauc relation (Equation 4.1). The related results are shown in Figure 4.17 (a-e). Overall, samples at low molar ratios (Z3A, Z4A and Z5A-MMO-400) exhibited energy band gap value of ~3.24 eV. Subsequently, a slight bathochromic shift in the energy band gap was acquired when the molar ratio increased to 6 (Z6A-MMO-400), which demonstrated a value of 3.21 eV. This outcome indicated a formation of narrow electron transition pathways within the MMO matrix electronic band structure. However, the energy band gap of the Z7A-MMO-400 sample increased

to 3.22 eV, revealing the Burstein–Moss effect emerging from the excessive density of Zn atom at the bottom of conduction band in MMO crystal lattice (Alshanableh *et al.*, 2016; YH Yang *et al.*, 2007).

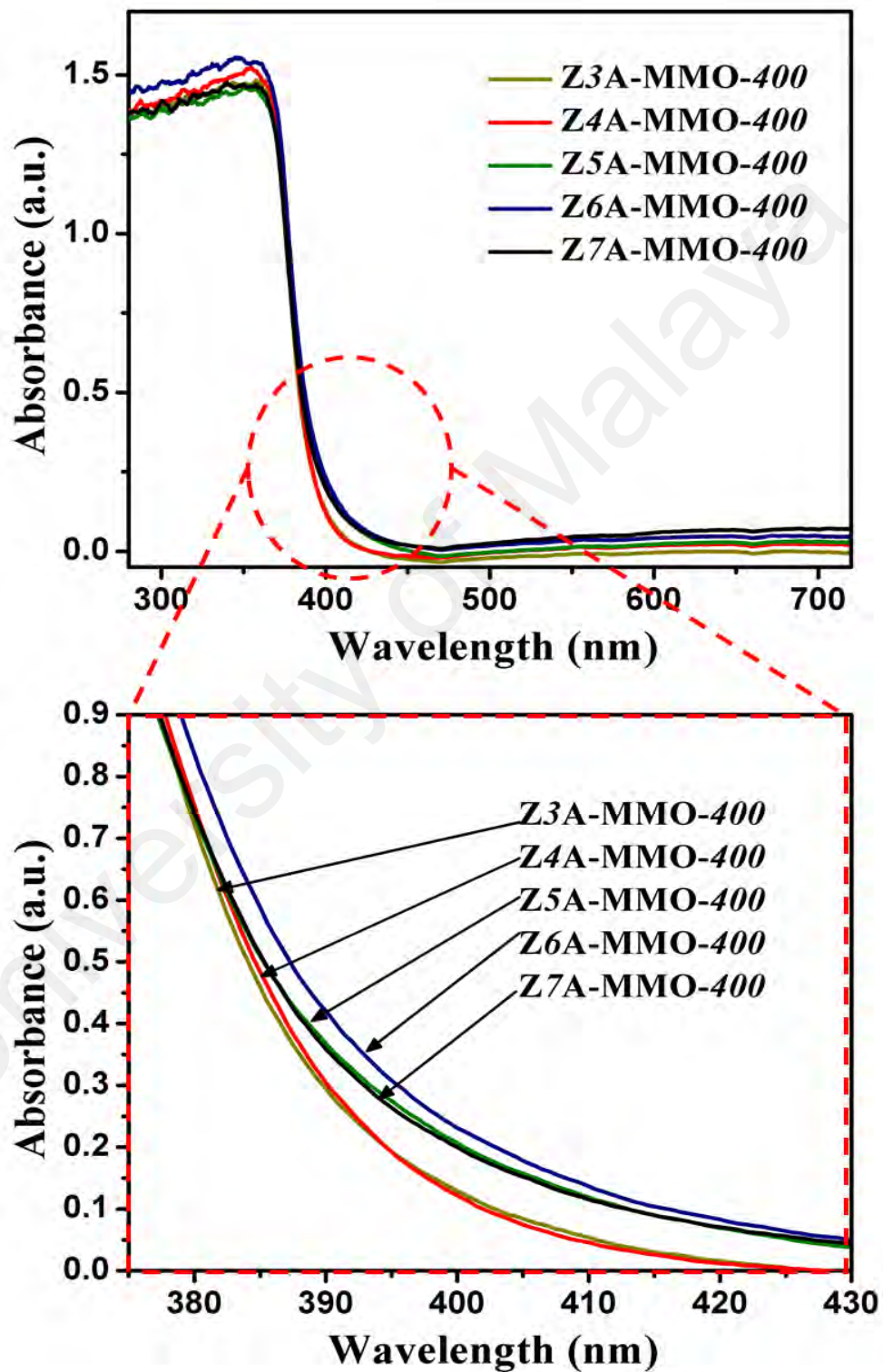


Figure 4.16: Absorbance spectra of ZrA-MMO-400 samples at different ratios ($r = 3, 4, 5, 6$ and 7).

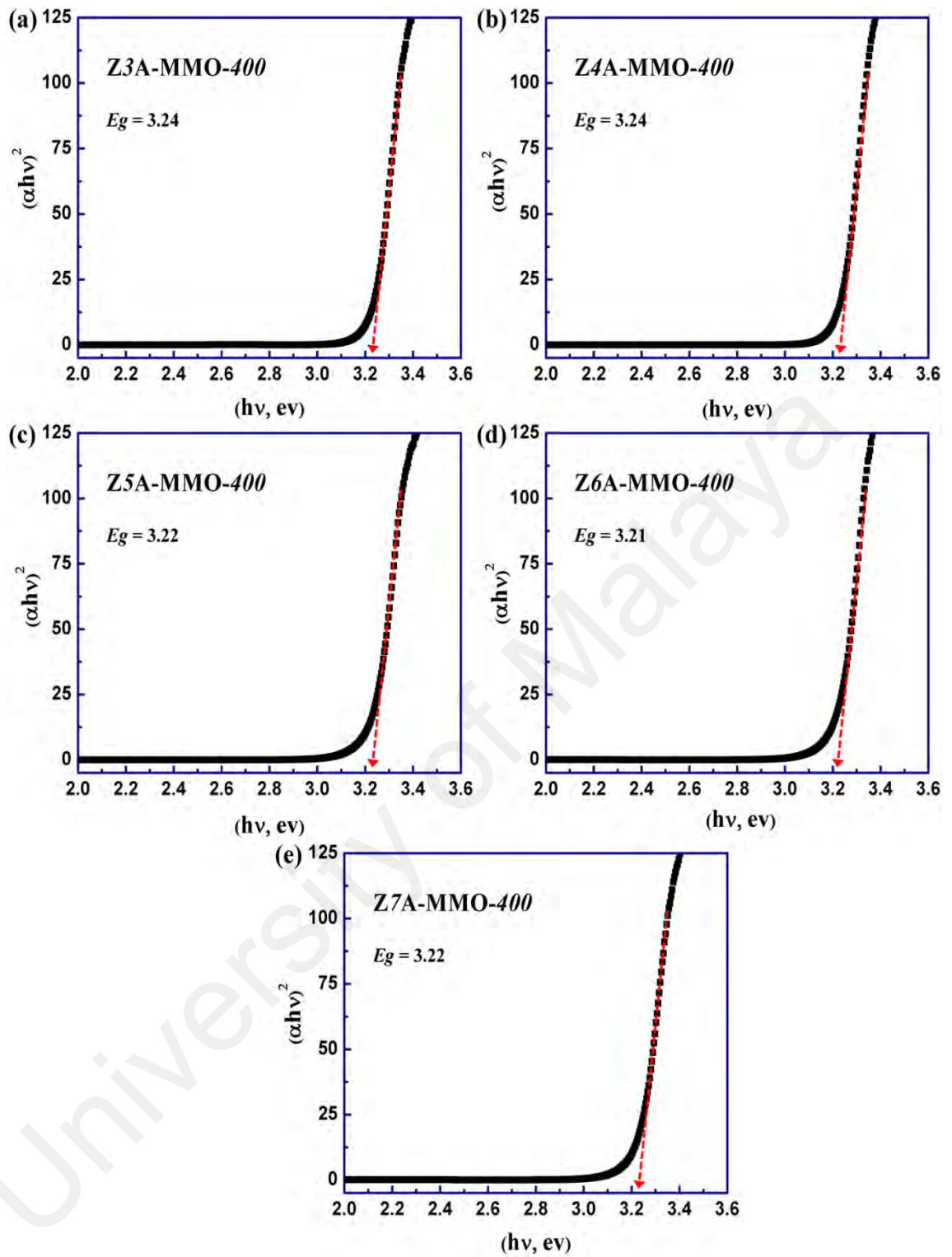


Figure 4.17: Optical band gap of ZrA-MMO-400 samples at different molar ratios; (a) Z3A-MMO-400, (b) Z4A-MMO-400, (c) Z5A-MMO-400, (d) Z6A-MMO-400 and (e) Z7A-MMO-400.

Figure 4.18 (a) shows a comparison plot of the optical properties between the absorbance spectra of pristine Z6A-LDH and thermally treated Z6A-MMO-400 samples. Basically, three main absorbance peaks were noticed in the pristine Z6A-LDH sample spectra which are mainly located at around 220, 290 and 370 nm. Specifically, peaks at 220 and 290 nm could be due to the presence of NO₃ in the interlayer of LDH (Ali Ahmed, Talib, *et al.*, 2012b; Chai *et al.*, 2009), whereas the peak at 370 nm is attributed to the direct transition between $2p$ orbital of oxygen and np and/or ns orbitals of metal (Zn of $n = 4$ and Al of $n = 3$). Furthermore, as aforementioned, thermal treatment of Zn/Al-LDH particles causes a collapse of the 2D layer structure with the formation of MMOs composed of ZnO phase and ZnAl₂O₄ spinel. This behavior was supported by the redshift in the optical spectra of Z6A-MMO-400 sample. Continuously, the optical band gap of pristine Z6A-LDH sample was calculated according to Equation 4.1. Whereas, pristine Z6A-LDH showed more than one energy band gap, which is due to the formation of several phases in the pristine Z6A-LDH. These energy band gaps were found to be 5.15, 3.78 and 3.2 eV as it can be seen in Figure 4.18 b, c and e, respectively. Energy band gaps around 5.15 and 3.78 eV can be ascribed to the existence of NO₃ groups in Z6A-LDH interlayer structure which in turn reflect the absorbance spectra findings (Ali Ahmed, Talib, *et al.*, 2012b). In the meanwhile, band gap around 3.2 eV could be attributed to ZnO formation during the synthesis of Z6A-LDH, as shown in the XRD patterns.

The findings in the current study, concerning the calculated band gap, are in a good agreement with previously published data concerning both thermal treatment temperature and molar ratio variations (Table 4.6) (Ahmed *et al.*, 2012a; Ali Ahmed, Talib, Hussein, *et al.*, 2012; L. Zhang *et al.*, 2014; X. Zhao *et al.*, 2012; X. Zhao *et al.*, 2010; Zhu *et al.*, 2017).

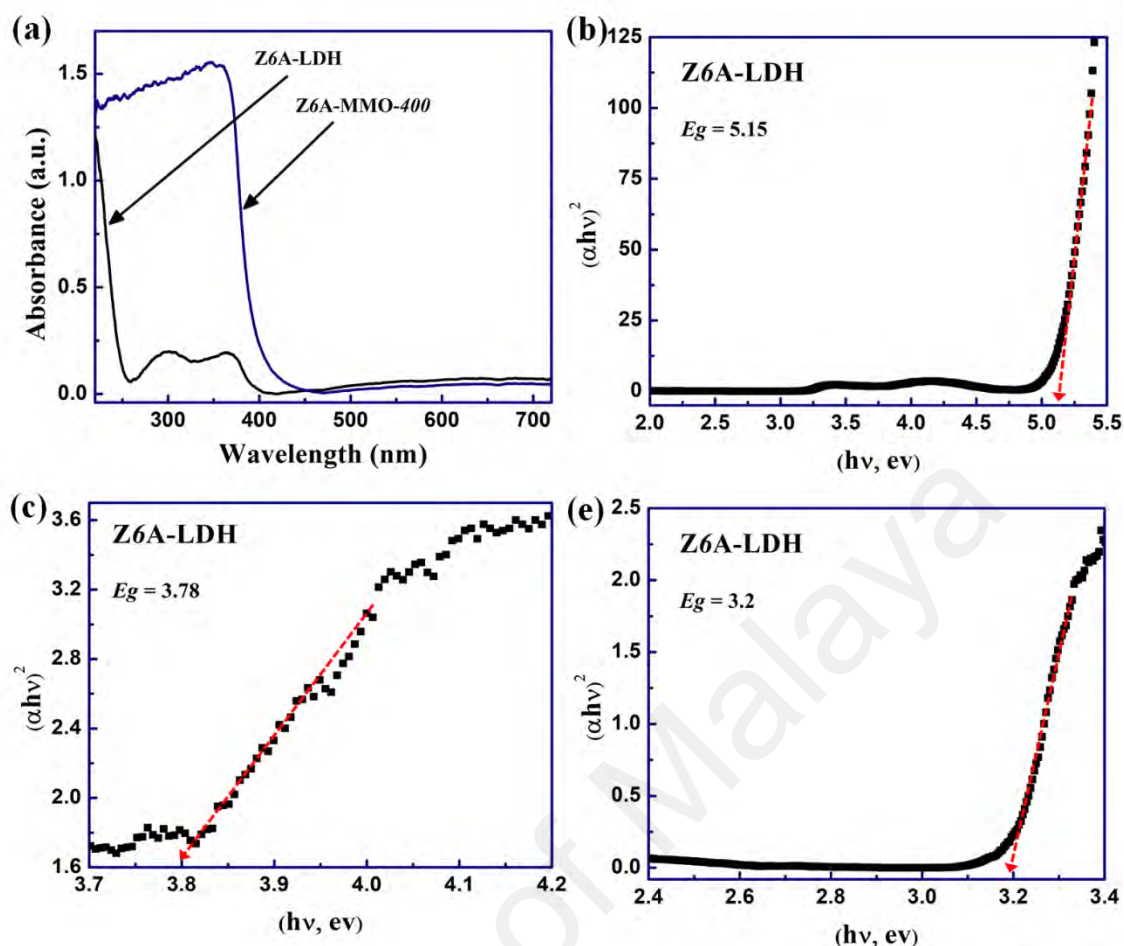


Figure 4.18: Optical properties of (a) absorbance of pristine Z6A-LDH and thermally treated Z6A-MMO-400 samples, (b) Z6A-LDH energy band gap no.1 (c) Z6A-LDH energy band gap no.2 and (d) Z6A-LDH energy band gap no.3.

Table 4.6: Comparison table to other researchers' outcomes.

<i>Sample</i>	<i>Band gap (eV)</i>	<i>Reference</i>
Pristine LDH	5.2 & 3.4	(Ahmed <i>et al.</i> , 2012b)
Z3A-MMO-500	3.13	(L. Zhang <i>et al.</i> , 2014)
Z4A-MMO-200	3.26	(Ahmed <i>et al.</i> , 2012a)
Z4A-MMO-400	3.25	(Ahmed <i>et al.</i> , 2012a)
Z6A-MMO-400	3.04	(Zhu <i>et al.</i> , 2017)

4.3.2 Photoluminescence spectroscopy

The steady-state photoluminescence (PL) measurement was performed to investigate the defect states of MMO anode materials and the role of thermal treatment temperature as well as the molar ratio on these defects alteration.

Figure 4.19 (a) displays normalized PL spectra of Z6A-MMO- T samples at different thermal treatment temperatures, where $T = 200, 300, 350, 400, 450$ and 500 °C. In this study, each individual PL spectra was normalized based on the NBE peak intensity of Z6A-MMO- T samples. Each PL emission spectra exhibited two distinct emissions, namely, the near band edge (NBE: ~ 380 nm) emission and in the visible region deep-level emission (DLE: 465–800 nm). Theoretically, NBE, in the UV region, is originated from the transition of a photogenerated electron from the conduction band to the valence band in MMO matrix ($\text{ZnO}/\text{ZnAl}_2\text{O}_4$), whereas DLE is related to the transition of an electron from the defect state (such as V_{zn} , Zn_i , V_{o} , and O_i) to the valence band in MMO matrix. Generally, a drastic quench in DLE spectrum intensity was noticed as the temperature increased which evidences the reduced surface defects originating from oxygen, Zn^{+2} and Al^{+3} vacancies (Abderrazek *et al.*, 2017; Nasr *et al.*, 2016). It is well-known that the ZnAl_2O_4 band gap is over 3.77 eV which was not found using the excitation source applied in the current study due to low laser power (X. Chen *et al.*, 2013). Therefore, the obtained PL spectra, especially in the NBE region, are mainly attributed to ZnO.

The ratio of intensities between NBE and DLE emissions ($I_{\text{NBE}}/I_{\text{DLE}}$) is considered as an indicator of crystal quality, and thus the larger ratio of $I_{\text{NBE}}/I_{\text{DLE}}$ indicates lower concentration of surface defects (Nasr *et al.*, 2016). It was observed that the $I_{\text{NBE}}/I_{\text{DLE}}$ ratio increased almost linearly with thermal treatment temperature increment from 200 to 400 °C (Figure 4.19, b). Subsequently, the $I_{\text{NBE}}/I_{\text{DLE}}$ ratio was decreased as the

temperature was further increased to 500 °C which could be due to higher formation of ZnAl_2O_4 spinel as well as densification and/or grain growth upon higher thermal treatment temperature. Increment in I_{NBE}/I_{DLE} ratio clearly indicates that both vacancies and interstitials oxygen defects are reduced at high thermal treatment temperatures. These results are in a good accordance with the XRD and UV-Vis analysis.

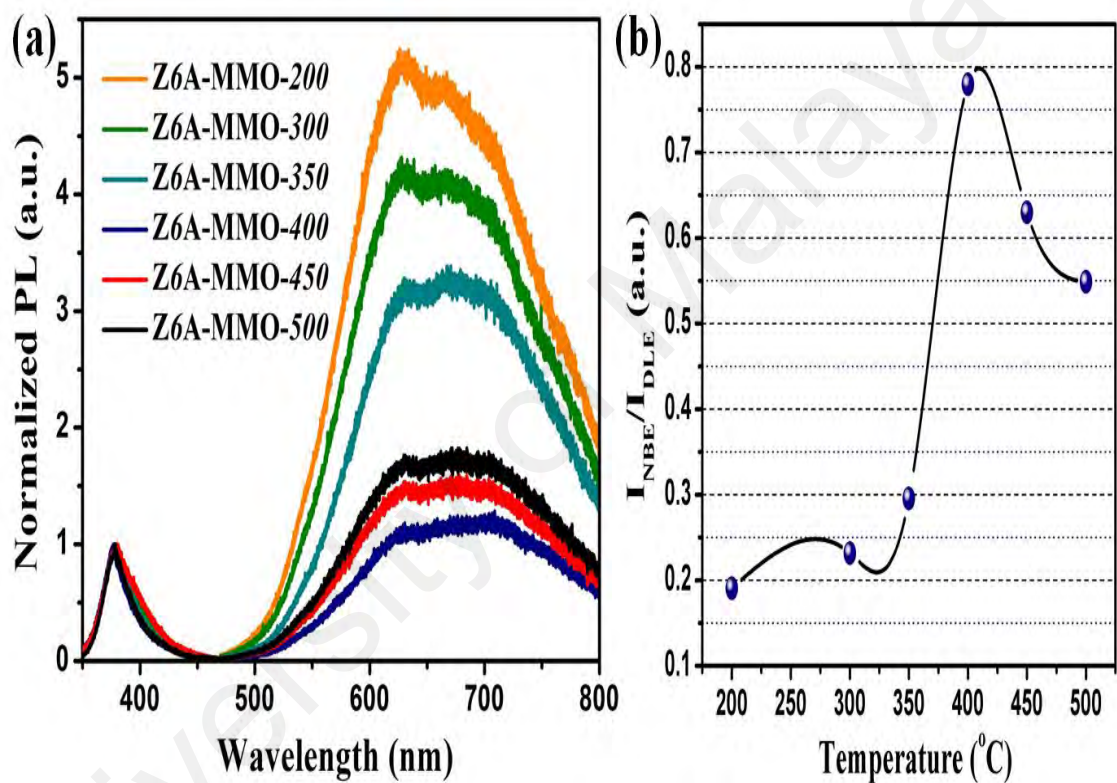


Figure 4.19: (a) Normalized PL spectra; and (b) I_{NBE}/I_{DLE} ratio of Z6A-MMO- T samples, where $T = 200, 300, 350, 400, 450$ and 500 °C.

The PL analysis was also employed to study the effect of molar ratio alteration on the defect states in the final MMO anode materials, where r represents the molar ratio of Zn^{+2} to Al^{+3} ($r = 3, 4, 5, 6$ and 7). Figure 4.20 (a) presents normalized PL spectra of the prepared ZrA- MMO-400 samples. Generally, increasing the molar ratio from 2 to 6 resulted in lower DLE peaks intensity which in turn indicates higher crystal quality of the prepared materials. Concurrently, further increase in the molar ratio ($r = 7$), led

to slightly higher defects which is in agreement with XRD and UV-vis analysis. Figure 4.20 (b) shows the I_{NBE}/I_{DLE} ratio which indicates lower concentration of surface defects as the molar ratio increases. This phenomenon may be due to higher concentration of $ZnAl_2O_4$ formation which resulted in higher number of defects on the surface of the prepared materials at low molar ratios. These results revealed that Zn^{2+} filled the defect site of the MMO crystal framework which in turn reduced the dislocation site of Al^{3+} . The Z6A-MMO-400 sample exhibited the highest ratio between the NBE to DLE region (Figure 4.20 (b)), showing that an optimum Zn dominated the crystalline nature in Z6A-MMO-400.

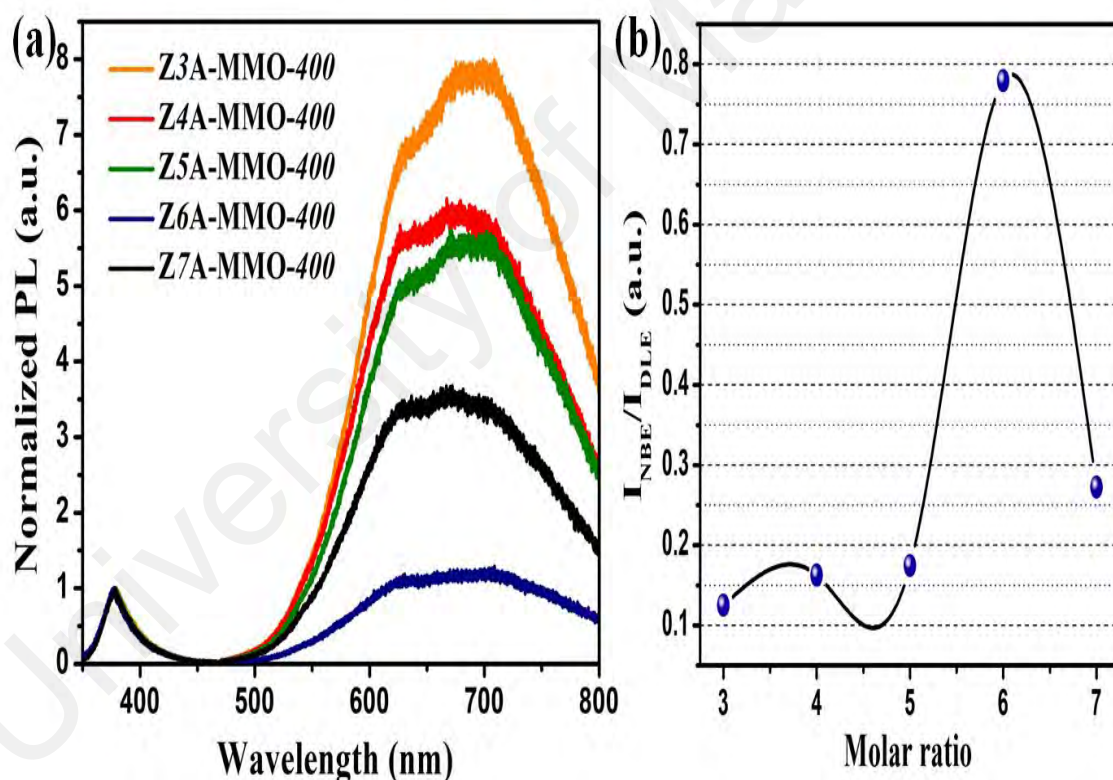


Figure 4.20: (a) Normalized PL spectra; and (b) I_{NBE}/I_{DLE} ratio of ZrA-MMO-400 samples, where $r = 3, 4, 5, 6$ and 7 .

Figure 4.21 illustrates normalized PL spectra of pristine Zn_6Al -LDH excited at 325 nm together with Z6A-MMO-400 samples based on the spectrum intensities in the NBE region. An ultraviolet emission around 380 nm was noticed originated from the NBE

emission. This spectrum is mainly due to free excitation recombination of ZnO. In the meanwhile, green emission was observed around 650 nm which is commonly attributed to the deep level emission originated from impurities, oxygen vacancies as well as structural defect states in the MMO matrix (Abderrazek *et al.*, 2017). Furthermore, the I_{NBE}/I_{DLE} ratio, which indicates the crystal quality, was also calculated. It was found that the I_{NBE}/I_{DLE} ratio of Zn6Al-LDH is lower than Z6A-MMO-400. This observation indicates a favorable formation of MMO matrix with low surface defects as compared to the pristine sample. Zn6Al-LDH demonstrated a value of 0.13 while I_{NBE}/I_{DLE} ratio was calculated to be 0.78 for Z6A-MMO-400 sample.

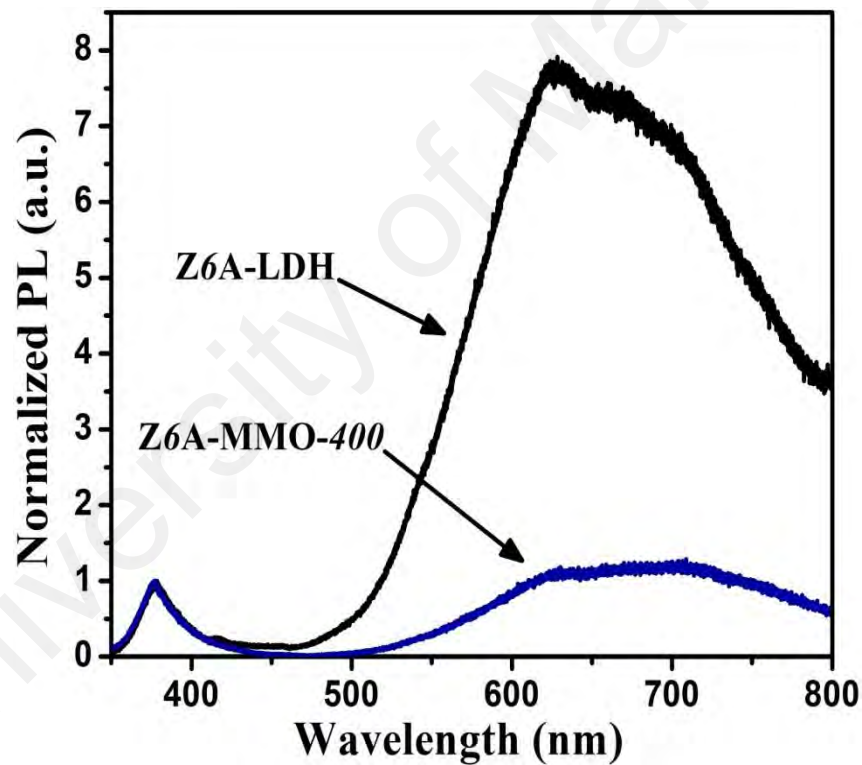


Figure 4.21: Normalized PL spectra of Z6A-LDH and Z6A-MMO-400 samples.

4.4 Dye-sensitized photodetector performance analysis

4.4.1 Spectral response of dye-sensitized photodetector

The general mechanism to demonstrate the photo-responsive behavior of MMO and dye N719 in the fabricated DS photodetector is shown in Figure 4.22, which reveals the illustrative schematic of both dark and illumination conditions. As shown in Figure 4.22 (a), the molecules of oxygen are adsorbed onto the prepared surface of MMO anode material during the dark condition because of the surface dangling bonds and subsequently free electrons from the MMO will be captured causing low dark conductivity, which can be expressed in equation 4.2: (Z. Wang *et al.*, 2011)



Continuously, in this study, Dye N719 was employed as sensitizer to alter the photo-generated electrons transfer pathway. Upon illumination by visible light, photons are captured by the dye molecules and subsequently an electron is injected in the MMO anode materials (Figure 4.22, b); this electron is excited by visible light from highest occupied molecular orbital (HOMO ~ -5.62 eV) towards the lowest unoccupied molecular orbital (LUMO ~ -3.9 eV) of N719 sensitizer after the absorption of low-frequency photons (Foruzin *et al.*, 2016), which is equivalent to a lower band in the visible light, in which these photons are subsequently injected in the conduction band (CB) of the MMO anode material (Figure 4.22, c). Simultaneously, the injected electrons are derived towards the collection electrode (FTO). Holes on the other side migrate from the valence band (VB) of MMO anode material to HOMO of N719 sensitizer. The value of dark current might increase, unavoidably, as the carriers travel between HOMO of N719 and CB of MMO.

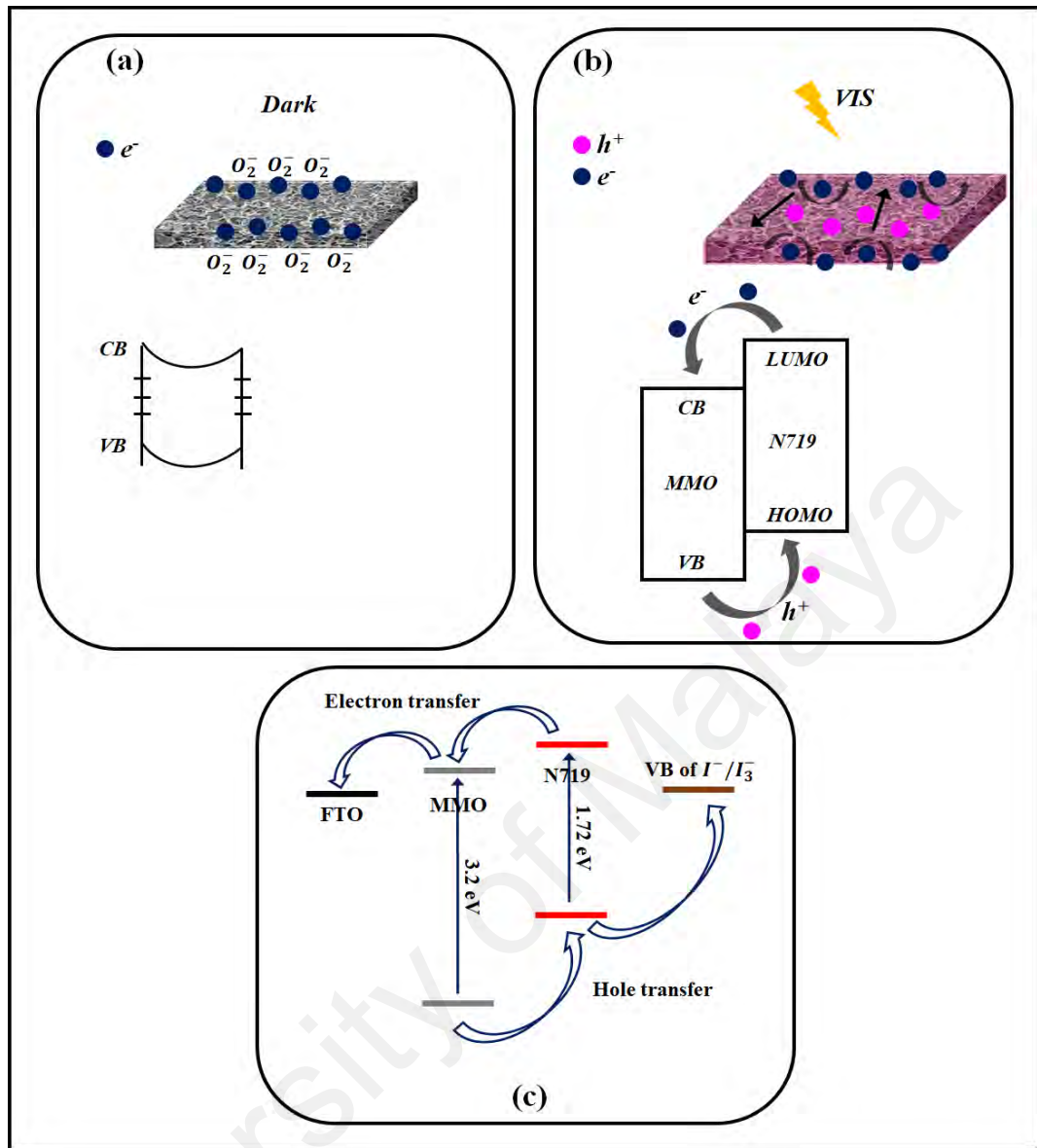


Figure 4.22: (a) Illustrative schematic of MMO anode material in dark condition, (b) Dye-sensitized mechanism and (c) proposed energy diagram of DS photodetector based on MMO and N719 sensitizer photoanode (Foruzin *et al.*, 2016).

Figure 4.23 (a) illustrates the absorption spectra of Z6A-MMO-400 sample alongside Z6A-MMO-400 containing dye N719 sensitizer. An observable wavelength cut off phenomenon of Z6A-MMO-400 materials at around 380 nm was noticed whereas the cut off wavelength of dye N719 concentrated in the range of 480-580 nm, mainly at 530 nm (Tao *et al.*, 2012). The latter absorption cut off is corresponded to the direct transition from HOMO to LUMO in dye N719. It can be clearly observed from Figure

4.23 (a) that dye N719 in the proposed geometry contributes an essential role to widening the absorption spectrum towards the visible light range.

The absorption spectra (from 350 to 720 nm) of Z6A-*MMO-T* and ZrA-*MMO-400* containing dye N719, which is adsorbed on the MMO layer (MMO + dye N719), are presented in Figure 4.23 (b) and (c), respectively. An observable cut off phenomenon of MMO anode materials around 380 nm was noticed for both thermal treatment temperature and molar ratio variations. In the meanwhile, another absorption peak was occurred at 530 nm which is mainly attributed to the sensitizer (N719) (Joly *et al.*, 2014). The latter absorption peak is corresponded to the direct transition from HOMO to LUMO in dye N719 (Figure 4.23 (d)) (Joly *et al.*, 2014). Continuously, the dye loading trend is also traceable from UV-Vis spectroscopy measurements. It was proven that the absorption spectra is proportional to the amount of dye loaded on the anode materials (Tao *et al.*, 2012; Yun *et al.*, 2010). As depicted in Figure 4.23 (d), the absorption spectra of five different dye N719 concentrations are demonstrated. Subsequently, a fitting curve was created based on the absorption λ max of different dye N719 concentrations (Figure 4.23 (e)). The resultant equation (Equation 4.3) was used to estimate the amount of dye N719 loaded on MMO anode materials. It was found that the sequence of the estimated loaded dye N719 is in accordance with BET surface area analysis where higher surface area facilitates higher amount of dye N719 loaded on the MMO layer.

$$y = 5.6254x - 0.6192 \quad (4.3)$$

where y represents the maximum absorbance at 530 nm and x is the estimated amount of dye loaded onto MMO layer.

In the variation of thermal treatment temperature, using Equation 4.3, it was found that the loaded amount of dye N719 increased when the temperature increased from 200 to 400 °C before being further decreased when the temperature increased to 500 °C. Based on the absorption λ max shown in Figure 4.23 (e) and Equation 4.3, the estimated amount of dye N719 on each layer of the prepared Z6A-*MMO-T* anode materials (Table 4.7) was found to be in the range of 2.5×10^{-4} to 3.3×10^{-4} mol/cm² for thermal treatment temperature of 200 to 400 °C, respectively. This phenomenon was expected as the sample treated at low temperature (200 °C) is rough and porous; however, impurities on the layer is high which in turn block the loading of dye N719 molecules. Further increase of temperature to 400 °C, the organic species are consumed and MMO anode materials are expected to have higher dye loading due to higher surface area and better porous quality. MMO anode materials which were treated at higher temperature (above 400 °C) exhibited more compact surface morphology with less porosity and lower surface area which results in lower dye loading amount (Al-Kahlout, 2015).

In the variation of molar ratio, it was noticed that increasing the molar ratio resulted in higher dye loading amount (Table 4.7 and Figure 4.23 (c)). This observation was noticed as the molar ratio increased from 3 to 6 (Z3A and Z6A-*MMO-400*), however, further increase in the molar ratio (Z7A-*MMO-400*) resulted in lower dye loading which can be due to compact surface morphology as shown in the FESEM analysis. Z3A-*MMO-400* exhibited 2.6×10^{-4} mol/cm² dye loaded on its surface, while Z6A-*MMO-400* showed value of 3.3×10^{-4} mol/cm²; in the meanwhile, Z7A-*MMO-400* demonstrated a value of 3.2×10^{-4} mol/cm². The dye loading sequence was expected from section 4.2 (FESEM and BET analysis).

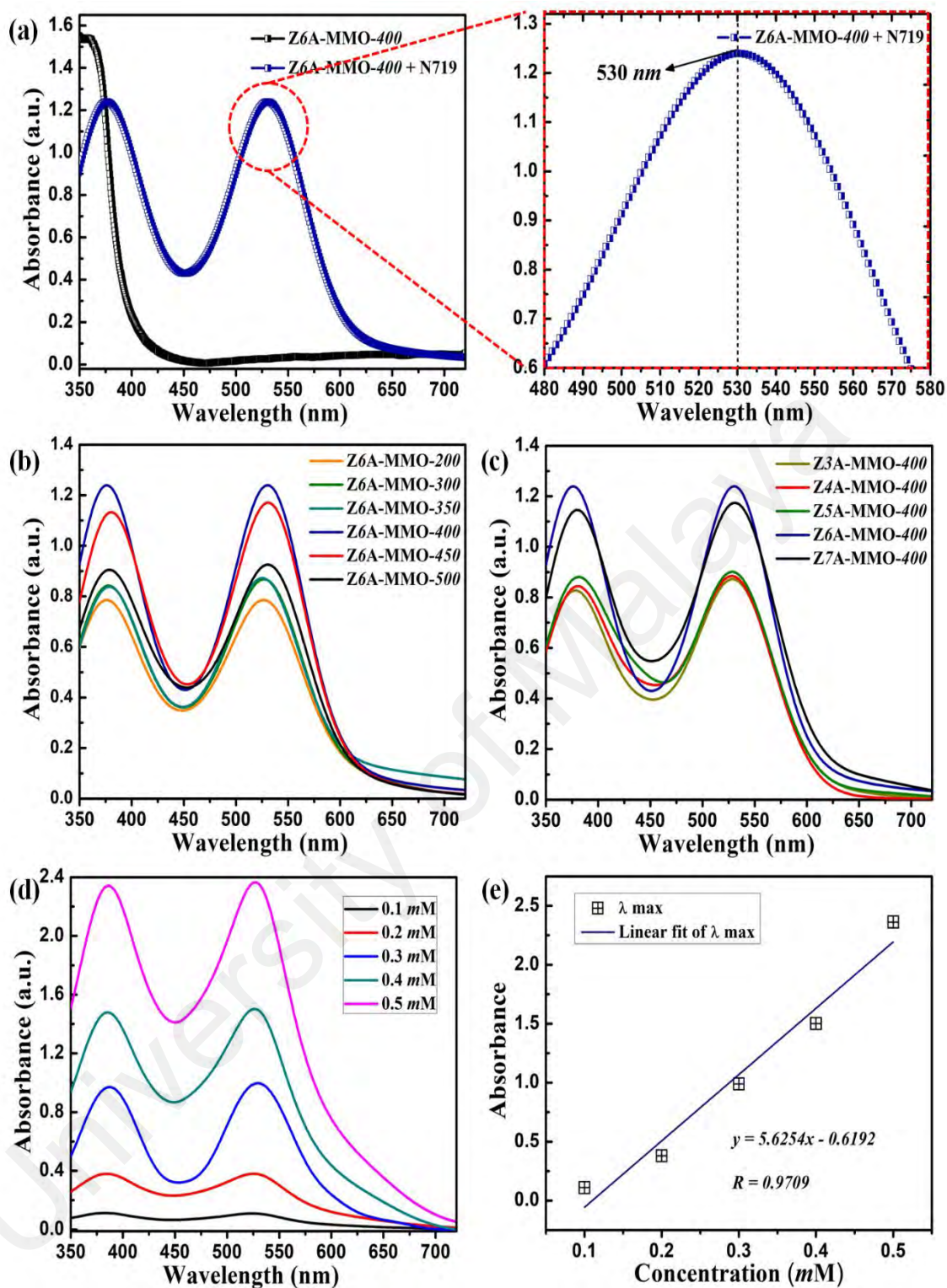


Figure 4.23: (a) Spectral response of Z6A-MMO-400 and Z6A-MMO-400 containing dye N719, (b) Z6A-MMO-T+ Dye N719, (c) ZrA-MMO-400 + Dye N719, (d) absorbance spectra of dye N719 at different concentrations; and (e) linear fit of absorption λ max of dye N719 at 525 nm.

Table 4.7: Amount of dye N719 loaded on MMO anode material layers.

Samples	Amount of dye	Samples	Amount of dye
Z6A-MMO-T	(mol/cm²)	ZrA-MMO-400	(mol/cm²)
Z6A-MMO-200	2.5 x 10 ⁻⁴	Z3A-MMO-400	2.6 x 10 ⁻⁴
Z6A-MMO-300	2.6 x 10 ⁻⁴	Z4A-MMO-400	2.7 x 10 ⁻⁴
Z6A-MMO-350	2.7 x 10 ⁻⁴	Z5A-MMO-400	2.7 x 10 ⁻⁴
Z6A-MMO-400	3.3 x 10 ⁻⁴	Z6A-MMO-400	3.3 x 10 ⁻⁴
Z6A-MMO-450	3.2 x 10 ⁻⁴	Z7A-MMO-400	3.2 x 10 ⁻⁴
Z6A-MMO-500	2.7 x 10 ⁻⁴	-	-

4.4.2 Illumination power dependence of dye-sensitized photodetector

The correlation between the photocurrent and various illumination power intensities under zero and 0.2 V bias measurements of the fabricated Z6A-MMO-T DS photodetectors is shown in Figure 4.24 (a and b) and Table 4.8, where $T = 200, 300, 350, 400, 450$ and 500 °C. It was observed from Figure 4.24 and Table 4.8 that the correlation between photocurrent and illumination power intensity is almost linear for both bias voltages. Notably, the amount of generated photocurrent increased monotonically with the increment of the illumination power operated from 0 to 100 mW/cm². The bias voltage increment also showed increase in the pronounced photocurrent magnitude. This phenomenon is attributed to the increment in the number of photo-excited electrons of sensitizer (N719) at higher illumination power which subsequently increases the number of electrons through CB in MMO anode materials. It can also be observed that, generally, higher thermal treatment temperature resulted in higher amount of photocurrent magnitude. In details, the magnitude of generated photocurrent at zero bias for Z6A-MMO-200 DS photodetector was found to be 1.4×10^{-7} and 1.3×10^{-4} A at illumination power of 0 mW/cm² and 100 mW/cm², respectively. Continuously, at 0.2 V bias voltage, Z6A-MMO-200 DS photodetector showed an increment in the magnitude of the photocurrent, whereas values of 8.9×10^{-6}

and 1.5×10^{-4} A were obtained at 0 mW/cm^2 and 100 mW/cm^2 illumination powers, respectively. Z6A-MMO-300 and Z6A-MMO-350 DS photodetectors exhibited higher photocurrent magnitude at both zero and 0.2 V bias voltages for the pronounced illumination powers. In the meanwhile, it can be noticed that the photocurrent in Z6A-MMO-400 is high as compared to other DS photodetectors, which indicates that the optimum temperature of MMO anode materials can give rise to the pronounced photocurrent magnitude. The magnitude of photocurrent generated from Z6A-MMO-400 DS photodetector at zero bias was increased from 1.4×10^{-6} to 6.5×10^{-4} A at illumination power of 0 mW/cm^2 and 100 mW/cm^2 , respectively. In the meanwhile, at 0.2 V bias voltage, the photocurrent magnitudes of Z6A-MMO-400 DS photodetector were found to be 1.3×10^{-5} and 7.2×10^{-4} A at 0 mW/cm^2 and 100 mW/cm^2 , respectively. Evidently, it can be clearly observed that thermal treatment temperatures above $400 \text{ }^\circ\text{C}$ resulted in lower photocurrent magnitude, regardless of illumination powers and/or bias voltages variation. This finding clearly suggests that higher dye loading is more effective than other factors such as crystallinity and the optical band gap of the prepared Z6A-MMO-*T* anode materials. Whereby, DS photodetectors fabricated using MMO anode materials that thermally treated at temperatures higher than $400 \text{ }^\circ\text{C}$ (Z6A-MMO-450 and Z6A-MMO-500) revealed slightly lower energy band gap and higher crystallinity than Z6A-MMO-400 anode material, however, higher surface area and bigger porous morphology are also required for higher dye loading which in turn results in higher number of electrons to be injected in the MMO anode conduction band (Al-Kahlout, 2015).

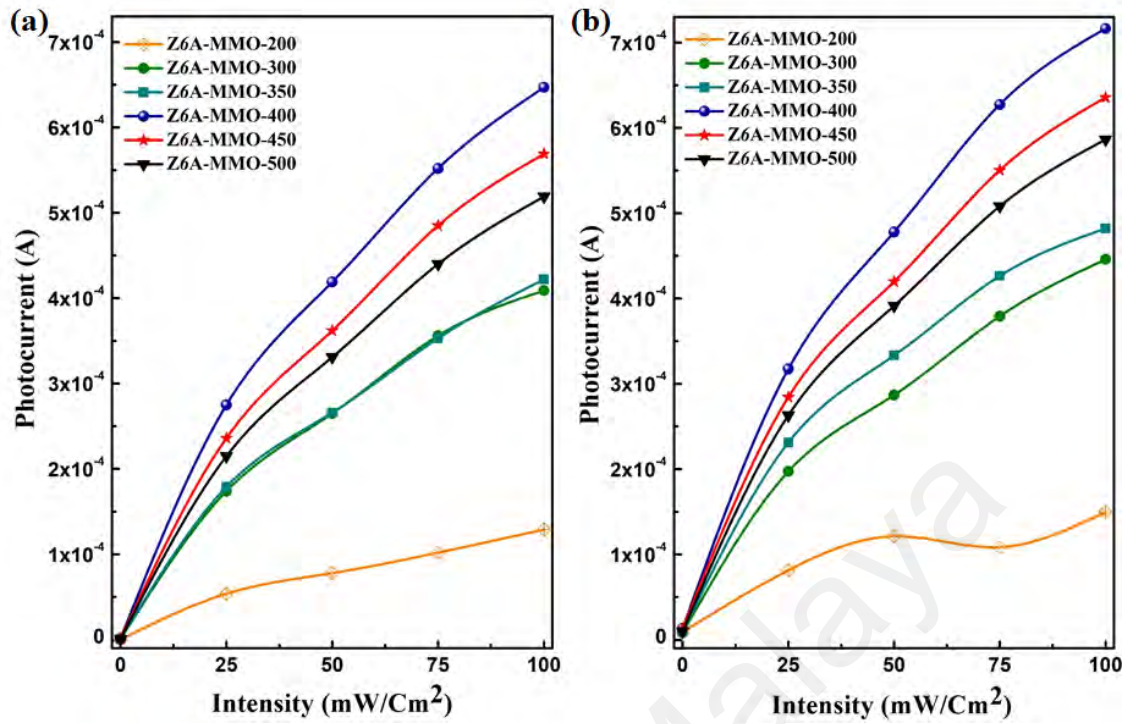


Figure 4.24: Photocurrent vs. illumination power for Z6A-MMO-*T* DS photodetectors; (a) zero and (b) 0.2 V bias voltages.

Table 4.8: Photocurrent magnitude, in mA, for Z6A-MMO-*T* DS photodetectors at different illumination power intensities.

Sample	Illumination power intensity (mW/cm^2)				
	0	25	50	75	100
Zero bias voltage condition					
Z6A-MMO-200	1.41×10^{-7}	5.39×10^{-5}	7.81×10^{-5}	1.02×10^{-4}	1.29×10^{-4}
Z6A-MMO-300	6.84×10^{-7}	1.74×10^{-4}	2.65×10^{-4}	3.56×10^{-4}	4.09×10^{-4}
Z6A-MMO-350	7.89×10^{-7}	1.79×10^{-4}	2.66×10^{-4}	3.53×10^{-4}	4.22×10^{-4}
Z6A-MMO-400	1.39×10^{-6}	2.75×10^{-4}	4.19×10^{-4}	5.52×10^{-4}	6.47×10^{-4}
Z6A-MMO-450	1.15×10^{-6}	2.36×10^{-4}	3.62×10^{-4}	4.85×10^{-4}	5.69×10^{-4}
Z6A-MMO-500	8.17×10^{-7}	2.15×10^{-4}	3.31×10^{-4}	4.40×10^{-4}	5.19×10^{-4}
0.2 bias voltage condition					
Z6A-MMO-200	8.99×10^{-6}	8.15×10^{-5}	1.21×10^{-4}	1.09×10^{-4}	1.50×10^{-4}
Z6A-MMO-300	9.23×10^{-6}	2.31×10^{-4}	3.33×10^{-4}	4.27×10^{-4}	4.82×10^{-4}
Z6A-MMO-350	1.32×10^{-5}	3.17×10^{-4}	4.78×10^{-4}	6.27×10^{-4}	7.16×10^{-4}
Z6A-MMO-400	1.30×10^{-5}	2.84×10^{-4}	4.20×10^{-4}	5.50×10^{-4}	6.36×10^{-4}
Z6A-MMO-450	9.86×10^{-6}	2.63×10^{-4}	3.91×10^{-4}	5.08×10^{-4}	5.86×10^{-4}
Z6A-MMO-500	8.99×10^{-6}	8.15×10^{-5}	1.21×10^{-4}	1.09×10^{-4}	1.50×10^{-4}

The photo-responsive parameters of the fabricated DS photodetector, namely, photo-responsivity (R), photo-conductivity (S), photo-detectivity (D*) and the effective quantum efficiency (EQE) were further studied and analyzed. The photo-responsivity, photo-conductivity, photo-detectivity and effective quantum efficiency at different thermal treatment temperatures as function of the illumination power are demonstrated in Figure 4.25 (a, b, c and d, respectively). These values were calculated according to Equations 2.7, 2.8, 2.10 and 2.11, respectively; at 0 bias voltage expect photo-conductivity values which were calculated at 0.2 V bias voltage. In general inspection, almost a linear decrease in the photo-responsive parameters was acquired as the illumination power increased from 25 to 100 mW/cm². This observation was noticed together with an increase in the photo-responsive parameters as, generally, the thermal treatment temperature increased. In the photo-responsivity observation, among all devices, Z6A-MMO-400 DS photodetector exhibited the highest photo-responsivity which was found to be 1.1×10^{-2} A/W at 25 mW/cm². On the contrary, Z6A-MMO-200 DS photodetector demonstrated value as low as 2.2×10^{-3} A/W at 25 mW/cm². A value of 8.5×10^{-7} Sm/W photo-conductivity for Z6A-MMO-200 sample was obtained; however, Z6A-MMO-400 demonstrated higher value of 3.3×10^{-6} Sm/W at illumination power of 25 mW/cm². In the photo-detectivity inspection, Z6A-MMO-500 recorded the highest value among all the samples (1.7×10^{10} Jones) whereas photo-detectivity value of Z6A-MMO-200 was found to be 1×10^{10} Jones at 25 mW/cm² illumination power. The photo-responsive parameters values were found to be lower at higher illumination intensity. The effective quantum efficiency showed a value of 2.6 % for Z6A-MMO-400 DS photodetector whilst a value of 5×10^{-1} % was obtained for Z6A-MMO-200 sample using illumination power of 25 mW/cm². In general, among all fabricated DS photodetectors, Z6A-MMO-400 exhibited the highest photo-responsive values while Z6A-MMO-200 demonstrated the lowest. DS photodetectors with thermal temperature

higher than 200 or 400 °C resulted in photo-responsive values between the demonstrated two thermal treatment temperatures. This phenomenon is in a good agreement with the anode materials characterizations findings whereas higher surface area delivers higher dye loading in the fabricated photoanode.

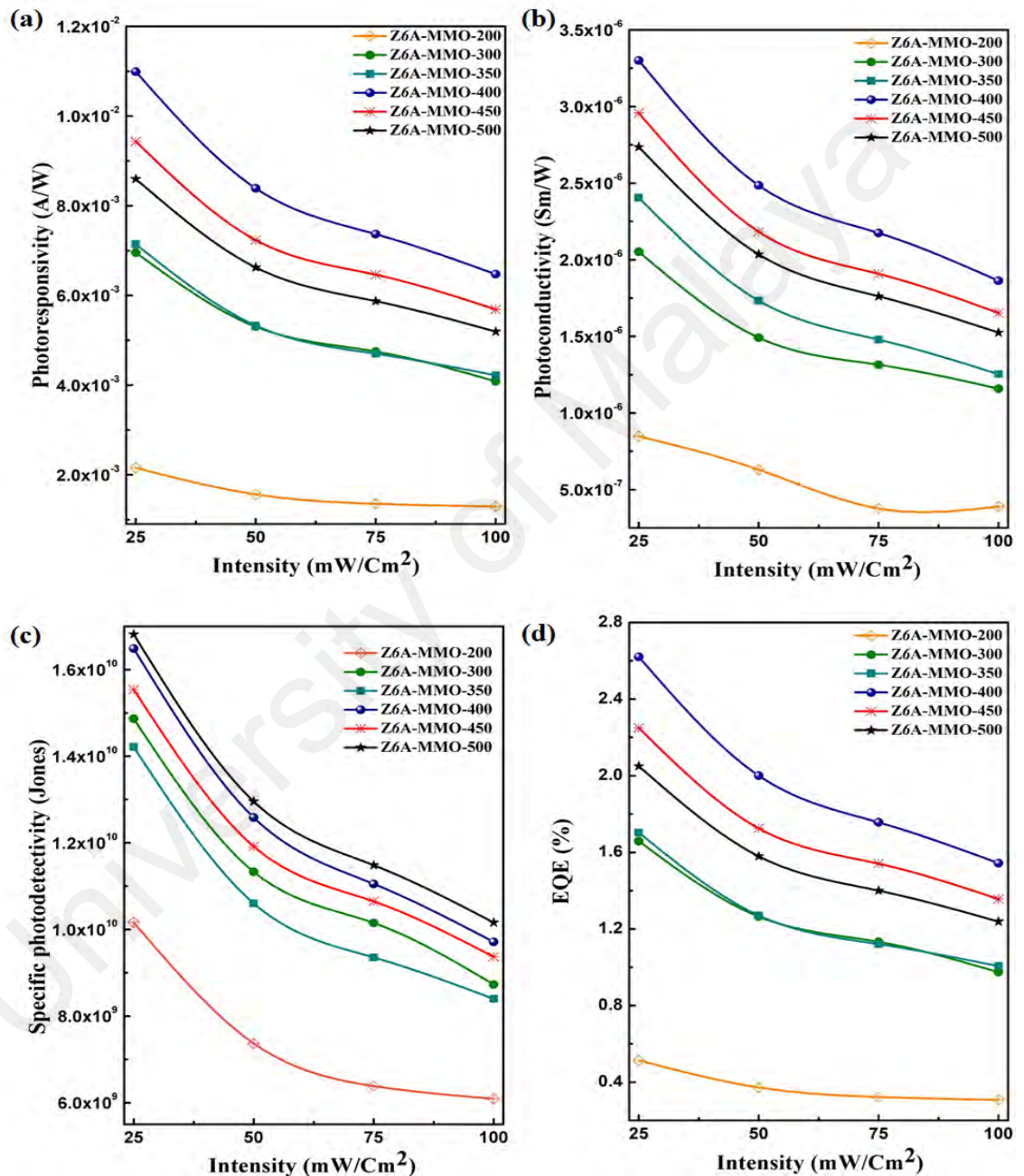


Figure 4.25: Illumination power dependence of photo-responsive behavior of Z6A-MMO-T DS photodetectors: (a) photo-responsivity, (b) photo-conductivity at 0.2 V bias voltage, (c) photo-detectivity and (d) effective quantum efficiency.

The effect of molar ratio on the correlation between the generated photocurrent and different illumination power intensity under zero and 0.2 V bias measurement of the fabricated *ZrA-MMO-400* DS photodetectors are illustrated in Figure 4.26 (a and b, respectively), where r represents the molar ratio of Zn^{+2} to Al^{+3} (3, 4, 5, 6 and 7). In the meanwhile, the raw data are presented in Table 4.9, for both zero and 0.2 bias voltage at different illumination power. Generally, the magnitude of generated photocurrent was increased as the illumination power increased due to an increase in the number of the excited electrons in the HOMO towards LUMO in N719 and subsequently higher number of electrons in the CB of MMO anode materials. Continuously, an increase in the molar ratio from 3 to 6 resulted in higher magnitude of generated photocurrent before being further decreased when the molar ratio increased to 7. This behavior could be explained by the observation that the dye N719 amount that was loaded on the *Z7A-MMO-400* anode material is relatively lower than the loaded dye N719 on the *Z6A-MMO-400* anode material which in turn resulted in lower amount of photo-generated current in *Z7A-MMO-400* DS photodetector. In particular, at zero bias voltage, DS photodetector *Z3A-MMO-400* exhibited photocurrent magnitude of 1.3×10^{-7} and 7.2×10^{-5} A at 0 mW/cm^2 and 100 mW/cm^2 illumination powers, respectively. Whereas at 0.2 bias voltage, values of 5.8×10^{-6} and 8.8×10^{-5} A were obtained at 0 mW/cm^2 and 100 mW/cm^2 illumination powers for the mentioned device. Furthermore, increasing the molar ratio to 4 or 5 (*Z4A* and *Z5A-MMO-400*) resulted in slightly higher amount of the photocurrent magnitudes. Among all the fabricated DS photodetectors, *Z6A-MMO-400* demonstrated the highest values of photocurrent magnitude. It is also worth mentioning that values of generated photocurrent in *Z6A-MMO-400* DS photodetector were increased when illumination power as well as the applied bias voltage increased. However, as mentioned above, the magnitude of generated photocurrent was decreased at molar ratio of 7, whereas *Z7A-MMO-400* DS photodetector demonstrated values of

3.8×10^{-4} and 4.2×10^{-4} A at zero and 0.2 V bias voltages, respectively, with illumination power of 100 mW/cm^2 . The decrease phenomenon is attributed to the properties of the prepared Z7A-*MMO-400* anode material were lower surface area and higher band gap could result in lower dye loading and longer electron path way, respectively.

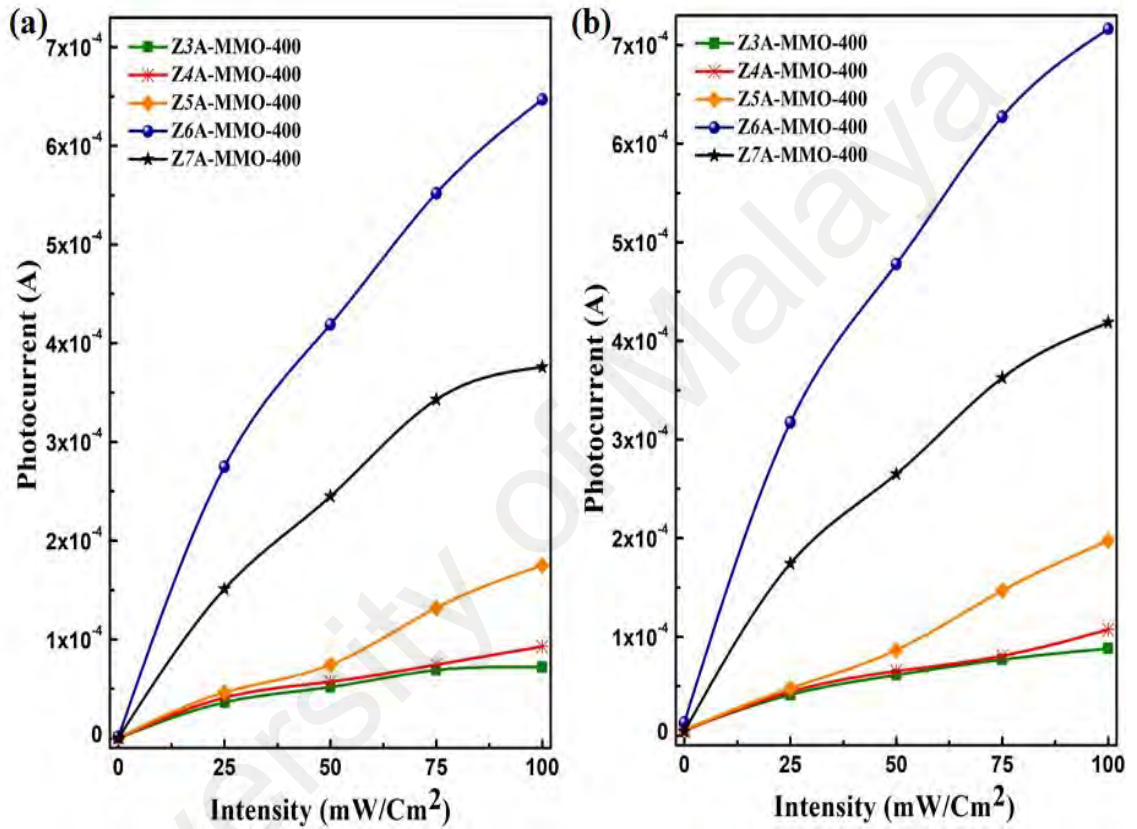


Figure 4.26: Photocurrent vs. illumination power for ZrA-*MMO-400* DS photodetectors; (a) zero and (b) 0.2 V bias voltages.

Table 4.9: Photocurrent magnitude, in mA, for ZrA-MMO-400 DS photodetectors at different illumination power intensities.

Sample	Illumination power intensity (mW/cm ²)				
	0	25	50	75	100
Zero bias voltage condition					
Z3A-MMO-400	1.30×10^{-7}	3.63×10^{-5}	5.18×10^{-5}	6.89×10^{-5}	7.20×10^{-5}
Z4A-MMO-400	2.38×10^{-7}	4.10×10^{-5}	5.72×10^{-5}	7.44×10^{-5}	9.28×10^{-5}
Z5A-MMO-400	2.94×10^{-7}	4.63×10^{-5}	7.43×10^{-5}	1.32×10^{-4}	1.75×10^{-4}
Z6A-MMO-400	1.39×10^{-6}	2.75×10^{-4}	4.19×10^{-4}	5.52×10^{-4}	6.47×10^{-4}
Z7A-MMO-400	3.08×10^{-7}	1.51×10^{-4}	2.45×10^{-4}	3.43×10^{-4}	3.76×10^{-4}
0.2 bias voltage condition					
Z3A-MMO-400	5.79×10^{-6}	4.13×10^{-5}	6.14×10^{-5}	7.69×10^{-5}	8.82×10^{-5}
Z4A-MMO-400	4.81×10^{-6}	4.43×10^{-5}	6.52×10^{-5}	8.07×10^{-5}	1.07×10^{-4}
Z5A-MMO-400	5.79×10^{-6}	4.78×10^{-5}	8.66×10^{-5}	1.47×10^{-4}	1.97×10^{-4}
Z6A-MMO-400	1.32×10^{-5}	3.17×10^{-4}	4.78×10^{-4}	6.27×10^{-4}	7.16×10^{-4}
Z7A-MMO-400	4.06×10^{-6}	1.74×10^{-4}	2.65×10^{-4}	3.63×10^{-4}	4.19×10^{-4}

The effect of molar ratio on photo-responsive parameters are demonstrated in Figure 4.27 (a, b, c and d) as a function of illumination power. Generally, a decrease in the photo-responsive parameters was observed as the illumination power increased from 25 to 100 mW/cm², whereas increased photo-responsive behavior was noticed with the molar ratio increment. Increasing the molar ratio from 3 to 6 resulted in higher photo-responsivity, photo-conductivity, photo-detectivity and effective quantum efficiency. However, further increasing in molar ratio resulted in lower photo-responsive values. DS photodetector Z3A-MMO-400 demonstrated values of 1.5×10^{-3} A/W, 4.3×10^{-7} Sm/W, $7.1 \times 10^{+9}$ jones and 3.5×10^{-1} of photo-responsivity, photo-conductivity, photo-detectivity and effective quantum efficiency, respectively, at illumination power of 25 mW/cm². These values were increased notably when the molar ratio increased to 6, photo-responsivity, photo-conductivity, photo-detectivity and effective quantum efficiency of 1.1×10^{-2} A/W, 3.3×10^{-6} Sm/W, $1.6 \times 10^{+10}$ jones and 2.6, respectively, at

illumination power of 25 mW/cm^2 . Continuously, as the molar ratio increased to 7, the photo-responsive parameters decreased to $6 \times 10^{-3} \text{ A/W}$, $1.8 \times 10^{-6} \text{ Sm/W}$ and 1.45. As aforementioned, this phenomenon is attributed to the low surface area by which lower dye loading was acquired which in turn demonstrates low number of electrons to be injected in the CB of the MMO anode material as compared with molar ratio 6. However, photo-detectivity of Z7A-MMO-400 DS photodetector exhibited higher value than Z6A-MMO-400 due to low dark current value ($3.9 \times 10^{-7} \text{ A}$) which affects the photo-conductivity value positively (according to equation 2.10).

The photocurrent behavior of all fabricated DS photodetectors, regardless of the thermal treatment temperature and molar ratio variations, was consistent with those of XRD, FESEM, UV-Vis and BET results analysis which confirms that higher crystallinity, mesoporous morphology, surface area and lower energy band gap and defect states exhibited shorter electron path ways and higher dye loading. In similar geometry, the proposed DS photodetectors exhibited comparable photocurrent and photo-responsive parameter values as compared to other research findings (Y. Lee *et al.*, 2015; Neto *et al.*, 2017; Parreira *et al.*, 2012; Qadir *et al.*, 2014; Qadir *et al.*, 2015; Z. Wang *et al.*, 2011).

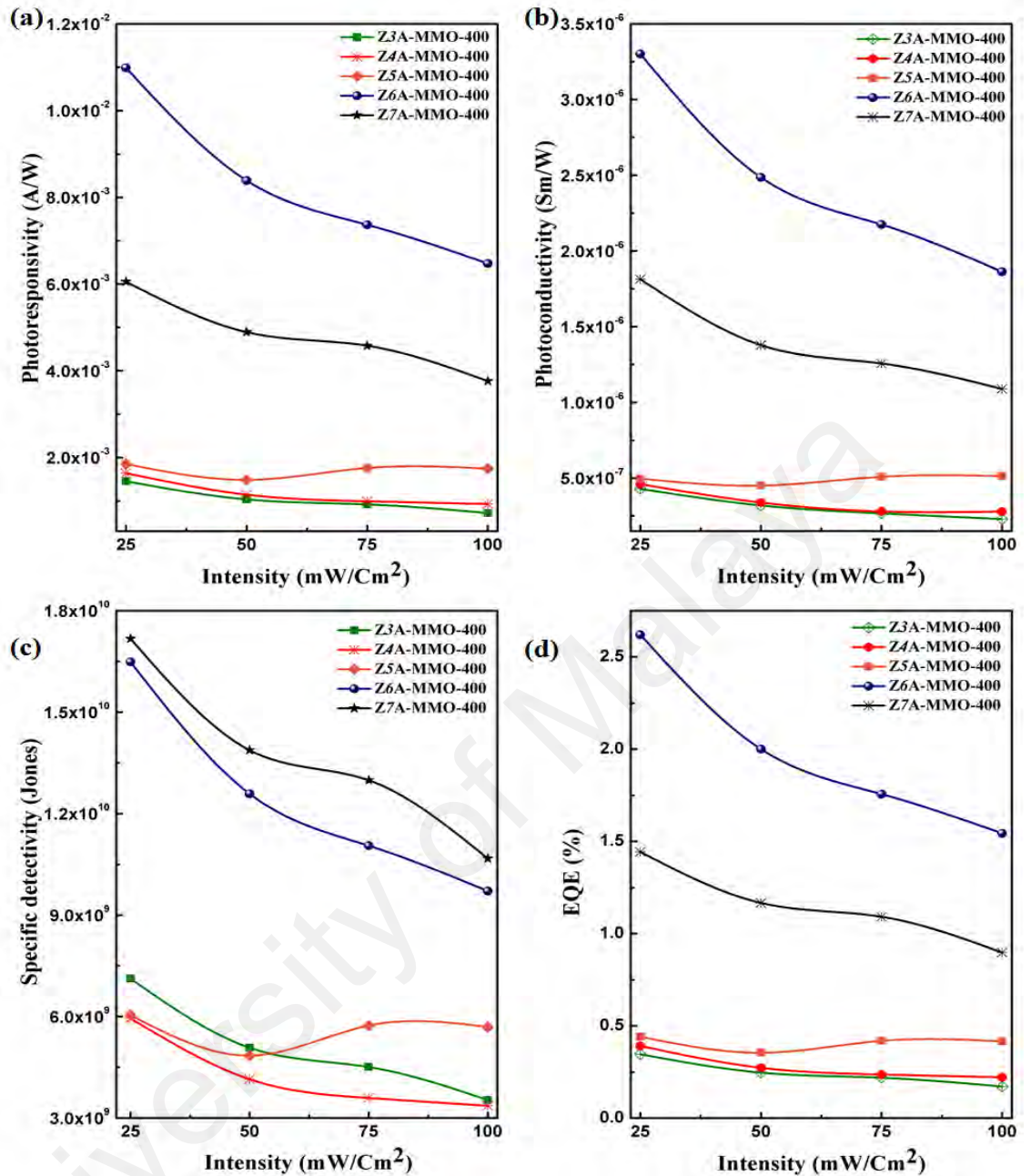


Figure 4.27: Illumination power dependence of photo-responsive behavior of ZrA-MMO-400 DS photodetectors: (a) photo-responsivity, (b) photo-conductivity at 0.2 V bias voltage (c) photo-detectivity and (d) effective quantum efficiency.

Figure 4.28 shows a logarithmic scale of the photo-responsivity and effective quantum efficiency as a function of illumination power for Z6A-MMO-400 DS photodetector, inset is the magnitude of photocurrent. The proposed photodetector, in conclusion, exhibited a photo-responsivity and EQE of 1.1×10^{-2} A/W and 2.6, respectively, under 25 mW/cm^2 , which is the lowest power limit in our experimental setup. Theoretically, the photo-responsivity increases as the intensity of illumination

power decreases until it reaches saturation value as the relation between photo-responsivity and illumination power intensity is inversely proportional (i.e., $R \propto P^{-1}$, Equation 2.7) (S. H. Yu *et al.*, 2014). Based on this thesis' findings, the photo-responsivity is expected to increase at lower illumination power values. For example, if the dark current (1.4×10^{-6}) was obtained at illumination power of 10^{-6} W/cm², the photo-responsivity would be 1.4 A/W. The EQE value, therefore, would also increase as the photo-responsivity increases until it reaches a value of 333.2 % in accordance with equation 2.11.

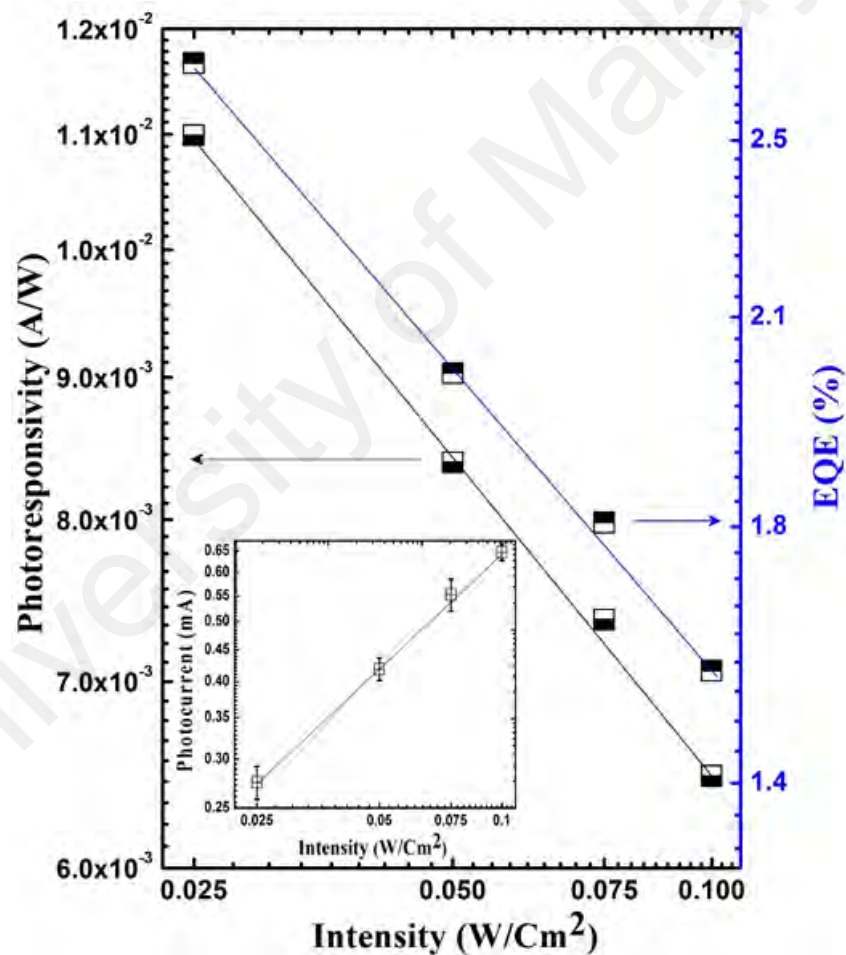


Figure 4.28: Logarithmic scale of photo-responsivity and effective quantum efficiency as a function of illumination power for Z6A-MMO-400 DS photodetector.

4.4.3 Spatial and Temporal Response Time of Dye-sensitized Photodetector

The response/recovery time as well as temporal response are crucial parameters in which the behavior of DS photodetector is determined for practical applications. The photo-switching behavior of the fabricated DS photodetectors was investigated over multiple 100 mW/cm^2 illumination power cycles at zero and 0.2 V bias voltage with $\sim 10 \text{ s}$ pulse width. Figures 4.29 and 4.30 show the photo-switching behavior as a function of time for *Z6A-MMO-T* and *ZrA-MMO-400* DS photodetectors, respectively. The photo-switching behavior of the fabricated DS photodetectors demonstrated a sharp increase in their magnitude under light illumination (–ON” state) and stably returned to low current value in the dark condition (–OFF” state). It is noteworthy to mention that the generated photocurrent is linearly dependent to the applied bias voltage. *Z6A-MMO-400* DS photodetector recorded a higher current (0.65 mA) than other DS photodetectors, for example *Z6A-MMO-200* exhibited value of 0.13 mA at zero bias voltage (Figures 4.29). In the meanwhile (Figures 4.30), *Z3A-MMO-400* DS photodetector demonstrated a value of 0.07 mA at zero bias voltage. These photocurrent values were slightly increased after a small bias voltage of 0.2 V was applied because of photo-excitation, which eventually increased the number of excited electrons which move towards the collection electrode and generated higher photocurrent. At 0.2 V bias voltage, *Z6A-MMO-400*, *Z6A-MMO-200* and *Z3A-MMO-400* DS photodetectors recorded values of 0.7, 0.15 and 0.09 mA, respectively. The same effect behavior of the thermal treatment temperature as well as molar ratio was observed, as it was illustrated in the previous section (4.4.2). Moreover, the ON-OFF switching behavior of the fabricated *Z6A-MMO-T* and *ZrA-MMO-400* DS photodetectors was investigated for all devices and it was noticed to be retained over three multiple cycles, which clearly indicates the reproducibility and robustness of the proposed DS photodetector

performance. The sequence order of photocurrent magnitude at 100 mW/cm² as a function of thermal treatment temperature and molar ratio is illustrated in appendix D.

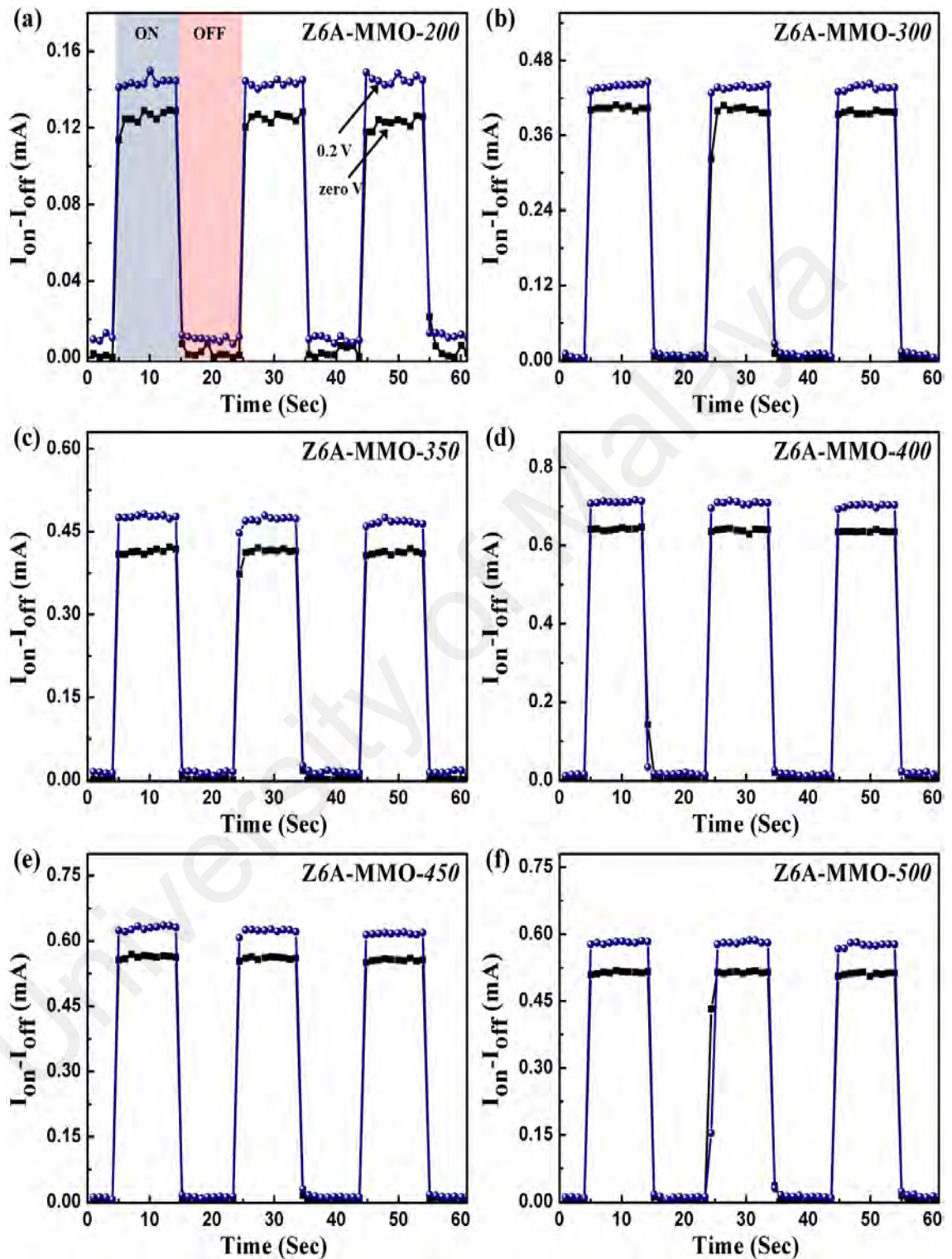


Figure 4.29: Photo-switching characteristics of the fabricated Z6A-MMO-*T* DS photodetectors under alternating dark and light illumination at zero and 0.2 bias voltage; (a) Z6A-MMO-200, (b) Z6A-MMO-300, (c) Z6A-MMO-350, (d) Z6A-MMO-400, (e) Z6A-MMO-450 and (f) Z6A-MMO-500.

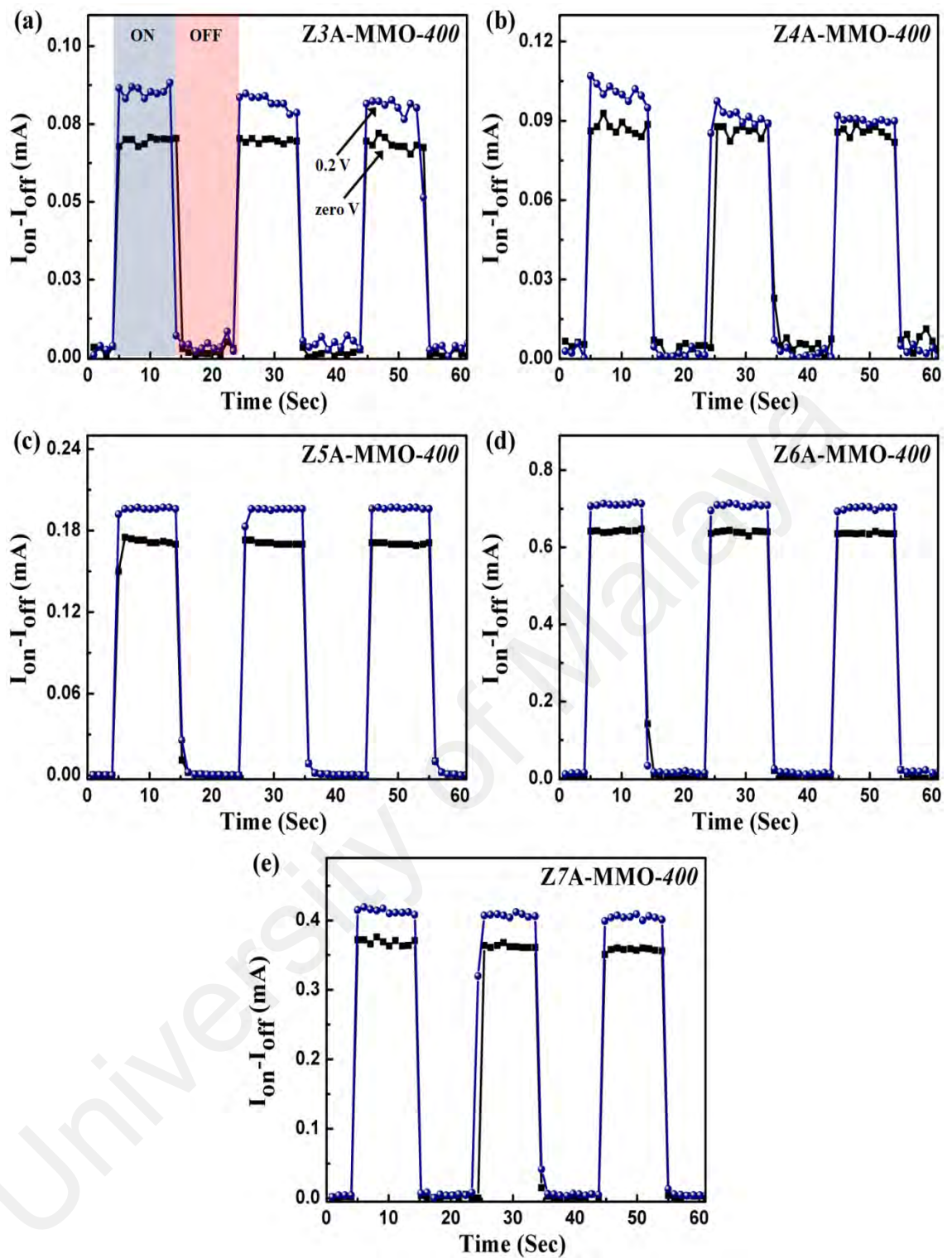


Figure 4.30: Photo-switching characteristics of the fabricated ZrA -MMO-400 DS photodetectors under alternating dark and light illumination at zero and 0.2 bias voltage; (a) Z3A- MMO -400, (b) Z4A- MMO -400, (c) Z5A- MMO -400, (d) Z6A- MMO -400, (e) Z7A- MMO -400.

Finally, the response/recovery time, t_r and t_c , respectively, was calculated as shown in Figure 4.31 for Z6A-*MMO-400* DS photodetector. The fabricated DS photodetector appeared to rise quickly and reach saturation stage with response time less than 1 s. In the meanwhile, the magnitude of photocurrent gradually declined and reach the initial state (dark current) with recovery time of 1 s. The fabricated DS photodetector displayed a short response/recovery time which can be attributed to the easy migration of excited electrons from dye molecules LUMO into the CB of MMO anode materials. The response time was found to be relatively lower than the recovery time which in turn indicates fast electron injection in the CB of MMO materials and subsequently slow recombination process of the excited electrons in MMO materials (S. H. Yu *et al.*, 2014). In similar geometry, the response/recovery time of the fabricated DS photodetector was found to be comparable to other researchers' findings, regardless of the materials used as summarized in Table 4.10. (Y. Lee *et al.*, 2015; Z. Wang *et al.*, 2011).

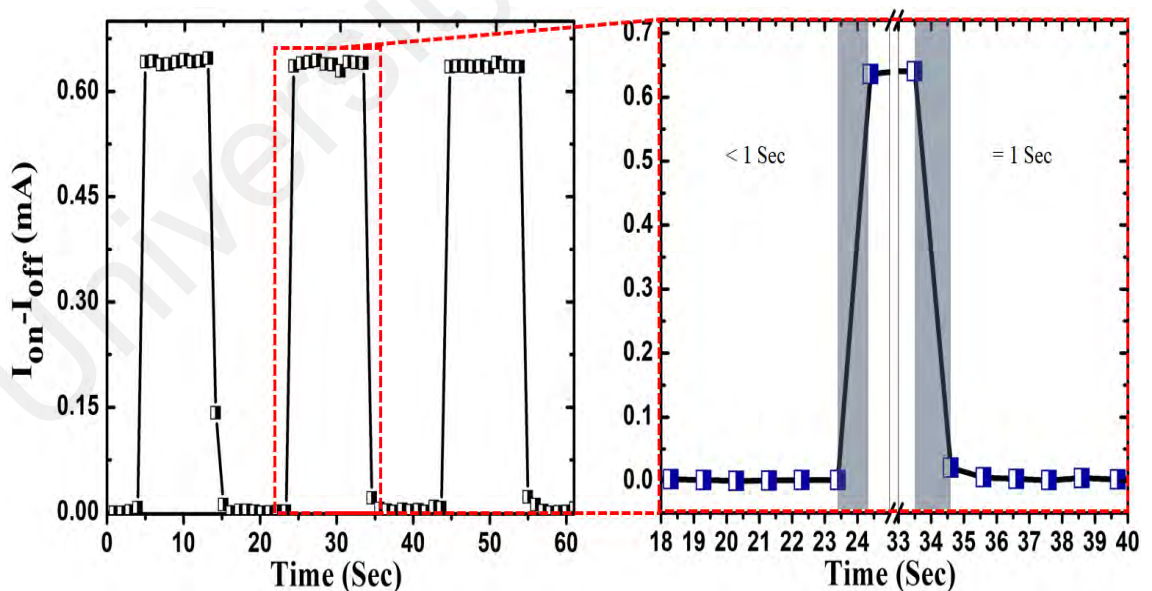


Figure 4.31: Response/recovery time of Z6A-*MMO-400* DS photodetector.

Table 4.10: Response/Recovery time comparison to other researchers' outcomes.

<i>Type of material</i>	<i>t_r (ms)</i>	<i>t_c (ms)</i>	<i>Reference</i>
TiO ₂ /NiTsPc	300	800	(Qadir <i>et al.</i> , 2014)
TiO ₂ /PCPDTBT	937	-	(Qadir <i>et al.</i> , 2015)
MoS ₂ /Rhodamine G	5.1×10^{-3}	2.3	(S. H. Yu <i>et al.</i> , 2014)
ZnO/RhB	2×10^3	2.3×10^3	(Bai & Liu, 2017)

4.5 Summary

The thermal and microstructural properties of pristine ZrA-LDH at different molar ratios were investigated. Furthermore, the structural, morphological, physical and optical characteristics of the prepared Z6A-MMO-400 and ZrA-MMO-400 using ZrA-LDH as precursor were analyzed using XRD, FESEM, BET-BJH, Uv-Vis and PL techniques, respectively. It was found that the optimum thermal treatment temperature, 400 °C, and molar ratio, 6, can give rise to the prepared materials in term of their surface area, band gap and surface defects as compared to pristine Z6A-LDH. In addition, DS photodetector-based Z6A-MMO-*T* and ZrA-MMO-400 as anode materials was fabricated. The photo-responsive behavior of the fabricated DS photodetectors was successfully demonstrated in term of photocurrent, photo-responsivity, photo-conductivity, photo-detectivity, external quantum efficiency, switching behavior and response/recovery time. In similar geometry, the optimum DS photodetector (Z6A-MMO-400) in this work exhibited comparable photo-responsive properties to other DS photodetector in the literature. Moreover, a robust correlation between the investigated properties of the prepared samples, Z6A-MMO-*T* and ZrA-MMO-400, and the DS photodetectors' photo-responsive behavior was successfully demonstrated (Table 4.11).

Table 4.11: Summary of the results analysis for all samples.

No.	Sample	Porous size (nm)	BET surface area (m ² /g)	Band gap (eV)	I_{NE}/I_{PLE} ratio	Dye loading (mol/cm ²)	Photocurrent (A) @ 25	R (A/W)	S (Sm/W)	D* (Jones)	EQE
1	Z6A-LDH	42	17	5.15-3.2	0.13	-	-	-	-	-	-
2	Z6A-MMO-200	46.5	32	3.3	0.19	2.5×10^{-4}	5.4×10^{-5}	2.2×10^{-3}	8.5×10^{-7}	1.0×10^{-10}	0.5
3	Z6A-MMO-300	47	38	3.28	0.23	2.6×10^{-4}	1.7×10^{-4}	7.0×10^{-3}	2.1×10^{-6}	1.5×10^{-10}	1.7
4	Z6A-MMO-350	62	41	3.25	0.30	2.7×10^{-4}	1.8×10^{-4}	7.1×10^{-3}	2.4×10^{-6}	1.4×10^{-10}	1.7
5	Z6A-MMO-400	68.5	53	3.21	0.78	3.3×10^{-4}	2.7×10^{-4}	1.1×10^{-2}	3.3×10^{-6}	1.6×10^{-10}	2.6
6	Z6A-MMO-450	65	51	3.21	0.63	3.2×10^{-4}	2.4×10^{-4}	9.4×10^{-3}	3.0×10^{-6}	1.6×10^{-10}	2.2
7	Z6A-MMO-500	35	46	3.22	0.55	2.7×10^{-4}	2.1×10^{-4}	8.6×10^{-3}	2.7×10^{-6}	1.4×10^{-10}	2.0
8	Z3A-MMO-400	12.6	39	3.24	0.13	2.6×10^{-4}	3.6×10^{-5}	1.5×10^{-3}	4.3×10^{-7}	7.1×10^{-9}	0.4
9	Z4A-MMO-400	44.2	40	3.24	0.16	2.7×10^{-4}	4.1×10^{-5}	1.6×10^{-3}	4.6×10^{-7}	5.9×10^{-9}	0.4
10	Z5A-MMO-400	46.7	44	3.22	0.17	2.7×10^{-4}	4.6×10^{-5}	1.9×10^{-3}	5.0×10^{-7}	6.0×10^{-9}	0.4
11	Z6A-MMO-400	68.5	53	3.21	0.78	3.3×10^{-4}	2.7×10^{-4}	1.1×10^{-2}	3.3×10^{-6}	1.6×10^{-10}	2.6
12	Z7A-MMO-400	32.6	51	3.22	0.27	3.2×10^{-4}	1.5×10^{-4}	6.1×10^{-3}	1.8×10^{-6}	1.7×10^{-10}	1.4

CHAPTER 5: CONCLUSION AND RECOMMENDATIONS

5.1 Conclusion

In conclusion of the present thesis, we successfully demonstrated the synthesization of *ZrA*-LDH nanoparticles at different molar ratios of Zn^{+2} to Al^{+3} via co-precipitation method. Subsequently, *ZrA*-MMO-400 as well as *Z₆A*-MMO-*T* as anode materials were prepared through doctor-blade and thermal oxidation techniques using the as-synthesized *ZrA*-LDH as precursor. Afterward, the prepared anode materials were further used in the fabrication of DS photodetector devices. XRD analysis was successfully conducted to identify the major phases of the prepared LDHs and the metal phases of ZnO and ZnAl_2O_4 spinel in the prepared anode materials (*ZrA*-LDH, *Z₆A*-MMO-*T* and *ZrA*-MMO-400). The main finding of the microstructural, optical and photo-responsive analysis of the prepared anode materials and fabricated DS photodetectors are summarized as follows:

1. A continuous mesoporous layer of the synthesized *ZrA*-LDH was obtained via modified co-precipitation method. Furthermore, a detailed microstructural analysis of *ZrA*-LDH was presented using TGA, XRD, FESEM, N_2 adsorption/desorption isotherm while *Z₆A*-LDH was further analyzed using UV-Vis and PL techniques.
2. It was found that molar ratio of 6 and oxidation temperature of 400 °C delivered the highest BET surface area, voids size and on the contrary the lowest optical band gap and surface defects. The optimum sample, *Z₆A*-MMO-400, demonstrated values of 68 nm, 53 m²/g, 3.21 eV and 0.78 for porous size, BET surface area, optical band gap and surface defects, respectively. On the contrary, pristine *Z₆A*-LDH showed values of 42 nm, 17 m²/g, 5.15-3.2 eV, 0.13 for porous size, BET surface area, optical band gap and surface defects, respectively.

3. The photo-responsive behavior of the fabricated DS photodetector was investigated, where the optimum device (Z6A-MMO-400 DS photodetector) demonstrated a photocurrent magnitude of 6.5×10^{-4} A at 100 mW/cm^2 and zero bias voltage. In addition, values of photo-responsivity and effective quantum efficiency were found to be 1.1×10^{-2} A/W and 2.6, respectively, at 25 mW/cm^2 and zero bias voltage. Nevertheless, it was also observed that the optimum device exhibited relatively shorter response than the recovery time.
4. The proposed MMO anode materials system provides breakthrough pathway to fabricate low-cost and easy fabrication process DS photodetector. Additionally, it can be clearly observed that, using LDH as a precursor, a successful robust correlation between the microstructural and optical properties of the anode materials and the fabricated DS photodetector photo-responsive behavior was successfully demonstrated.

5.2 Recommendations and future work

There are still some efforts which can be taken into consideration to further develop the proposed materials performance as follows:

1. Based on the current experiment works, additional treatment ought to be considered in term of the LDH synthesis process, for example longer period for layers growth and/or different temperature may result in higher surface area and subsequently higher dye loading amount.
2. Further reduction in the surface defects, ratio between $I_{\text{NBE}}/I_{\text{DLE}}$, through morphological modifications of the proposed MMO anode materials should also be considered. For instance, nanoroads and/or nanowalls with high crystallinity in order to enhance the phase purity which in turn result in lower surface defects is an approach.

3. In this study, dye N719 was employed as photon absorber in the visible light in which measurement of the fabricated DS photodetector took a place. It is highly recommended to use the proposed photodetector in the UV region where the prepared anode materials are effective in term of their optical behavior. This would broaden the spectral response of the proposed DS photodetector in both UV and visible light region.

University of Malaya

REFERENCES

- Abderrazek, K., Frini Srasra, N., & Srasra, E. (2017). Synthesis and Characterization of [Zn-Al] Layered Double Hydroxides: Effect of the Operating Parameters. *Journal of the Chinese Chemical Society*, 64(3), 346-353.
- Ahmed, A. A. A., Talib, Z. A., bin Hussein, M. Z., & Zakaria, A. (2012a). Improvement of the crystallinity and photocatalytic property of zinc oxide as calcination product of Zn-Al layered double hydroxide. *Journal of Alloys and Compounds*, 539, 154-160.
- Ahmed, A. A. A., Talib, Z. A., bin Hussein, M. Z., & Zakaria, A. (2012b). Zn-Al layered double hydroxide prepared at different molar ratios: Preparation, characterization, optical and dielectric properties. *Journal of Solid State Chemistry*, 191, 271-278.
- Ahrenkiel, R., Dunlavy, D., & Hanak, T. (1988). Minority-carrier lifetime in ITO/InP heterojunctions. *Journal of applied physics*, 64(4), 1916-1921.
- Ai, H., Huang, X., Zhu, Z., Liu, J., Chi, Q., Li, Y., . . . Ji, X. (2008). A novel glucose sensor based on monodispersed Ni/Al layered double hydroxide and chitosan. *Biosensors and Bioelectronics*, 24(4), 1048-1052.
- Ajaikumar, S., & Pandurangan, A. (2009). Efficient synthesis of quinoxaline derivatives over ZrO_2/M_xO_y (M= Al, Ga, In and La) mixed metal oxides supported on MCM-41 mesoporous molecular sieves. *Applied Catalysis A: General*, 357(2), 184-192.
- Al-Kahlout, A. (2015). Thermal treatment optimization of ZnO nanoparticles-photoelectrodes for high photovoltaic performance of dye-sensitized solar cells. *Journal of the Association of Arab Universities for Basic and Applied Sciences*, 17, 66-72.
- Ali Ahmed, A. A., Talib, Z. A., & Hussein, M. Z. (2012a). ESR spectra and thermal diffusivity of Zn-Al layered double hydroxide. *Journal of Physics and Chemistry of Solids*, 73(1), 124-128.
- Ali Ahmed, A. A., Talib, Z. A., & Hussein, M. Z. (2012b). Thermal, optical and dielectric properties of Zn-Al layered double hydroxide. *Applied Clay Science*, 56, 68-76.
- Ali Ahmed, A. A., Talib, Z. A., & Hussein, M. Z. (2013). Influence of metallic molar ratio on the electron spin resonance and thermal diffusivity of Zn-Al layered double hydroxide. *Journal of Nanomaterials*, 2013, 105.
- Ali Ahmed, A. A., Talib, Z. A., Hussein, M. Z., & Zakaria, A. (2012). Zn-Al layered double hydroxide prepared at different molar ratios: Preparation, characterization, optical and dielectric properties. *Journal of Solid State Chemistry*, 191, 271-278.

- Alshanableh, A., Yap, C. C., Tan, S. T., Lee, H. B., Tan, C. H., Ginting, R. T., & Jumali, M. H. H. (2016). Novel hydrothermal approach to functionalize self-oriented twin ZnO nanotube arrays. *Materials Letters*, *165*, 75-78.
- Ardo, S., & Meyer, G. J. (2009). Photodriven heterogeneous charge transfer with transition-metal compounds anchored to TiO₂ semiconductor surfaces. *Chemical Society Reviews*, *38*(1), 115-164.
- Bai, Z. Q., & Liu, Z. W. (2017). A broadband photodetector based on Rhodamine B-sensitized ZnO nanowires film. *Scientific Reports*, *7*, 11384.
- Béres, A., Pálincó, I., Kiricsi, I., Nagy, J. B., Kiyozumi, Y., & Mizukami, F. (1999). Layered double hydroxides and their pillared derivatives—materials for solid base catalysis; synthesis and characterization. *Applied Catalysis A: General*, *182*(2), 237-247.
- Bond, G. C. (1962). *Catalysis by metals*: Academic Press.
- Boschloo, G., & Hagfeldt, A. (2009). Characteristics of the iodide/triiodide redox mediator in dye-sensitized solar cells. *Accounts of Chemical Research*, *42*(11), 1819-1826.
- Braterman, P. S., Xu, Z. P., & Yarberrry, F. (2004). Layered double hydroxides (LDHs). *Handbook of layered materials*, 373-474.
- Caglar, M., Ilican, S., Caglar, Y., & Yakuphanoglu, F. (2009). Electrical conductivity and optical properties of ZnO nanostructured thin film. *Applied Surface Science*, *255*(8), 4491-4496.
- Cao, F., Tian, W., Gu, B., Ma, Y., Lu, H., & Li, L. (2017). High-performance UV–vis photodetectors based on electrospun ZnO nanofiber-solution processed perovskite hybrid structures. *Nano Research*, *10*(7), 2244-2256.
- Cao, J., Zhao, Y., Zhu, Y., Yang, X., Shi, P., Xiao, H., . . . Liu, J. (2017). Preparation and photovoltaic properties of CdS quantum dot-sensitized solar cell based on zinc tin mixed metal oxides. *Journal of Colloid and Interface Science*, *498*, 223-228.
- Cao, J., Zhu, Y., Yang, X., Chen, Y., Li, Y., Xiao, H., . . . Liu, J. (2016). The promising photo anode of graphene/zinc titanium mixed metal oxides for the CdS quantum dot-sensitized solar cell. *Solar Energy Materials and Solar Cells*, *157*, 814-819.
- Carja, G., Nakajima, A., Dranca, S., Dranca, C., & Okada, K. (2010). TiO₂/ZnLDH as a self-assembled nanocomposite with photoresponsive properties. *The Journal of Physical Chemistry C*, *114*(35), 14722-14728.
- Casady, J., & Johnson, R. W. (1996). Status of silicon carbide (SiC) as a wide-bandgap semiconductor for high-temperature applications: A review. *Solid-State Electronics*, *39*(10), 1409-1422.
- Cavani, F., Trifirò, F., & Vaccari, A. (1991). Hydrotalcite-type anionic clays: Preparation, properties and applications. *Catalysis today*, *11*(2), 173-301.

- Chai, H., Xu, X., Lin, Y., Evans, D. G., & Li, D. (2009). Synthesis and UV absorption properties of 2, 3-dihydroxynaphthalene-6-sulfonate anion-intercalated Zn–Al layered double hydroxides. *Polymer Degradation and stability*, 94(4), 744-749.
- Chang, S.-H., Fang, Y.-K., Hsu, K.-C., & Wei, T.-C. (2008). GaN UV MSM photodetector on porous β -SiC/(111) Si substrates. *Sensors and Actuators A: Physical*, 147(1), 1-5.
- Chang, S., Chang, S., Lu, C., & Chuang, R. (2008). *GaN photodetectors prepared on silicon and sapphire substrates*. Paper presented at the Electron Devices and Solid-State Circuits, 2008. EDSSC 2008. IEEE International Conference on.
- Chen, P.-Y., Dang, X., Klug, M. T., Qi, J., Dorval Courchesne, N. m.-M., Burpo, F. J., . . . Belcher, A. M. (2013). Versatile three-dimensional virus-based template for dye-sensitized solar cells with improved electron transport and light harvesting. *ACS nano*, 7(8), 6563-6574.
- Chen, X., Fu, C., Wang, Y., Yang, W., & Evans, D. G. (2008). Direct electrochemistry and electrocatalysis based on a film of horseradish peroxidase intercalated into Ni–Al layered double hydroxide nanosheets. *Biosensors and Bioelectronics*, 24(3), 356-361.
- Chen, X., Li, J., Sun, Z., Fang, X., Wei, Z., Fang, F., . . . Wang, X. (2013). The formation and acceptor related emission behavior of ZnO/ZnAl₂O₄ core–shell structures. *Journal of Alloys and Compounds*, 571, 114-117.
- Cheng, X., Huang, X., Wang, X., & Sun, D. (2010a). Influence of calcination on the adsorptive removal of phosphate by Zn–Al layered double hydroxides from excess sludge liquor. *Journal of hazardous materials*, 177(1-3), 516-523.
- Cheng, X., Huang, X., Wang, X., & Sun, D. (2010b). Influence of calcination on the adsorptive removal of phosphate by Zn–Al layered double hydroxides from excess sludge liquor. *Journal of hazardous materials*, 177(1), 516-523.
- Cho, S., Jang, J. W., Kong, K. j., Kim, E. S., Lee, K. H., & Lee, J. S. (2013). Anion-Doped Mixed Metal Oxide Nanostructures Derived from Layered Double Hydroxide as Visible Light Photocatalysts. *Advanced Functional Materials*, 23(19), 2348-2356.
- Choi, S.-W., Park, J. Y., & Kim, S. S. (2009). Synthesis of SnO₂–ZnO core–shell nanofibers via a novel two-step process and their gas sensing properties. *Nanotechnology*, 20(46), 465603.
- Chung, D. S., Kim, Y.-H., & Lee, J.-S. (2013). Achieving high sensitivity in hybrid photodetectors based on an organic single crystal and an inorganic nanocrystal array. *Nanotechnology*, 25(3), 035202.
- Cui, G., Evans, D. G., & Li, D. (2010). Synthesis and UV absorption properties of 5, 5'-thiodisalicylic acid intercalated Zn– Al layered double hydroxides. *Polymer Degradation and stability*, 95(10), 2082-2087.

- Cullity, D., & Stock, S. (2001). Elements of X-ray Diffraction. In: New Jersey: Prentice Hall.
- Daeneke, T., Kwon, T.-H., Holmes, A. B., Duffy, N. W., Bach, U., & Spiccia, L. (2011). High-efficiency dye-sensitized solar cells with ferrocene-based electrolytes. *Nature chemistry*, 3(3), 211-215.
- Dembele, K. T., Selopal, G. S., Soldano, C., Nechache, R., Rimada, J. C., Concina, I., . . . Vomiero, A. (2013). Hybrid carbon nanotubes–TiO₂ photoanodes for high efficiency dye-sensitized solar cells. *The Journal of Physical Chemistry C*, 117(28), 14510-14517.
- Devan, R. S., Patil, R. A., Lin, J. H., & Ma, Y. R. (2012). One-Dimensional Metal-Oxide Nanostructures: Recent Developments in Synthesis, Characterization, and Applications. *Advanced Functional Materials*, 22(16), 3326-3370.
- Dodd, A., McKinley, A., Saunders, M., & Tsuzuki, T. (2006). Mechanochemical synthesis of nanocrystalline SnO₂–ZnO photocatalysts. *Nanotechnology*, 17(3), 692.
- Dong, J., Han, D., Li, H., Yu, W., Zhang, S., Zhang, X., & Wang, Y. (2018). Effect of Al doping on performance of ZnO thin film transistors. *Applied Surface Science*, 433, 836-839.
- Dualeh, A. (2014). Analysis of Key Electronic, Optical and Structural Parameters in Mesoscopic Solid-State Solar Cells.
- Dwibedi, D., Murugesan, C., Leskes, M., & Barpanda, P. (2018). Role of annealing temperature on cation ordering in hydrothermally prepared zinc aluminate (ZnAl₂O₄) spinel. *Materials Research Bulletin*, 98, 219-224.
- Elia, A., Aispuro, P. M., Quaranta, N., Martín-Martínez, J. M., & Vázquez, P. (2011). *Synthesis and Characterization of New Silica-Titania Mixed Oxides Obtained by Sol-Gel Technique*. Paper presented at the Macromolecular Symposia.
- Evans, D. G., & Duan, X. (2006). Preparation of layered double hydroxides and their applications as additives in polymers, as precursors to magnetic materials and in biology and medicine. *Chemical Communications*(5), 485-496.
- Evans, D. G., & Slade, R. C. (2006). Structural aspects of layered double hydroxides. In *Layered double hydroxides* (pp. 1-87): Springer.
- Fan, H. J., Yang, Y., & Zacharias, M. (2009). ZnO-based ternary compound nanotubes and nanowires. *Journal of Materials Chemistry*, 19(7), 885-900.
- Fang, X., Ma, T., Guan, G., Akiyama, M., & Abe, E. (2004). Performances characteristics of dye-sensitized solar cells based on counter electrodes with Pt films of different thickness. *Journal of Photochemistry and Photobiology A: Chemistry*, 164(1), 179-182.

- Fang, Z., Yan, Z., Tan, Y., Liu, X., & Wang, Y. (2005). Influence of post-annealing treatment on the structure properties of ZnO films. *Applied surface science*, 241(3), 303-308.
- Feng, X., Zhu, K., Frank, A. J., Grimes, C. A., & Mallouk, T. E. (2012). Rapid charge transport in dye-sensitized solar cells made from vertically aligned single-crystal rutile TiO₂ nanowires. *Angewandte Chemie*, 124(11), 2781-2784.
- Foruzin, L. J., Rezvani, Z., & Nejati, K. (2016). Fabrication of TiO₂@ ZnAl-layered double hydroxide based anode material for dye-sensitized solar cell. *RSC Advances*, 6(13), 10912-10918.
- Gao, C., Li, X., Wang, Y., Chen, L., Pan, X., Zhang, Z., & Xie, E. (2013). Titanium dioxide coated zinc oxide nanostrawberry aggregates for dye-sensitized solar cell and self-powered UV-photodetector. *Journal of Power Sources*, 239, 458-465.
- Gawande, M. B., Pandey, R. K., & Jayaram, R. V. (2012). Role of mixed metal oxides in catalysis science—versatile applications in organic synthesis. *Catalysis Science & Technology*, 2(6), 1113-1125.
- Gfroerer, T. H. (2000). Photoluminescence in analysis of surfaces and interfaces. *Encyclopedia of Analytical Chemistry*.
- Gong, J., Liang, J., & Sumathy, K. (2012). Review on dye-sensitized solar cells (DSSCs): fundamental concepts and novel materials. *Renewable and Sustainable Energy Reviews*, 16(8), 5848-5860.
- Gong, X., Tong, M., Xia, Y., Cai, W., Moon, J. S., Cao, Y., . . . Heeger, A. J. (2009). High-detectivity polymer photodetectors with spectral response from 300 nm to 1450 nm. *science*, 325(5948), 1665-1667.
- Guo, Z., Zhao, D., Liu, Y., Shen, D., Zhang, J., & Li, B. (2008). Visible and ultraviolet light alternative photodetector based on ZnO nanowire/n-Si heterojunction. *Applied Physics Letters*, 93(16), 163501.
- Hadnadjev-Kostic, M., Vulic, T., Marinkovic-Neducin, R., Lončarević, D., Dostanić, J., Markov, S., & Jovanović, D. (2017). Photo-induced properties of photocatalysts: A study on the modified structural, optical and textural properties of TiO₂-ZnAl layered double hydroxide based materials. *Journal of Cleaner Production*, 164, 1-18.
- Hagfeldt, A., Boschloo, G., Sun, L., Kloo, L., & Pettersson, H. (2010). Dye-sensitized solar cells. *Chemical reviews*, 110(11), 6595-6663.
- Hagfeldt, A., & Grätzel, M. (2000). Molecular photovoltaics. *Accounts of Chemical Research*, 33(5), 269-277.
- Hamann, T. W., Jensen, R. A., Martinson, A. B., Van Ryswyk, H., & Hupp, J. T. (2008). Advancing beyond current generation dye-sensitized solar cells. *Energy & Environmental Science*, 1(1), 66-78.

- Hassanein, A. M., Salahuddin, N. A., Matsuda, A., Hattori, T., & Elfiky, M. N. (2017). Fabrication of Biosensor Based on Layered Double Hydroxide/Polypyrrole/Carbon Paste Electrode for Determination of Anti-Hypertensive and Prostatic Hyperplasia Drug Terazosin. *World Academy of Science, Engineering and Technology, International Journal of Biomedical and Biological Engineering*, 4(11).
- He, J., Wei, M., Li, B., Kang, Y., Evans, D. G., & Duan, X. (2006). Preparation of layered double hydroxides. In *Layered double hydroxides* (pp. 89-119): Springer.
- He, Z., Zhang, W., Zhang, W., Jie, J., Luo, L., Yuan, G., . . . Lee, C.-S. (2010). High-performance CdSe: In nanowire field-effect transistors based on top-gate configuration with high-K non-oxide dielectrics. *The Journal of Physical Chemistry C*, 114(10), 4663-4668.
- Herschel, W. (1800). II. Experiments on the refrangibility of the invisible rays of the sun. *The Philosophical Magazine: Comprehending the Various Branches of Science, the Liberal and Fine Arts, Agriculture, Manufactures, and Commerce*, 8(29), 9-15.
- Hosono, E., Fujihara, S., Honma, I., & Zhou, H. (2005). The fabrication of an upright-standing zinc oxide nanosheet for use in dye-sensitized solar cells. *Advanced Materials*, 17(17), 2091-2094.
- Huang, J.-S., Hsiao, C.-Y., Syu, S.-J., Chao, J.-J., & Lin, C.-F. (2009). Well-aligned single-crystalline silicon nanowire hybrid solar cells on glass. *Solar Energy Materials and Solar Cells*, 93(5), 621-624.
- Hussein, M. Z. B., Yun-Hin, T.-Y., bin Tawang, M. M., & Shahadan, R. (2002). Thermal degradation of (zinc–aluminium-layered double hydroxide-dioctyl sulphosuccinate) nanocomposite. *Materials chemistry and physics*, 74(3), 265-271.
- Huynh, W. U., Dittmer, J. J., & Alivisatos, A. P. (2002). Hybrid nanorod-polymer solar cells. *science*, 295(5564), 2425-2427.
- Issa, B., Obaidat, I. M., Albiss, B. A., & Haik, Y. (2013). Magnetic nanoparticles: surface effects and properties related to biomedicine applications. *International journal of molecular sciences*, 14(11), 21266-21305.
- Jailaubekov, A. E., Willard, A. P., Tritsch, J. R., Chan, W.-L., Sai, N., Gearba, R., . . . Rossky, P. J. (2013). Hot charge-transfer excitons set the time limit for charge separation at donor/acceptor interfaces in organic photovoltaics. *Nature materials*, 12(1), 66-73.
- Jarzab, D., Szendrei, K., Yarema, M., Pichler, S., Heiss, W., & Loi, M. A. (2011). Charge-Separation Dynamics in Inorganic–Organic Ternary Blends for Efficient Infrared Photodiodes. *Advanced Functional Materials*, 21(11), 1988-1992.

- Jiang, D., Su, L., Ma, L., Yao, N., Xu, X., Tang, H., & Li, X. (2010). Cu–Zn–Al mixed metal oxides derived from hydroxycarbonate precursors for H₂S removal at low temperature. *Applied surface science*, 256(10), 3216-3223.
- Jiang, Y., Zhang, W. J., Jie, J. S., Meng, X. M., Fan, X., & Lee, S. T. (2007). Photoresponse Properties of CdSe Single-Nanoribbon Photodetectors. *Advanced Functional Materials*, 17(11), 1795-1800.
- Jie, J., Zhang, W., Bello, I., Lee, C.-S., & Lee, S.-T. (2010). One-dimensional II–VI nanostructures: synthesis, properties and optoelectronic applications. *Nano today*, 5(4), 313-336.
- Joly, D., Pellejà, L., Narbey, S., Oswald, F., Chiron, J., Clifford, J. N., . . . Demadrille, R. (2014). A robust organic dye for dye sensitized solar cells based on iodine/iodide electrolytes combining high efficiency and outstanding stability. *Scientific Reports*, 4, 4033.
- Kalita, G., Adhikari, S., Aryal, H. R., Afre, R., Soga, T., Sharon, M., . . . Umeno, M. (2009). Silicon nanowire array/polymer hybrid solar cell incorporating carbon nanotubes. *Journal of Physics D: Applied Physics*, 42(11), 115104.
- Kang, M.-S., Kim, J. H., Kim, Y. J., Won, J., Park, N.-G., & Kang, Y. S. (2005). Dye-sensitized solar cells based on composite solid polymer electrolytes. *Chemical Communications*(7), 889-891.
- Khelashvili, G., Behrens, S., Weidenthaler, C., Vetter, C., Hinsch, A., Kern, R., . . . Bönnemann, H. (2006). Catalytic platinum layers for dye solar cells: A comparative study. *Thin Solid Films*, 511, 342-348.
- Kim, K., Kim, J.-J., & Kim, D.-H. (2017). Organic photodetector and image sensor. In: Google Patents.
- Kim, Y. J., Park, C. E., & Chung, D. S. (2014). Interface engineering of a highly sensitive solution processed organic photodiode. *Physical Chemistry Chemical Physics*, 16(34), 18472-18477.
- Kolmakov, A., & Moskovits, M. (2004). Chemical sensing and catalysis by one-dimensional metal-oxide nanostructures. *Annu. Rev. Mater. Res.*, 34, 151-180.
- Konle, J., Presting, H., Kibbel, H., Thonke, K., & Sauer, R. (2001). Enhanced performance of silicon based photodetectors using silicon/germanium nanostructures. *Solid-State Electronics*, 45(11), 1921-1925.
- Konstantatos, G., Howard, I., Fischer, A., Hoogland, S., Clifford, J., Klem, E., . . . Sargent, E. H. (2006). Ultrasensitive solution-cast quantum dot photodetectors. *nature*, 442(7099), 180-183.
- Konstantatos, G., & Sargent, E. H. (2011). Colloidal quantum dot photodetectors. *Infrared Physics & Technology*, 54(3), 278-282.

- Krüger, J., Plass, R., Cevey, L., Piccirelli, M., Grätzel, M., & Bach, U. (2001). High efficiency solid-state photovoltaic device due to inhibition of interface charge recombination. *Applied Physics Letters*, 79(13), 2085-2087.
- Kung, H. H. (1989). *Transition metal oxides: surface chemistry and catalysis* (Vol. 45): Elsevier.
- Latorre-Sanchez, M., Atienzar, P., Abellán, G., Puche, M., Fornés, V., Ribera, A., & García, H. (2012). The synthesis of a hybrid graphene–nickel/manganese mixed oxide and its performance in lithium-ion batteries. *Carbon*, 50(2), 518-525.
- Lee, J. H., Rhee, S. W., Nam, H. J., & Jung, D. Y. (2009). Surface selective deposition of PMMA on layered double hydroxide nanocrystals immobilized on solid substrates. *Advanced Materials*, 21(5), 546-549.
- Lee, Y., Yu, S. H., Jeon, J., Kim, H., Lee, J. Y., Kim, H., . . . Cho, J. H. (2015). Hybrid structures of organic dye and graphene for ultrahigh gain photodetectors. *Carbon*, 88, 165-172.
- Lehtinen, K. E., & Zachariah, M. R. (2001). Effect of coalescence energy release on the temporal shape evolution of nanoparticles. *Physical Review B*, 63(20), 205402.
- Lei, X., Zhang, F., Yang, L., Guo, X., Tian, Y., Fu, S., . . . Duan, X. (2007). Highly crystalline activated layered double hydroxides as solid acid-base catalysts. *AIChE journal*, 53(4), 932-940.
- Lenzmann, F., & Kroon, J. (2007). Recent advances in dye-sensitized solar cells. *Advances in OptoElectronics*, 2007.
- Lhuillier, E., & Guyot-Sionnest, P. (2017). Recent Progresses in Mid Infrared Nanocrystal Optoelectronics. *IEEE Journal of Selected Topics in Quantum Electronics*, 23(5), 1-8.
- Li, F., & Duan, X. (2006). Applications of layered double hydroxides. In *Layered double hydroxides* (pp. 193-223): Springer.
- Li, H., Yao, C., Meng, L., Sun, H., Huang, J., & Gong, Q. (2013). Photoelectrochemical performance of hydrogenated ZnO/CdS core–shell nanorod arrays. *Electrochimica Acta*, 108, 45-50.
- Li, L., Ma, R., Ebina, Y., Fukuda, K., Takada, K., & Sasaki, T. (2007). Layer-by-layer assembly and spontaneous flocculation of oppositely charged oxide and hydroxide nanosheets into inorganic sandwich layered materials. *Journal of the American Chemical Society*, 129(25), 8000-8007.
- Li, Z., Wang, J., Xu, X., & Ye, X. (2008). The evolution of optical properties during hydrothermal coarsening of ZnS nanoparticles. *Materials Letters*, 62(23), 3862-3864.
- Lin, H., Liu, H., Qian, X., Lai, S.-W., Li, Y., Chen, N., . . . Li, Y. (2011). Constructing a blue light photodetector on inorganic/organic p–n heterojunction nanowire arrays. *Inorganic chemistry*, 50(16), 7749-7753.

- Listorti, A., O'Regan, B., & Durrant, J. R. (2011). Electron transfer dynamics in dye-sensitized solar cells. *Chemistry of Materials*, 23(15), 3381-3399.
- Liu, X., Wei, M., Li, F., & Duan, X. (2007). Intraparticle diffusion of 1-phenyl-1, 2-ethanediol in layered double hydroxides. *AIChE journal*, 53(6), 1591-1600.
- Lopez-Sanchez, O., Lembke, D., Kayci, M., Radenovic, A., & Kis, A. (2013). Ultrasensitive photodetectors based on monolayer MoS₂. *Nature nanotechnology*, 8(7), 497-501.
- Lü, Z., Zhang, F., Lei, X., Yang, L., Xu, S., & Duan, X. (2008). In situ growth of layered double hydroxide films on anodic aluminum oxide/aluminum and its catalytic feature in aldol condensation of acetone. *Chemical Engineering Science*, 63(16), 4055-4062.
- Luo, L., Tao, W., Hu, X., Xiao, T., Heng, B., Huang, W., . . . Wang, J. (2011). Mesoporous F-doped ZnO prism arrays with significantly enhanced photovoltaic performance for dye-sensitized solar cells. *Journal of Power Sources*, 196(23), 10518-10525.
- Luo, L., Zhang, Y., Mao, S. S., & Lin, L. (2006). Fabrication and characterization of ZnO nanowires based UV photodiodes. *Sensors and Actuators A: Physical*, 127(2), 201-206.
- Luszczynska, B., Szymanski, M., Verilhac, J., Reiss, P., & Djurado, D. (2013). Improved external quantum efficiency of solution-processed P3HT: 60PCBM photodetectors by the addition of Cu-In-Se nanocrystals. *Organic Electronics*, 14(12), 3206-3212.
- Maçaira, J., Andrade, L., & Mendes, A. (2013). Review on nanostructured photoelectrodes for next generation dye-sensitized solar cells. *Renewable and Sustainable Energy Reviews*, 27, 334-349.
- Marrs, M. A., Moyer, C. D., Bawolek, E. J., Cordova, R. J., Trujillo, J., Raupp, G. B., & Vogt, B. D. (2011). Control of threshold voltage and saturation mobility using dual-active-layer device based on amorphous mixed metal-oxide-semiconductor on flexible plastic substrates. *IEEE Transactions on Electron Devices*, 58(10), 3428-3434.
- Mathew, S., Yella, A., Gao, P., Humphry-Baker, R., Curchod, B. F., Ashari-Astani, N., . . . Grätzel, M. (2014). Dye-sensitized solar cells with 13% efficiency achieved through the molecular engineering of porphyrin sensitizers. *Nature chemistry*, 6(3), 242-247.
- Meng, Q.-B., Takahashi, K., Zhang, X.-T., Sutanto, I., Rao, T., Sato, O., . . . Urugami, M. (2003). Fabrication of an efficient solid-state dye-sensitized solar cell. *langmuir*, 19(9), 3572-3574.
- Mikulics, M., Marso, M., Kordoš, P., Stanček, S., Kováč, P., Zheng, X., . . . Sobolewski, R. (2003). Ultrafast and highly sensitive photodetectors fabricated on high-energy nitrogen-implanted GaAs. *Applied Physics Letters*, 83(9), 1719-1721.

- Millan, J., Godignon, P., Perpina, X., Pérez-Tomás, A., & Rebollo, J. (2014). A survey of wide bandgap power semiconductor devices. *IEEE transactions on Power Electronics*, 29(5), 2155-2163.
- Monroy, E., Omnès, F., & Calle, F. (2003). Wide-bandgap semiconductor ultraviolet photodetectors. *Semiconductor Science and Technology*, 18(4), R33.
- Morandi, S., Prinetto, F., Di Martino, M., Ghiotti, G., Lorret, O., Tichit, D., . . . Carotta, M. (2006). Synthesis and characterisation of gas sensor materials obtained from Pt/Zn/Al layered double hydroxides. *Sensors and Actuators B: Chemical*, 118(1), 215-220.
- Musselman, K. P., Marin, A., Schmidt-Mende, L., & MacManus-Driscoll, J. L. (2012). Incompatible length scales in nanostructured Cu₂O solar cells. *Advanced Functional Materials*, 22(10), 2202-2208.
- Nasr, M., Viter, R., Eid, C., Warmont, F., Habchi, R., Miele, P., & Bechelany, M. (2016). Synthesis of novel ZnO/ZnAl₂O₄ multi co-centric nanotubes and their long-term stability in photocatalytic application. *RSC Advances*, 6(105), 103692-103699.
- Neto, S. Y., da Silva, F. G. S., Souto, D. E. P., Faria, A. R., de Andrade, H. M., Luz, R. d. C. S., . . . Damos, F. S. (2017). Photoelectrochemical immunodiagnosis of canine leishmaniasis using cadmium-sulfide-sensitized zinc oxide modified with synthetic peptides. *Electrochemistry Communications*, 82, 75-79.
- O'regan, B., & Grätzel, M. (1991a). A low-cost, high-efficiency solar cell based on dye-sensitized colloidal TiO₂ films. *nature*, 353(6346), 737-740.
- O'regan, B., & Grätzel, M. (1991b). A low-cost, high-efficiency solar cell based on dye-sensitized colloidal TiO₂ films. *nature*, 353(6346), 737-740.
- Omar, A., & Abdullah, H. (2014). Electron transport analysis in zinc oxide-based dye-sensitized solar cells: a review. *Renewable and Sustainable Energy Reviews*, 31, 149-157.
- Omnès, F., Monroy, E., Muñoz, E., & Reverchon, J.-L. (2007). *Wide bandgap UV photodetectors: A short review of devices and applications*. Paper presented at the Proc. of SPIE.
- Pan, S., Liu, Q., Zhao, J., & Li, G. (2017). Ultrahigh Detectivity and Wide Dynamic Range Ultraviolet Photodetectors Based on Bi_xSn_{1-x}O₂ Intermediate Band Semiconductor. *ACS applied materials & interfaces*, 9(34), 28737-28742.
- Papageorgiou, N. (2004). Counter-electrode function in nanocrystalline photoelectrochemical cell configurations. *Coordination chemistry reviews*, 248(13), 1421-1446.
- Papageorgiou, N., Maier, W., & Grätzel, M. (1997). An iodine/triiodide reduction electrocatalyst for aqueous and organic media. *Journal of The Electrochemical Society*, 144(3), 876-884.

- Park, H., Hussain, S. Q., Velumani, S., Le, A. H. T., Ahn, S., Kim, S., & Yi, J. (2015). Influence of working pressure on the structural, optical and electrical properties of sputter deposited AZO thin films. *Materials Science in Semiconductor Processing*, 37, 29-36.
- Parreira, P., Torres, E., Nunes, C., de Carvalho, C. N., Lavareda, G., Amaral, A., & Brites, M. J. (2012). Dye-sensitized 1D anatase TiO₂ nanorods for tunable efficient photodetection in the visible range. *Sensors and Actuators B: Chemical*, 161(1), 901-907.
- Pérez-Casero, R., Gutiérrez-Llorente, A., Pons-Y-Moll, O., Seiler, W., Defourneau, R. M., Defourneau, D., . . . Viana, B. (2005). Er-doped ZnO thin films grown by pulsed-laser deposition. *Journal of applied physics*, 97(5), 054905.
- Prades, J. D., Jimenez-Diaz, R., Hernandez-Ramirez, F., Fernandez-Romero, L., Andreu, T., Cirera, A., . . . Barth, S. (2008). Toward a systematic understanding of photodetectors based on individual metal oxide nanowires. *The Journal of Physical Chemistry C*, 112(37), 14639-14644.
- Qadir, K. W., Ahmad, Z., & Sulaiman, K. (2014). Performance enhancement of NiTsPc based photo sensor using treated TiO₂ NPs film. *Journal of nanoparticle research*, 16(11), 2705.
- Qadir, K. W., Ahmad, Z., Sulaiman, K., Yap, C. C., & Touati, F. (2015). Binary blend based dye sensitized photo sensor using PCPDTBT and MEH-PPV composite as a light sensitizer. *Synthetic Metals*, 210, 392-397.
- Rauch, T. (2014). *Spectral enhancement of organic photodetectors*: KIT Scientific Publishing.
- Reddy, B. M., Chowdhury, B., & Smirniotis, P. G. (2001). An XPS study of the dispersion of MoO₃ on TiO₂-ZrO₂, TiO₂-SiO₂, TiO₂-Al₂O₃, SiO₂-ZrO₂, and SiO₂-TiO₂-ZrO₂ mixed oxides. *Applied Catalysis A: General*, 211(1), 19-30.
- Reynal, A., & Palomares, E. (2011). Ruthenium polypyridyl sensitizers in dye solar cells based on mesoporous TiO₂. *European Journal of Inorganic Chemistry*, 2011(29), 4509-4526.
- Rives, V. (2001). *Layered double hydroxides: present and future*: Nova Publishers.
- Rogalski, A. (2002). Infrared detectors: an overview. *Infrared Physics & Technology*, 43(3), 187-210.
- Rogalski, A., & Razeghi, M. (1996). Semiconductor ultraviolet photodetectors. *OPTOELECTRONICS REVIEW*, 13-30.
- Roto, R., & Villemure, G. (2007). Cyclic voltammetry of metal bipyridyl cations at redox active Ni-Al-Cl layered double hydroxide films. *Journal of Electroanalytical Chemistry*, 601(1), 112-118.

- Roto, R., Yamagishi, A., & Villemure, G. (2004). Electrochemical quartz crystal microbalance study of mass transport in thin film of a redox active Ni–Al–Cl layered double hydroxide. *Journal of Electroanalytical Chemistry*, 572(1), 101-108.
- Saber, O., & Tagaya, H. (2009). Preparation of a new nano-layered materials and organic–inorganic nano-hybrid materials, Zn–Si LDH. *Journal of Porous Materials*, 16(1), 81-89.
- Sahoo, S., Husale, S., Colwill, B., Lu, T.-M., Nayak, S., & Ajayan, P. M. (2009). Electric field directed self-assembly of cuprous oxide nanostructures for photon sensing. *ACS nano*, 3(12), 3935-3944.
- Saito, Y., Azechi, T., Kitamura, T., Hasegawa, Y., Wada, Y., & Yanagida, S. (2004). Photo-sensitizing ruthenium complexes for solid state dye solar cells in combination with conducting polymers as hole conductors. *Coordination chemistry reviews*, 248(13), 1469-1478.
- Saleh, B. E., & Teich, M. C. (2007). Semiconductor photon detectors. *Fundamentals of Photonics*, 644-695.
- Salih, E. Y., Sabri, M. F. M., Hussein, M. Z., Sulaiman, K., Said, S. M., Saifullah, B., & Bashir, M. B. A. (2018). Structural, optical and electrical properties of ZnO/ZnAl₂O₄ nanocomposites prepared via thermal reduction approach. *Journal of Materials Science*, 53(1), 581-590.
- Salomao, R., Milena, L., Wakamatsu, M., & Pandolfelli, V. C. (2011). Hydrotalcite synthesis via co-precipitation reactions using MgO and Al (OH) 3 precursors. *Ceramics International*, 37(8), 3063-3070.
- Sampath, S. K., & Cordaro, J. F. (1998). Optical properties of zinc aluminate, zinc gallate, and zinc aluminogallate spinels. *Journal of the American Ceramic Society*, 81(3), 649-654.
- Sarkar, S., Mahapatra, A. D., & Basak, D. (2018). Self-powered highly enhanced broad wavelength (UV to visible) photoresponse of ZnO@ ZnO_{1-x}S_x@ ZnS core-shell heterostructures. *Journal of Colloid and Interface Science*, 523, 245-253.
- Schilinsky, P., Waldauf, C., Hauch, J., & Brabec, C. J. (2004). Polymer photovoltaic detectors: progress and recent developments. *Thin Solid Films*, 451, 105-108.
- Schubert, M. B., Sämann, M., Furin, D., Thielmann, J., Harendt, C., & Gauglitz, G. (2011). *Amorphous silicon based photodetectors for biosensing*. Paper presented at the Lasers and Electro-Optics Europe (CLEO EUROPE/EQEC), 2011 Conference on and 12th European Quantum Electronics Conference.
- Schwenzer, B., Pop, L. Z., Neilson, J. R., Sbardellati, T. B., & Morse, D. E. (2009). Nanostructured ZnS and CdS films synthesized using layered double hydroxide films as precursor and template. *Inorganic chemistry*, 48(4), 1542-1550.

- Sharma, A., Bhattacharyya, B., Srivastava, A., Senguttuvan, T., & Husale, S. (2016). High performance broadband photodetector using fabricated nanowires of bismuth selenide. *Scientific Reports*, 6, 19138.
- Shu, G., Liu, J., Chiang, A. S., & Thompson, R. W. (2006). Transparent zeolite films with regular surface patterns. *Advanced Materials*, 18(2), 185-189.
- Sima, C., Grigoriu, C., & Antohe, S. (2010). Comparison of the dye-sensitized solar cells performances based on transparent conductive ITO and FTO. *Thin Solid Films*, 519(2), 595-597.
- Sing, K. S. (1985). Reporting physisorption data for gas/solid systems with special reference to the determination of surface area and porosity (Recommendations 1984). *Pure and applied chemistry*, 57(4), 603-619.
- Skotheim, T. A., & Reynolds, J. (2006). *Conjugated polymers: processing and applications*: CRC press.
- Song, J., Leng, M., Fu, X., & Liu, J. (2012). Synthesis and characterization of nanosized zinc aluminate spinel from a novel Zn–Al layered double hydroxide precursor. *Journal of Alloys and Compounds*, 543, 142-146.
- Song, L., Shi, W., & Lu, C. (2016). Confinement Effect in Layered Double Hydroxide Nanoreactor: Improved Optical Sensing Selectivity. *Analytical chemistry*, 88(16), 8188-8193.
- Suzuki, Y., Yamaguchi, H., Oonuki, K., Okamura, Y., & Okano, K. (2003). Amorphous selenium photodetector driven by diamond cold cathode. *IEEE Electron Device Letters*, 24(1), 16-18.
- Syrrokostas, G., Siokou, A., Leftheriotis, G., & Yianoulis, P. (2012). Degradation mechanisms of Pt counter electrodes for dye sensitized solar cells. *Solar Energy Materials and Solar Cells*, 103, 119-127.
- Tang, A., & Zhang, X. (2006). Mechanochemical route to synthesize Co₃O₄/CuO composite nanopowders. *International Journal of Physical Sciences*, 1(2), 102-105.
- Tang, C. W. (1986). Two-layer organic photovoltaic cell. *Applied Physics Letters*, 48(2), 183-185.
- Tao, R., Tomita, T., Wong, R. A., & Waki, K. (2012). Electrochemical and structural analysis of Al-doped ZnO nanorod arrays in dye-sensitized solar cells. *Journal of Power Sources*, 214, 159-165.
- Teng, C.-j., Xie, D., Sun, M.-x., Chen, S., Yang, P., & Sun, Y.-l. (2016). Organic Dye-Sensitized CH₃NH₃PbI₃ Hybrid Flexible Photodetector with Bulk Heterojunction Architectures. *ACS applied materials & interfaces*, 8(45), 31289-31294.

- Tsekouras, G., Mozer, A. J., & Wallace, G. G. (2008). Enhanced performance of dye sensitized solar cells utilizing platinum electrodeposit counter electrodes. *Journal of The Electrochemical Society*, 155(7), K124-K128.
- Tzeng, S., Hon, M., & Leu, I. (2010). Improvement in the photocurrent to dark current contrast ratio of ZnO/Au Schottky photodetector with PMMA microlens arrays. *Journal of The Electrochemical Society*, 157(10), H919-H923.
- Umar, A., & Hahn, Y.-B. (2010). *Metal oxide nanostructures and their applications* (Vol. 5): American Scientific Publ.
- Valouch, S., Huska, K., Hetterich, J., Colsmann, A., Moosmann, C., Dopf, K., . . . Christ, N. Nanostructured organic photodiodes.
- Van der Laag, N., Snel, M., Magusin, P., & De With, G. (2004). Structural, elastic, thermophysical and dielectric properties of zinc aluminate (ZnAl₂O₄). *Journal of the European Ceramic Society*, 24(8), 2417-2424.
- Velu, S., Ramkumar, V., Narayanan, A., & Swamy, C. (1997). Effect of interlayer anions on the physicochemical properties of zinc–aluminium hydroxalcalite-like compounds. *Journal of Materials Science*, 32(4), 957-964.
- Wang, D., Ren, H., & Yu, R. (2017). *Graphdiyne nanosheet/Pt nanoparticle-based counter electrode material with enhanced catalytic activity for dye-sensitized solar cells*. Paper presented at the ABSTRACTS OF PAPERS OF THE AMERICAN CHEMICAL SOCIETY.
- Wang, J., & Lin, Z. (2012). Dye-Sensitized TiO₂ Nanotube Solar Cells: Rational Structural and Surface Engineering on TiO₂ Nanotubes. *Chemistry–An Asian Journal*, 7(12), 2754-2762.
- Wang, P., Dai, Q., Zakeeruddin, S. M., Forsyth, M., MacFarlane, D. R., & Grätzel, M. (2004). Ambient temperature plastic crystal electrolyte for efficient, all-solid-state dye-sensitized solar cell. *Journal of the American Chemical Society*, 126(42), 13590-13591.
- Wang, P., Zakeeruddin, S. M., Moser, J.-E., Humphry-Baker, R., & Grätzel, M. (2004). A solvent-free, SeCN⁻/(SeCN)³⁻-based ionic liquid electrolyte for high-efficiency dye-sensitized nanocrystalline solar cells. *Journal of the American Chemical Society*, 126(23), 7164-7165.
- Wang, P., Zakeeruddin, S. M., Moser, J. E., Nazeeruddin, M. K., Sekiguchi, T., & Grätzel, M. (2003). A stable quasi-solid-state dye-sensitized solar cell with an amphiphilic ruthenium sensitizer and polymer gel electrolyte. *Nature materials*, 2(6), 402-407.
- Wang, X., Song, W., Liu, B., Chen, G., Chen, D., Zhou, C., & Shen, G. (2013). High-Performance Organic-Inorganic Hybrid Photodetectors Based on P3HT: CdSe Nanowire Heterojunctions on Rigid and Flexible Substrates. *Advanced Functional Materials*, 23(9), 1202-1209.

- Wang, Z., Wang, H., Liu, B., Qiu, W., Zhang, J., Ran, S., . . . Chen, D. (2011). Transferable and flexible nanorod-assembled TiO₂ cloths for dye-sensitized solar cells, photodetectors, and photocatalysts. *ACS nano*, 5(10), 8412-8419.
- Waynant, R. W., & Ediger, M. N. (2000). *Electro-optics handbook*: McGraw-Hill New York.
- Wei, M., Zhang, X., Evans, D. G., Duan, X., Li, X., & Chen, H. (2007). Rh-TPPTS intercalated layered double hydroxides as hydroformylation catalyst. *AIChE journal*, 53(11), 2916-2924.
- Williams, G. R., & O'Hare, D. (2006). Towards understanding, control and application of layered double hydroxide chemistry. *Journal of Materials Chemistry*, 16(30), 3065-3074.
- Wu, F., Bai, J., Feng, J., & Xiong, S. (2015). Porous mixed metal oxides: design, formation mechanism, and application in lithium-ion batteries. *Nanoscale*, 7(41), 17211-17230.
- Wu, Z., Chen, Z., Du, X., Logan, J. M., Sippel, J., Nikolou, M., . . . Hebard, A. F. (2004). Transparent, conductive carbon nanotube films. *science*, 305(5688), 1273-1276.
- Xie, J. (2013). *Characterisation of low noise InGaAs/AlAsSb avalanche photodiodes*. University of Sheffield,
- Xue, H., Kong, X., Liu, Z., Liu, C., Zhou, J., Chen, W., . . . Xu, Q. (2007). Ti O₂ based metal-semiconductor-metal ultraviolet photodetectors. *Applied Physics Letters*, 90(20), 201118.
- Yang, L. (2014). *Hole Transport Materials for Solid-State Mesoscopic Solar Cells*. Acta Universitatis Upsaliensis,
- Yang, M., Ding, B., & Lee, J.-K. (2014). Surface electrochemical properties of niobium-doped titanium dioxide nanorods and their effect on carrier collection efficiency of dye sensitized solar cells. *Journal of Power Sources*, 245, 301-307.
- Yang, Y., Chen, X., Feng, Y., & Yang, G. (2007). Physical mechanism of blue-shift of UV luminescence of a single pencil-like ZnO nanowire. *Nano letters*, 7(12), 3879-3883.
- Yang, Y., Yan, X., Hu, X., Feng, R., & Zhou, M. (2017). In-situ growth of ZIF-8 on layered double hydroxide: Effect of Zn/Al molar ratios on their structural, morphological and adsorption properties. *Journal of Colloid and Interface Science*.
- Ye, M., Wen, X., Wang, M., Iocozzia, J., Zhang, N., Lin, C., & Lin, Z. (2015). Recent advances in dye-sensitized solar cells: from photoanodes, sensitizers and electrolytes to counter electrodes. *Materials today*, 18(3), 155-162.
- Ye, M., Xin, X., Lin, C., & Lin, Z. (2011). High efficiency dye-sensitized solar cells based on hierarchically structured nanotubes. *Nano letters*, 11(8), 3214-3220.

- Yoshikawa, A., Matsunami, H., & Nanishi, Y. (2007). Development and Applications of Wide Bandgap Semiconductors. In *Wide Bandgap Semiconductors* (pp. 1-24): Springer.
- Yotter, R. A., & Wilson, D. M. (2003). A review of photodetectors for sensing light-emitting reporters in biological systems. *IEEE Sensors Journal*, 3(3), 288-303.
- Yu, G., Pakbaz, K., & Heeger, A. (1994). Semiconducting polymer diodes: Large size, low cost photodetectors with excellent visible-ultraviolet sensitivity. *Applied Physics Letters*, 64(25), 3422-3424.
- Yu, J., Yang, Y., Fan, R., Zhang, H., Li, L., Wei, L., . . . Fu, H. (2013). Er³⁺ and Yb³⁺ co-doped TiO_{2-x}F_x up-conversion luminescence powder as a light scattering layer with enhanced performance in dye sensitized solar cells. *Journal of Power Sources*, 243, 436-443.
- Yu, S. H., Lee, Y., Jang, S. K., Kang, J., Jeon, J., Lee, C., . . . Lee, S. (2014). Dye-sensitized MoS₂ photodetector with enhanced spectral photoresponse. *ACS nano*, 8(8), 8285-8291.
- Yuan, X., Jing, Q., Chen, J., & Li, L. (2017). Photocatalytic Cr (VI) reduction by mixed metal oxide derived from ZnAl layered double hydroxide. *Applied Clay Science*, 143, 168-174.
- Yun, S., Lee, J., Chung, J., & Lim, S. (2010). Improvement of ZnO nanorod-based dye-sensitized solar cell efficiency by Al-doping. *Journal of Physics and Chemistry of Solids*, 71(12), 1724-1731.
- Zhai, T., Fang, X., Liao, M., Xu, X., Li, L., Liu, B., . . . Bando, Y. (2010). Fabrication of high-quality In₂Se₃ nanowire arrays toward high-performance visible-light photodetectors. *ACS nano*, 4(3), 1596-1602.
- Zhai, T., Li, L., Wang, X., Fang, X., Bando, Y., & Golberg, D. (2010). Recent Developments in One-Dimensional Inorganic Nanostructures for Photodetectors. *Advanced Functional Materials*, 20(24), 4233-4248.
- Zhang, F., Niu, S., Guo, W., Zhu, G., Liu, Y., Zhang, X., & Wang, Z. L. (2013). Piezophototronic effect enhanced visible/UV photodetector of a carbon-fiber/ZnO-CdS double-shell microwire. *ACS nano*, 7(5), 4537-4544.
- Zhang, F., Sun, M., Xu, S., Zhao, L., & Zhang, B. (2008). Fabrication of oriented layered double hydroxide films by spin coating and their use in corrosion protection. *Chemical Engineering Journal*, 141(1), 362-367.
- Zhang, F., Zhao, L., Chen, H., Xu, S., Evans, D. G., & Duan, X. (2008). Corrosion resistance of superhydrophobic layered double hydroxide films on aluminum. *Angewandte Chemie International Edition*, 47(13), 2466-2469.
- Zhang, H., Jenatsch, S., De Jonghe, J., Nüesch, F., Steim, R., Véron, A. C., & Hany, R. (2015). Transparent organic photodetector using a near-infrared absorbing cyanine dye. *Scientific Reports*, 5.

- Zhang, L., Dai, C.-h., Zhang, X.-x., Liu, Y.-n., & Yan, J.-h. (2016). Synthesis and highly efficient photocatalytic activity of mixed oxides derived from ZnNiAl layered double hydroxides. *Transactions of Nonferrous Metals Society of China*, 26(9), 2380-2389.
- Zhang, L., Liu, J., Xiao, H., Liu, D., Qin, Y., Wu, H., . . . Hou, W. (2014). Preparation and properties of mixed metal oxides based layered double hydroxide as anode materials for dye-sensitized solar cell. *Chemical Engineering Journal*, 250, 1-5.
- Zhang, Q., Dandeneau, C. S., Zhou, X., & Cao, G. (2009). ZnO nanostructures for dye-sensitized solar cells. *Advanced Materials*, 21(41), 4087-4108.
- Zhang, R., Pan, J., Briggs, E. P., Thrash, M., & Kerr, L. L. (2008). Studies on the adsorption of RuN3 dye on sheet-like nanostructured porous ZnO films. *Solar Energy Materials and Solar Cells*, 92(4), 425-431.
- Zhang, T.-F., Li, Z.-P., Wang, J.-Z., Kong, W.-Y., Wu, G.-A., Zheng, Y.-Z., . . . Luo, L.-B. (2016). Broadband photodetector based on carbon nanotube thin film/single layer graphene Schottky junction. *Scientific Reports*, 6.
- Zhang, W., Chuu, C.-P., Huang, J.-K., Chen, C.-H., Tsai, M.-L., Chang, Y.-H., . . . Chou, M.-Y. (2014). Ultrahigh-gain photodetectors based on atomically thin graphene-MoS₂ heterostructures. *Scientific reports*, 4.
- Zhao, Q., Guo, Y., Zhou, Y., Yan, X., & Xu, X. (2017). Solution-processable exfoliation and photoelectric properties of two-dimensional layered MoS₂ photoelectrodes. *Journal of colloid and interface science*, 490, 287-293.
- Zhao, X., Wang, L., Xu, X., Lei, X., Xu, S., & Zhang, F. (2012). Fabrication and photocatalytic properties of novel ZnO/ZnAl₂O₄ nanocomposite with ZnAl₂O₄ dispersed inside ZnO network. *AIChE Journal*, 58(2), 573-582.
- Zhao, X., Zhang, F., Xu, S., Evans, D. G., & Duan, X. (2010). From layered double hydroxides to ZnO-based mixed metal oxides by thermal decomposition: transformation mechanism and UV-blocking properties of the product. *Chemistry of Materials*, 22(13), 3933-3942.
- Zheng, L., Zheng, Y., Chen, C., Zhan, Y., Lin, X., Zheng, Q., . . . Zhu, J. (2009). Network structured SnO₂/ZnO heterojunction nanocatalyst with high photocatalytic activity. *Inorganic chemistry*, 48(5), 1819-1825.
- Zhu, Y., Wang, D., Yang, X., Liu, S., Liu, D., Liu, J., . . . Liu, J. (2017). Investigation of the dye-sensitized solar cell designed by a series of mixed metal oxides based on ZnAl-layered double hydroxide. *Applied Physics A*, 123(10), 641.
- Zimmermann, H. (2009). Silicon technologies and integrated photodetectors. In *Integrated Silicon Optoelectronics* (pp. 29-153): Springer.

University of Malaya

APPENDICES

Appendix A

Raw materials specifications and chemical formulas

The materials which were used in the current study are outlined with their chemical and physical properties as follow:

- i. Zinc nitrate hexahydrate:** Zinc nitrate hexahydrate with chemical formula of $\text{Zn}(\text{NO}_3)_2 \cdot 6\text{H}_2\text{O}$ (Aldrich, 98.1%) is a chemical compound with white crystal appearance and highly soluble in water and alcohol. Its chemical structure comprises a zinc salt and nitric acid. In detail, the molar mass of $\text{Zn}(\text{NO}_3)_2 \cdot 6\text{H}_2\text{O}$ is 297.49 g/mol, a density of 2.065 g/cm³ and melting and boiling points of 36.4 °C and 125 °C, respectively.
- ii. Aluminum nitrate nonahydrate:** Aluminum nitrate nonahydrate with chemical formula $\text{Al}(\text{NO}_3)_3 \cdot 9\text{H}_2\text{O}$ (Merck Co., 99.4%) is known as a chemical compound with white and most commonly crystal form and highly soluble in water. The chemical structure of aluminum nitrate nonahydrate also comprises an aluminum salt and nitric acid. It has molar mass of 375.13 g/mol and density of 1.72 g/cm³ (nonahydrate), while the melting and boiling points are 73.9 °C and 150 °C, respectively.
- iii. Sodium hydroxide:** Sodium hydroxide which is also named “lye and caustic soda” is well-known as inorganic compound. The chemical formula of sodium hydroxide is NaOH (Aldrich, 99%). NaOH is consisting of sodium cations Na^+ and hydroxide anions OH^- . NaOH is a white solid ionic compound which is very caustic base and alkali, also very soluble in water and absorbs moisture readily as well as carbon dioxide in air. It has

molar mass of 39.997 g/mol, a density of 2.13 g/cm³, while the melting and boiling points are 318 °C and 1338 °C, respectively.

- iv. **Fluorine-doped tin oxide:** Fluorine-doped tin oxide which well-known as FTO (Solaronix) is a transparent colorless conductive oxide (TCO) material. FTO-coated glass substrate was selected to be used in both anode and cathode electrodes in this study due to the sufficient electrical conductivity, cost-effective, low sheet resistance (7 Ω/sq) and excellent thermal and chemical stability under atmospheric conditions (J. Gong *et al.*, 2012).
- v. **Polyethylene glycol 400:** PEG 400 with the chemical formula of C_{2n}H_{4n+2}O_{n+1} (n = 8.1) is sufficiently low molecular grade of PEG. It has colorless, clear, and viscous watery chemical compound and highly soluble in ethanol. The molar mass of PEG 400 is 380-420 g/mol while its density is 1.128 g/cm³. In the meanwhile its melting point is 4-8 °C and viscosity of 90 cSt at room temperature.
- vi. **Ruthenizer 535-bis TBA:** Ruthenizer which is well-known as N719 is a high performance ruthenium dye with chemical formula C₅₈H₈₆O₈N₈S₂RU (Solaronix), it has the chemical name of cis-diisothiocyanato-bis(2,2'-bipyridyl-4,4'-dicarboxylato) ruthenium(II) bis(tetrabutylammonium). The dark purple powder N719 with molar mass of 1188.6 g/mol is highly soluble in alcohol (Ethanol specifically) and very sensitive to light.
- vii. **Iodolyte HI-30:** Iodolyte HI-30 (Solaronix) is a brown liquid redox couple electrolyte (iodide/tri-iodide). The chemical structure of the iodolyte HI-30 comprises an ionic liquid, lithium salt and pyridine derivative. It is highly soluble in acetonitrile.

Appendix B

Raw materials calculations for preparation of ZrA-LDH samples

Molecular weight of elements:

$$\text{Zn (NO}_3)_2 \cdot 6\text{H}_2\text{O} = 297.49 \frac{\text{g}}{\text{mol}} \quad \text{purity} = 98.1 \%$$

$$\text{Al (NO}_3)_3 \cdot 9\text{H}_2\text{O} = 375.13 \frac{\text{g}}{\text{mol}} \quad \text{purity} = 99.4 \%$$

$$\text{NaOH} = 40 \frac{\text{g}}{\text{mol}} \quad \text{purity} = 99.0 \%$$

Accordinging the equation below

$$Wt = \text{Molarity} \times \text{Volume (L)} \times \text{Mol. Wt} \left(\frac{\text{g}}{\text{mol}}\right) \times \frac{100}{\text{purity}}$$

The molar ratios of the prepared materials are Zn^{2+} to $\text{Al}^{3+} = 3:1, 4:1, 5:1, 6:1$ and $7:1$; and the NaOH prepared with 1.5 molar concentration:

I. For the calculation of $\text{Zn (NO}_3)_2 \cdot 6\text{H}_2\text{O}$ with concentration of 0.1 Molar

$$Wt = 0.1 \times \frac{150}{1000} (\text{L}) \times 297.49 \left(\frac{\text{g}}{\text{mol}}\right) \times \frac{100}{98.1}$$

$$Wt = 4.55 \text{ g}$$

II. For the calculation of $\text{Al (NO}_3)_3 \cdot 9\text{H}_2\text{O}$ with concentration of 0.033 Molar

$$Wt = 0.033 \times \frac{150}{1000} (\text{L}) \times 375.13 \left(\frac{\text{g}}{\text{mol}}\right) \times \frac{100}{99.4}$$

$$Wt = 1.87 \text{ g}$$

III. For the calculation of $\text{Al}(\text{NO}_3)_2 \cdot 9\text{H}_2\text{O}$ with concentration of 0.025 Molar

$$Wt = 0.025 \times \frac{150}{1000} (L) \times 375.13 \left(\frac{g}{mol}\right) \times \frac{100}{99.4}$$

$$Wt = 1.42 \text{ g}$$

IV. For the calculation of $\text{Al}(\text{NO}_3)_2 \cdot 9\text{H}_2\text{O}$ with concentration of 0.02 Molar

$$Wt = 0.02 \times \frac{150}{1000} (L) \times 375.13 \left(\frac{g}{mol}\right) \times \frac{100}{99.4}$$

$$Wt = 1.13 \text{ g}$$

V. For the calculation of $\text{Al}(\text{NO}_3)_2 \cdot 9\text{H}_2\text{O}$ with concentration of 0.0166 Molar

$$Wt = 0.0166 \times \frac{150}{1000} (L) \times 375.13 \left(\frac{g}{mol}\right) \times \frac{100}{99.4}$$

$$Wt = 0.94 \text{ g}$$

VI. For the calculation of $\text{Al}(\text{NO}_3)_2 \cdot 9\text{H}_2\text{O}$ with concentration of 0.0142 Molar

$$Wt = 0.0142 \times \frac{150}{1000} (L) \times 375.13 \left(\frac{g}{mol}\right) \times \frac{100}{99.4}$$

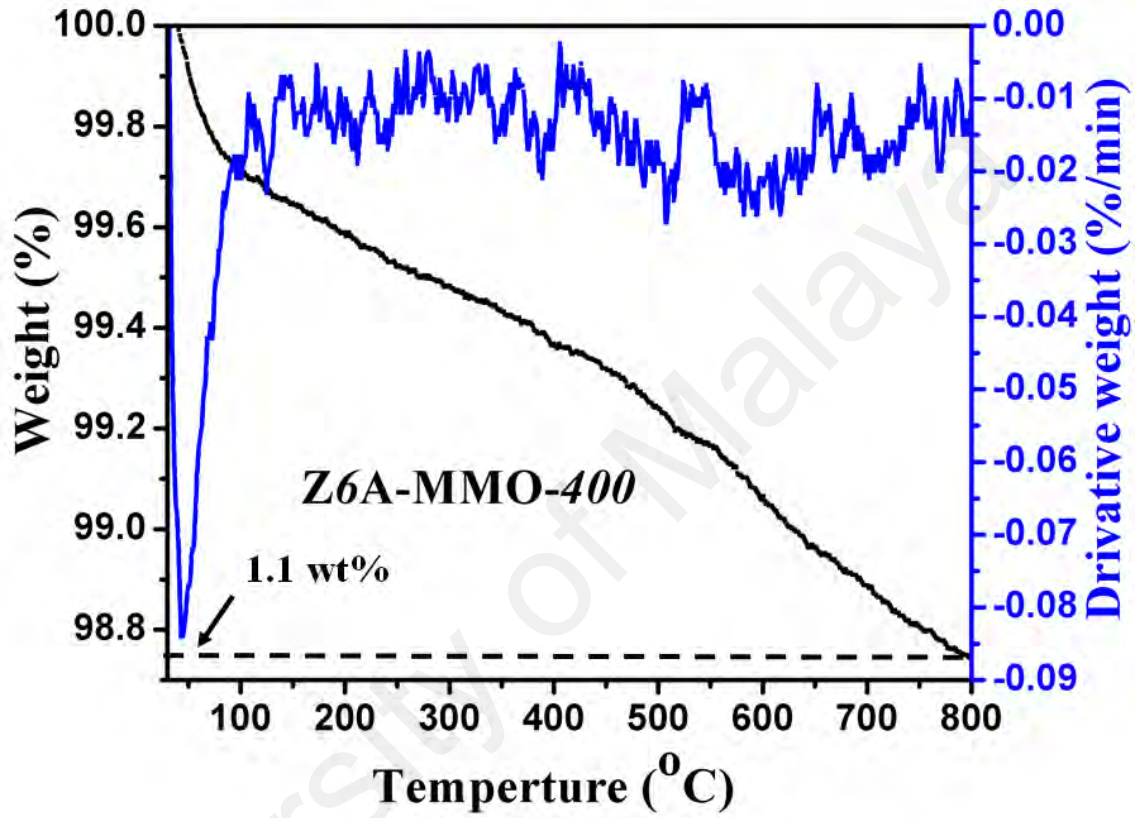
$$Wt = 0.80 \text{ g}$$

VII. For the calculation of NaOH with concentration of 2 Molar

$$Wt = 2 \times \frac{250}{1000} (L) \times 40 \left(\frac{g}{mol}\right) \times \frac{100}{99}$$

Appendix C

Thermal analysis (TGA/DTG) of Z6A-MMO-400



Appendix D

The sequence order of photocurrent magnitude at 100 mW/cm^2 as a function of thermal treatment temperature and molar ratio

